Testing and Modelling of Electrical Traction Machines

Performance Characterisation with Measurements from Transient Operation

SEBASTIAN HALL
FACULTY OF ENGINEERING | LUND UNIVERSITY

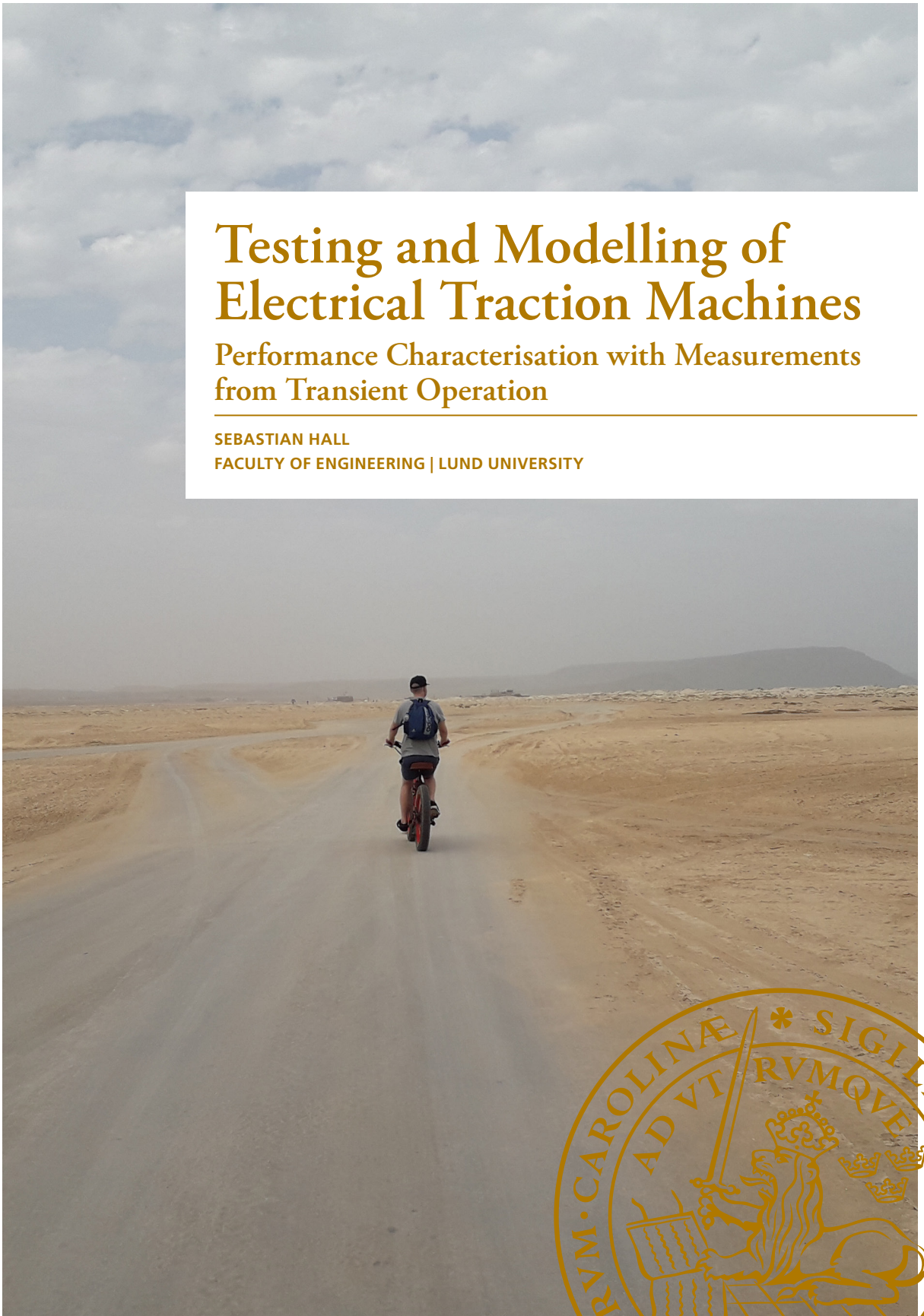

Testing and Modelling of Electrical Traction Machines

Testing and Modelling of Electrical Traction Machines

Performance Characterisation with Measurements from Transient Operation

by Sebastian Hall

LUND
UNIVERSITY

Thesis for the degree of Doctor of Philosophy in Engineering
Thesis advisors: Prof. Mats Alaküla, Assoc. Prof. Avo Reinap
Faculty opponent: Assoc. Prof. Pia Lindh

To be presented, with the permission of the Faculty of Engineering of Lund University, for public criticism in the E:A lecture hall, Electrical Engineering Building, Ole Römers väg, Lund Sweden, on Friday, the 10th of May 2019 at 10:15.

Organization	Document name
LUND UNIVERSITY Department of Biomedical Engineering Box 118 SE–221 00 LUND, Sweden	**DOCTORAL DISSERTATION** Date of disputation 2019-05-10 Sponsoring organization
Author(s) Sebastian Hall	

Title and subtitle

Testing and Modelling of Electrical Traction Machines:
Performance Characterisation with Measurements from Transient Operation

Abstract

This thesis presents methods to derive and model the performance characteristics of interior permanent magnet machines – a machine type which is commonly used for propulsion of electrical vehicles. The thesis divides the performance characteristics into three subcategories: The electromagnetic properties, the loss profile and the thermal behaviour of the machines. One separate characterisation method is presented for each subcategory. However, all three methods have in common that they use data solely from mechanical or thermal transient operation. The methods aim to derive the characteristics with as little and as cheap equipment as possible, and to minimise the duration time of the tests.

The procedure that derives the electromagnetic properties uses measurements from when the test objects accelerate and brakes. The method obtains the relationship between the current and the linked magnetic flux in the stator windings with relatively small means, and it does not demand a brake machine or a power analyser. Furthermore, due to the low time duration of the tests, the method is well suited to derive the temperature dependence of the current/flux relationships. The loss profile of the machine is derived with a similar method as the magnetic model, but requires lower mechanical dynamics. Therefore, the method generally requires an increase of the moment of inertia of the rotating parts of the machines. This is typically achieved by mounting flywheels on the shafts of the test objects. The method yields results that are well suited to use as identification data for loss models of the machines. The thermal characteristics of the test objects are obtained from temperature measurements during transient thermal conditions. The measured data are used to derive an equivalent circuit that describes the thermal behaviour of the test object well.

Key words

Electrical machines, Interior permanent magnet synchronous machines (IPMSMs), Testing, characterisation, Modelling

Classification system and/or index terms (if any)

Supplementary bibliographical information	Language
	English
ISSN and key title	ISBN
	978-91-88934-98-7 (print) 978-91-88934-99-4 (pdf)
Recipient's notes	Number of pages: 201 / Price
	Security classification

Testing and Modelling of Electrical Traction Machines

Performance Characterisation with Measurements from Transient Operation

by Sebastian Hall

LUND
UNIVERSITY

Cover illustration: Electric biking into the horizon

Faculty of Engineering
Department of Biomedical Engineering
Division of Industrial Electrical Engineering and Automation

ISBN: 978-91-88934-98-7 (print)
ISBN: 978-91-88934-99-4 (pdf)
ISSN: LUTEDX/(TEIE-1092)/1-201/(2019)

Printed in Sweden by Media-Tryck, Lund University, Lund 2019

It's not about possible or impossible
I'm doing it because I want to
- Monkey D. Luffy

Contents

List of publications

Journal publications

I **Dynamic Magnetic Model Identification of Permanent Magnet Synchronous Machines**

S. Hall, F. J. Marquez-Fernandez, M. Alakaüla
IEEE Transactions on Energy Conversion, vol. 32, no. 4, pp. 1367-1375, Dec. 2017.

II **Dynamic Testing Characterization of a Synchronous Reluctance Machine**

S. Wiedemann, **S. Hall**, R. Kennel, M. Alaküla
IEEE Transactions on Industry Applications, vol. 54, no. 2, pp. 1370-1378, March-April 2018.

Conference publications

III **Lumped-parameter grey-box modelling of traction machines for low-speed applications**

S. Hall, M. Alaküla
2018 International conference on Electrical machines (ICEM), Alexandroupoli, 2018, pp. 2668-2674.

IV **Consistency analysis of torque measurements performed on a PMSM using dynamic testing**

S. Hall, Y. Loayza, A. Reinap, M. Alaküla
2014 International conference on Electrical machines (ICEM), Berlin, 2014, pp. 1529-1535.

V **An evaluation of two Direct Current Control methods implemented with LabVIEW on a FPGA**

S. Hall, Y. Loayza
2013 International Conference on Electrical Machines and Systems (ICEMS), Busan, 2013, pp. 1455-1460.

VI **Evaluation of a temperature model for an Interior Permanent Magnet Synchronous Machine for parallel hybrid electric heavy vehicle**

R. Andersson, **S. Hall**
2016 International Symposium on Power Electronics, Electrical Drives, Automation and Motion (SPEEDAM), Anacapri, 2016, pp. 419-424.

Licentiate thesis

VII **Dynamic Testing of Permanent Magnet Synchronous Machines**
S. Hall
Licentiate thesis, Lund University, 2016

Acknowledgements

It has been a long ride and I have met many fantastic people along the way. This is for the most important:

The Senseis

Mats Alaküla - The man who made this possible. I am forever grateful.

Avo Reinap - The philosophy sessions have been outstanding.

Fran Marquez - The master reader, thanks for everything.

The Workshop Ninja

Getachew Darge - Person number two that made this possible at all. Thanks!

The Admin Heroins

Carina Lindström - Carina, where would I be without you?

Ulrika Westerdahl - And Ulrika, where would I be without you?

Probably nowhere.

The Crew

Gabriel Domingues - Many memories my friend...

Anton Karlsson - One year feels like 12h ago!

Rasmus Andersson - But you will have to stick with me for a while longer.

Lars Lindgren - Infinite fountain of knowledge.

Max Collins - Throw up Maxwell's four like it was nothing!

Bobby Frank - Take it easy with the chillies though...

Philip - But keep lifting those weights!

Samuel - And keep eating that cake!

Plus all the people that came and went... -Thank you!

(A special thanks to Simon Wiedemann for the work and the friendship!)

The Senior Staff

Ulf Jeppson - Steady like a rock.

Johan Björnstedt - Keep ETG alive!

And Henriette, Gunnar, Bengt, and all I've missed - Thank you!

(A special thanks to Lars Gertman for reading the thesis!)

The Closest Ones

Mamma - You are the best.

Pappa - And you too.

Lillebror - And you too.

Storebror - And you too.

Gisse - Thanks for sticking around during my egocentric episodes. You are my favourite person in the whole world.

Popular summary

Testing, characterisation and modelling of electrical machines might sound like a dry and unsexy subject; however, after a scratch on the surface one can find a quite hot content. Well, hot (as well as cool) might be a bit misleading, and the word relevant probably describes the topic better. In either case, due to the increased interest in applications with a highly dynamic loading pattern, one can expect an increasing need for extensive evaluation of machines that fit such applications well in the next-coming years. Unfortunately, the testing and evaluation methods that are used today generally demand quite a lot of equipment. Furthermore, the durations of these tests tend to be long. Therefore, it makes sense to investigate alternative approaches that obtain as much information about the characteristics of the test object as possible with as small means as possible. And abracadabra, an empty space opens up in the jungle of research.

The purpose of the testing and evaluation is to obtain information about how the electrical machine under test reacts to a certain input. If one for instance excites the stator windings of the machine with specific currents, a torque that creates rotation arises. In addition, the currents and the rotation generate heat. If the torque and the heat can be quantified for many different currents and rotational speeds, one can obtain a good picture of the performance of the machine, which in turn can be used as base for e.g. performance validation, modelling and optimisation of the machine operation. Furthermore, knowledge about the thermal characteristics makes it possible to foresee when the temperature of the machine approaches levels where it might cause damage. Consequently, this knowledge can be used to predict the maximum machine power. In summary, the most important machine characteristics to have information about can be devided up into three chategories:

1. The torque (that results in rotation) as a function of the stator currents.
2. The power losses (that generate heat) as functions of the currents and the speed.
3. The temperature distribution in the machine as a function of the stator currents and the speed.

The torque of a machine can be measured with a torque sensor on the rotating axis, but it can also be calculated if the electromagnetic properties of the test object are known. This thesis presents a method that estimates the electromagnetic properties based on measurements from when the machine accelerates and brakes, and it therefore does not require a load to keep the machine speed constant (which is otherwise common in this type of machine characterisation). Furthermore, the tests are quick, which means that the temperature does not have time to rise significantly during the procedure. Therefore, the characterisation

can be performed quickly at different temperatures to see if the electromagnetic properties, and consequently also the torque, change.

The power of a machine is generally measured in a setup where the shaft of the test object is connected to a second machine that keeps the rotational speed constant. A sensor in between the test object and the second machine measures the relevant parameters to obtain the mechanical power (the torque and the speed). At the same time, a so called power analyser measures the electrical power. When the mechanical and electrical powers are known, the power losses can be estimated by calculating the difference between them. Even though this procedure gives accurate results, it demands long testing times and expensive setups. Therefore, this thesis presents an alternative approach that estimates the mechanical power from accelerations and retardations. In addition, relatively cheap industrial sensors measure the electrical power. Consequently, one obtains a good estimate of the loss characteristics of the machine with very small means.

The temperature profile of a machine depends on the aforementioned power losses, but also on its geometry, material characteristics and cooling strategies. A common way to model the temperature behaviour of a machine is to design a so called lumped-parameter circuit. If the circuit has a sufficient design and accurate parameters, one can obtain a good estimate of the temperature in the machine as a function of the power losses and the cooling. This thesis presents a method to obtain parameter values that result in good simulations of the temperature. The method estimates the parameters based on measurement data during transient power loading, and it can therefore foresee the thermal behaviour even when the machine reaches very high temperatures.

In summary, this thesis presents methods that estimate the most fundamental characteristics of electrical traction machines with alternative approaches. Hopefully, the content gives inspiration to engineers and other interested people to keep evaluating machines in new innovative manners. As the great Churchill said: *Now this is not the end. It is not even the beginning of the end. But it is, perhaps, the end of the beginning*. For these test methods, that is.

Nomenclature

Abbreviations

AC Alternating Current

ATO Angle Tracker Observer

CFD Computational Fluid Dynamics

D/A Digital/Analogue

DAQ Data AcQuisition

DC Direct Current

LUT Look-Up Table

FDT Fringe Detection Technique

FEM Finite-Element Method

FIFO First In First Out

FOC Field-oriented controller

FPGA Field-Programmable Gate Array

PM Permanent Magnet

PMSM Permanent Magnet Synchronous Machine

- **IPMSM** Interior Permanent Magnet Synchronous Machine
- **SMPMSM** Surface Mounted Permanent Magnet Synchronous Machine

Scalars

A Area [m²]

B_p Peak magnetic flux density [T]

C Thermal capacitances [J/K]

- C_{ew} End-winding capacitance
- C_w Winding capacitance

- C_t Teeth capacitance
- C_y Yoke capacitance
- C_h House capacitance
- C_c Coolant capacitance

C_p Specific heat capacity [J/(kg·K)]

$\mathcal{C}_{mc}$ Moment coefficient [-]

d Duty cycle [-]

f Frequency [Hz]

G_{rr} Rolling friction factor [-] (from empirical equation)

G_{sl} Sliding friction factor [-] (from empirical equation)

h Heat transfer coefficient [W/(m²·K)]

i Electric current [A]

- i^s_{dq} Stator winding currents in the synchronous reference frame
- i^f_{dq} Currents that give rise to eddy-current losses
- i^ψ_{dq} Currents that result in linked magnetic flux

J Moment of inertia [kg·m²]

$\mathcal{J}$ Current density [A/m²]

k Power loss model constants

- k_{ss} Frequency-independent loss coefficient [W]
- k_l Linearly frequency-dependent loss coefficient [Ws]
- k_q Quadratically frequency-dependent loss coefficient [Ws²]

$\mathcal{K}$ Iron loss constants

- $\mathcal{K}_h$ Hysteresis loss constant [Ws/T$^{\alpha_h}$]
- $\mathcal{K}_c$ Classical loss constant [Ws²/T²]
- $\mathcal{K}_e$ Excess loss constant [Ws$^{1.5}$/T$^{1.5}$]

L Inductance [H]

- L_{dq} Constant inductances in the synchronous reference frame

$L_{dq\,\textbf{differential}}^{(i_d^s, i_q^s)}$ Differential inductance as a function of the dq-axes currents

$L_{dq\,\textbf{apparent}}^{(i_d^s, i_q^s)}$ Apparent inductance as a function of the dq-axes currents

n Rotational speed [rpm]

n_{pp} Number of pole pairs [-]

P_e Electrical power [W]

P_{loss} Power losses [W]

$\hat{P}_{loss,mg}$ Power loss estimation from generator and motor operation

$\hat{P}_{loss,sd}$ Speed-dependent power loss estimation from loss torque

$\hat{P}_{DC}$ Power loss due to DC resistance

P_m Mechanical power [W]

Q Heat [J]

$\dot{Q}$ Rate of heat change [W]

q Factor that divides total winding into end-winding and active winding [-]

r Radius [m]

R Electric resistance [Ω]

R_{DC} DC winding resistance

R_{DC} Equivalent eddy-current loss resistance

R_s Stator winding resistance

R_{skin} Resistance due to skin effect

R_0 Resistance of thermal model

$\mathcal{R}$ Thermal resistance [K/W]

$\mathcal{R}_{ew\leftrightarrow w}$ End-winding-to-winding resistance

$\mathcal{R}_{w\leftrightarrow t}$ Winding-to-teeth resistance

$\mathcal{R}_{t\leftrightarrow y}$ Teeth-to-yoke resistance

$\mathcal{R}_{y\leftrightarrow h}$ Yoke-to-house resistance

$\mathcal{R}_{h\leftrightarrow c}$ House-to-oil-coolant resistance

$\mathcal{R}_{c\leftrightarrow c_w}$ Oil-coolant-to-water-coolant resistance

$\mathbf{Re}_\phi$ Rotational Reynolds number [-]

T Torque [Nm]

- T_{em} Electromagnetic torque
- T_m Mechanical torque
- T_{loss} Loss torque
- T_{wind} Windage torque
- $T_{converter}$ Braking torque due to converter
- T_{rr} The rolling friction torque
- T_{sl} Sliding friction torque

U_{DC} DC voltage [V]

$\widehat{u}$ Peak voltage [V]

u Time-varying voltage [V]

- u_{abc} Phase voltages
- $u_{\alpha\beta 0}$ Voltages in the stationary reference frame
- u_{diode} Voltage drop over diode
- u_{igbt} Voltage drop over igbt
- u_{dq0} Voltages in the synchronous reference frame

V Volume [m³]

$\dot{V}$ Volumetric flow rate [m³/s]

v_{abc} Phase potentials [V]

x Distance [m]

α_h Second hysteresis constant [-]

α_{Cu} Temperature coefficient of copper [-]

δ skin depth [m]

ζ Temperature [C]

- ζ_{ew} End-winding temperature
- ζ_w Winding temperature
- ζ_t Teeth temperature

ζ_y Yoke temperature

ζ_h Housing temperature

ζ_c Oil-coolant temperature

ζ_{c_w} Water-coolant temperature

η Standard deviation [-]

θ Rotor position [radians]

κ Converter loss torque model constant [Nm· s]

λ Thermal conductivity [W/(m·K)]

μ_0 Permeability of free space [H/m]

μ_{sl} Sliding fiction coefficient [-] (from empirical equation)

μ_{bl} "Constant depending on movement" in sliding friction component equation [-] (from empirical equation)

μ_{EHL} sliding coefficient in full-film conditions [-] (from empirical equation)

ρ Density [kg/(m³)]

σ Electrical conductivity [S/m]

τ Thermal time constant [-]

χ Building factor constant [-]

Φ_{ish} Inlet shear heating reduction factor in rolling bearing friction model [-] (from empirical model)

Φ_{rs} kinematic replenishment/starvation reduction factor in rolling bearing friction model [-] (from empirical model)

Φ_{bl} Weighting factor for the sliding friction coefficient [-] (from empirical model)

ψ Linked magnetic flux [Weber]

ψ_m Magnetic flux linkage due to permanent magnets

$\psi^{(i_d^s, i_q^s)}$ Average magnetic flux linkage as function of the dq-axes stator currents and the PM flux

$\psi^{(i_d^\psi, i_q^\psi)}$ Magnetic flux linkage as function of the dq-axes flux linking currents and PM flux

ω	Electrical angular velocity [rad/s]
ω_m	Mechanical angular velocity [rad/s]
v_{Air}	Viscosity of air [m²/s]
ν_g	Viscosity bearing grease [m²/s]

Vectors and Matrices

$\mathbf{A}$	Matrix in state-space model
$\mathbf{B}$	Matrix in state-space model
$\mathbf{C}$	Matrix in state-space model
$\mathbf{g}$	Gradient vector
$\mathbf{H}$	Hessian matrix
$\mathbf{J}$	Jacobian matrix
$\mathbf{r}$	residual vector
u	Input vector in state-space model
v_1	Input vector 1 for state-space model for simulation
v_2	Input vector 2 for state-space model for simulation
x	State vector in state-space model
y	Output vector in state-space model
Φ_N	Regressor matrix

Chapter 1

Introduction

1.1 Motivation for the research

As the market for electrical vehicles grows bigger, companies and governments allocate more and more resources for development of, and research about, electrical drive trains. Consequently, efficient experimental characterisation and validation of electrical machines for traction become increasingly important. Data from experimental tests are necessary for performance validation of manufactured and purchased machines, building of realistic simulation models and development and optimisation of control algorithms. However, established test procedures are often inefficient in terms of time, space and equipment, and testing of electrical drive trains is therefore generally a costly and time-consuming process. Therefore, the tight competition on the (hybrid) electrical vehicle market calls for cheaper and more time-efficient test methods. Due to these reasons, this thesis presents a study on how interior permanent magnet machines (IPMSMs) can be characterised and modelled by measurements from electro-mechanical and thermal transient operations. The choice of subject gives rise to some enquiries:

- Why IPMSMs?
- Which characteristics, and why are they important?
- Why to use measurements from transient operations?

The next coming sections try to answer these questions in a satisfying manner.

1.1.1 The IPMSM and electrical vehicles

Electrical vehicles put high demands on the electrical machines that are used for propulsion. Some of the most fundamental requirements are

- High torque and power densities that result in reduced machine sizes.
- High efficiencies that extend the ranges of the vehicles and lower the cooling requirements.
- High speed and torque operational spans that are necessary due to the highly dynamic operation of the machines.

Despite the challenging requirements, the automotive industry uses many different types of electrical machines that are considered to fulfil the needs. The different machine types have different advantages and disadvantages: The induction machine is robust but relatively difficult to control, in particular at low speed. The reluctance machines are cheap and robust, but suffer from either poor power factor (synchronous reluctance machines), or high noise and torque ripple (switched reluctance machines). The PMSMs feature very high performances in terms of efficiency and torque density. Designed in the right way, they can also achieve a high constant power region above nominal speed. However, the materials of the permanent magnets (supposing neodymium magnets with boron) are quite scarce, and price and availability introduce an uncertainty to the cost of the machines. Despite this, the PMSM has become one of the most popular machine types for traction applications, and it is therefore selected as the target for the study of this thesis.

Figure 1.1 shows typical topologies of two fundamental design approaches of radial-flux inner-rotor PMSMs: one where the magnets are mounted on the surface of the rotor (SMPMSM) and one where the magnets are embedded (IPMSM). The surface mounted type generally features a higher torque density. Nevertheless, the interior magnets in the IPMSM reduce the risk of mechanical problems when the speed increases. Furthermore, the integrated magnets make the rotor magnetically asymmetrical. The asymmetry yields possibilities to achieve reluctance torque if the machine is controlled in an appropriate way. The reluctance torque contributes to extend the constant power region to speeds significantly higher than the base speed (some studies indicate that the field-weakening region of a SMPMSM can be extended to match the IPMSM, but the high frequency introduce significant eddy currents in the magnets [1]). Due to these properties, many studies chose the V-shaped IPMSM as the favourite machine choice for electrical traction [2–5], and it was therefore chosen as the subject of this thesis. Regardless, it should be added that much of the approaches that are presented throughout this thesis can be applied to any type of synchronous machines. Furthermore, it is possible to extend the methods to include other

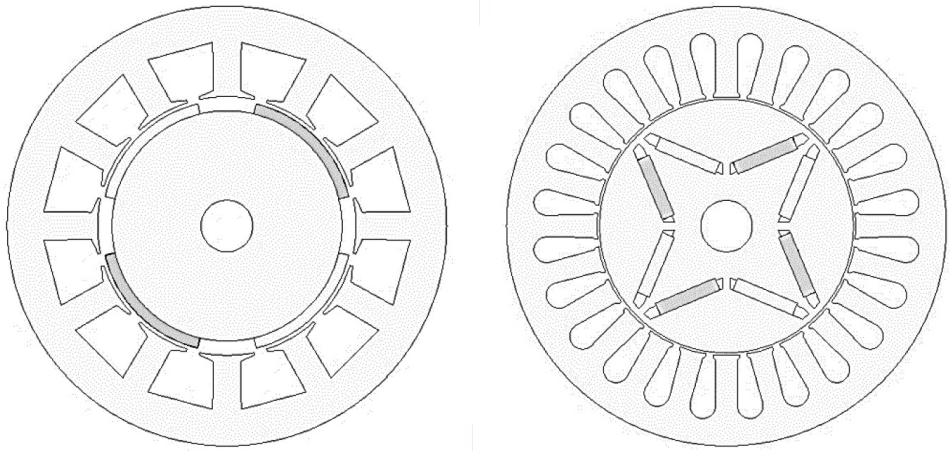

(a) SMPMSM **(b)** IPMSM

Figure 1.1: Typical permanent magnet synchronous machine topologies.

conventional machine types. However, due to time restrictions, these possibilities are not examined in the frame of this work.

1.1.2 Important properties of an IPMSM built for traction

As mentioned above, IPMSMs for traction applications require high torque and power densities, high efficiencies, and wide speed and torque ranges. Furthermore, good cooling attributes, which depend less on generic machine types and more on individual machine designs, are also of utmost importance. The characteristics that dictate the performance of these qualities are

- The electromagnetic properties of the machine, which relate the armature currents to the linked magnetic fluxes and air-gap torques.
- The loss behaviours, which determine the efficiency.
- The cooling properties, which determine the temperature distribution in the machine.

These are the primary aspects that are taken into account during the machine design process, and that need to be evaluated once the machine has been manufactured. This thesis focuses on experimental estimations of these properties, and divide the parts into three different chapters: I) Electromagnetic characterisation, II) loss analysis, and III) thermal

characterisation and modelling. The chapters relate to each other, but can also be seen as standalone analyses of the specific topics.

Thermal perspectives. All three of the aforementioned categories relate to the temperature of the machine in one sense or another. Since the temperature influences the magnetic properties of permanent magnets quite significantly, a magnetic model for a machine at room temperature differs from one at e.g. 100^{o}C. Consequently, it is important to analyse the temperature's influence on the electromagnetic characteristics if the machine design include permanent magnets. Considering the machine losses, they create heat dissipation and therefore yield temperature changes in the machine. It is challenging to find the origin and the magnitude of the losses due to the complex frequency-dependent loss phenomena in the machine. Furthermore, the losses tend to change with the temperature in itself, which further complicates the identification. Therefore, the loss identification strategy needs a lot of attention and fine tuning to yield accurate results. Finally, the cooling and thermal properties obviously relate to the temperature. Challenges lie in finding equivalent lumped parameters and heat-transfer coefficients that can predict the heat flux paths and the temperature distributions in the machines accurately.

Importance of parameter estimation. The paragraphs above imply the importance of the estimation of the aforementioned categories of machine properties:

1. Firstly, the electromagnetic characteristics of a machine decides the maximum speed and torque, and relates specific currents to specific torques. Consequently, information about the characteristics is necessary to design a well-performing control algorithm for the machine;
2. Secondly, information about the losses makes it possible to foresee where and when heat is dissipated during operation. Therefore, insight in the loss behaviour of machines greatly helps to predict when and how much a machine must be cooled;
3. Thirdly, information about cooling and temperature characteristics is paramount to predict how high stator currents and speed a machine can sustain without overheating.

These are the main motivations to the topic of this work.

1.1.3 Testing during transient operation

The general approaches that evaluate the electromagnetic and the loss characteristics of electrical machines work in mechanical steady-state operation. The test object is excited with different current combinations while a load machine keeps the rotational speed constant.

By measuring and comparing the input currents and the torque, and the mechanical and electrical power, one obtains information about the electromagnetic and the loss characteristics of the machine (these procedures are discussed much more elaborately in chapter 2 and 3, respectively, where relevant literature is referred to). The steady-state approach entails some positive features

- Since the machine operates with constant speed, only a few fundamental periods worth of data is sufficient to derive the properties of a test object for the specific loading point.
- The steady-state operation makes it straight forward to estimate the uncertainty of measurement results for specific speeds.

The first point implies that the sampling frequency of the measurements can be very high, which results in accurate measurement results. The second point makes the methods ideal for benchmarking since uncertainty is an important factor for standardisation. However, the steady-state methods also suffer some drawbacks: firstly, they demand very costly equipment. If the high sampling frequency and the uncertainty estimation should give any benefit, the measurement devices must assure a high accuracy (or a low uncertainty). A power analyser and a high quality torque sensor are costly, and they must be regularly calibrated to assure continuing good measurements. Furthermore, the setups require a load machine with the associated drive, which both are expensive and demand a lot of space. In addition, the setup times of the experiments are substantial due to the mounting and alignment of the machines.

Considering the negative aspects of the steady-state tests, it is of interest to find test methods that require minimal equipment, that perform the tests quickly, and that give possibilities to set up the tests in an uncomplicated manner. With this in mind, this thesis investigates the possibilities to remove as much equipment as possible and to characterise the machines with measurements from transient electro-mechanical and thermal conditions, using only industrial current sensors and low-cost voltage measurement approaches. It should be clarified that the ambition is not to find replacements of the conventional methods, but to complement them. As a matter of fact, the transient measurement approaches suffer where the steady-state approaches excel. In particular, it is complicated to estimate the uncertainty of the measurements results from transient operation. With that being said, the possibilities of estimating machine properties from measurements from dynamic operation is an unexplored research area, and it is therefore chosen as the main topic of this thesis.

Regarding the identification of the cooling and thermal characteristics of the machine, there are, in contrast to e.g. efficiency measurement procedures, no methods that are established as benchmark tests. Furthermore, methods to estimate the thermal characteristics during thermal transient operation have been presented quite frequently in the recent years

(chapter gives 3 discusses approaches to derive the thermal characteristics of electrical machines). However, the test methods either depend on similar test setups as the efficiency tests, or require many tests to derive both the steady-state and the transient thermal characteristics of the machines. Therefore, an approach where the total thermal behaviour of the machine can be derived from one test, with minimal equipment, is of interest. The motivation of the thermal characterisation part of this work is therefore

- The lack of a strategy that derives the thermal models with one test and as little equipment as possible.
- The need of a thermal characterisation method to complement the aforementioned methods for an all-inclusive property evaluation of the machine.

1.2 Objectives and Limits

The main objective of this work is to develop tools to obtain the most important characteristics of an IPMSM with 1) as little and as cheap equipment as possible and 2) as fast testing procedures as possible. Furthermore, the characterisation should relate to the temperature of the machine in one way or another. Since this is a very wide objective, limitations are set up to keep the work within a reasonable time frame:

- The work focuses on test methods that evaluate the machines with measurements from dynamic operations;
- One test approach is chosen for each category of the aforementioned machine properties;
- The methods are experimentally evaluated in the frame of what the test facilities of the designated laboratory allows;
- The uncertainty of the results is not evaluated in detail.

The last item on the list above is important since statistical uncertainty estimations are a major part of efficiency tests for e.g. benchmarking and standardisation [6, 7]. For the electromagnetic characterisation tests, the uncertainty is difficult to estimate since the derivation of the magnetic model includes transformation of uncertain variables. Furthermore, the filtering of the data makes it even more complicated – especially if the speed is derived directly from the position. It should however be mentioned that most publications that present similar methods does not include uncertainty in the estimations [8].

The loss estimation results suffer more when the uncertainty cannot be included in the outcome of the tests. Unfortunately, uncertainty is difficult to predict with the presented method since the evaluated machine does not remain at different speeds during the test procedure. Enough samples for each operating point can consequently not be obtained to quantify the uncertainty in a satisfying manner. However, this thesis does not aim to replace conventional test methods when it comes to benchmark testing. Therefore, an approach to obtain accurate results from the dynamic tests can be to calibrate the test setup with results from a method that assures results with low uncertainty outcome[1]. After the calibration, it would still not be possible to quantify the uncertainty of the results from the dynamic tests, but the method could be trusted to give good results in e.g. prototype evaluation and loss modelling.

The thermal characterisation presented in this uses uses thermal PT100 sensors with high intrinsic uncertainty. Furthermore, since the exact placements of the thermal sensors are difficult to predict, the uncertainty of which temperatures that are measured is even higher. Therefore, uncertainty of the supposed measured temperatures becomes almost impossible to quantify accurately.

1.3 Disposition

As mentioned above, this thesis is divided into three chapters that represent three major parts of the complete characteristics of an IPMSM: The electromagnetic characteristics, the loss profile, and the cooling and the thermal properties. Each chapter is approached separately, and they can be read more or less independently. However, the whole work is still closely interconnected: The experimental test procedures of the electromagnetic characterisation and the loss profile identification are very similar, even though the obtained measurements are used in different ways. Therefore, the loss model chapter sometimes refers to the electromagnetic characterisation chapter. Furthermore, the thermal characterisation and modelling chapter relate closely to loss modelling since the losses generate the heat in the machine. The list below gives a short introduction of the chapters

Chapter 2 presents a method to derive the electromagnetic characteristics of IPMSMs. It also gives alternatives to how a magnetic model can be used in practical applications, summarises established methods that derive the characteristics, and proposes techniques to obtain the necessary data for the characterisation;

[1] This also demands a method to derive the moment of inertia of the test objects. However, chapter 3 gives an example of a method that can yield satisfying results.

Chapter 3 shows how a similar test method as in Chapter 2 can be used to derive the loss profile and loss models of machines. Conventional loss testing, manners of calculating losses, and a walk-through of different loss phenomena are also presented;

Chapter 4 describes a method that derives the thermal characteristics of machines during stand still and low-speed operation. In addition, it presents general thermal modelling concepts;

Chapter 5 gives inputs to possible continuation of the work and concludes the thesis.

1.4 Contribution

The main contribution of this work is to show how the most important properties of IPMSMs can be derived from measurements during transient operation. Below follow the most important contributions from each chapter:

Chapter 2

- Validation of methods that quantify the temperature's influence on the electromagnetic characteristics of machines is not common in the literature. Consequently, the biggest contribution of this chapter is to present and validate a method that derives the electromagnetic characteristics of an IPMSM as a function of the temperature relatively easy.

Chapter 3

- Even though a significant amount of studies treat modelling and analyses of losses in machines, the actual loss measurement procedure is rarely discussed as a topic for research. The greatest contribution of this chapter is the presentation and analysis of an alternative method to measure the losses of an IPMSM, which estimates the losses quicker and with less means than established test methods.

Chapter 4

- Most methods that models the thermal behaviour of machines either require extensive measurements with an advanced test setup, or does not include measurement data of winding currents that cause the machine to overheat in steady-state operation. This chapter contributes with a modelling procedure that includes currents over the whole operating range, and that works with relatively simple test equipment. The results give room for a lot of future research, and

the biggest contribution is therefore to present a modelling approach that can be adjusted and extended to fit various setups and applications.

Chapter 2

Electromagnetic characterisation

2.1 Introduction

The electromagnetic properties of an interior permanent magnet synchronous machine (IPMSM) dictate how it performs in terms of maximum torque and speed, and consequently define its possible operational range. Needless to say, detailed information about these properties is necessary to design and evaluate machine topologies in a sufficient way. In the machine design phase, simulation tools give direct feedback on how different machine designs perform with relatively good accuracy: With the fast computers of today, quite advanced simulation techniques, such as finite-element method (FEM) simulations, are introduced in an early stage of the design procedure [9, 10]. When one or a few designs are chosen as prime candidates, time costly 3D simulations yield an even more detailed picture of the machine performance. The aforementioned simulation tools generally predict the electromagnetic characteristics of a machine quite well. However, due to manufacturing tolerances, material propety variations and other unforeseeable phenomena, the true attributes of a machine always deviate from the simulations [11, 12]. Therefore, experimental tests that estimate the characteristics and validate the simulation results should be performed once a machine has been manufactured.

This chapter presents and evaluates an experimental method that derives the electromagnetic characteristics of synchronous machines in general, and for IPMSMs in particular. The procedure aims to test the machines quickly with as little and as cheap equipment as possible. Even though electromagnetic characterisation is an active area in the research community, the temperature is seldom considered as a variable in the estimations. Therefore, the biggest contribution of the chapter lies in showing how the method estimates changes of the electromagnetic characteristics due to the temperature in a straight-forward

fashion.

The first part of the chapter presents the magnetic model, which describes the relationship between the electrical and magnetic properties of the machine, and defines the equivalent circuit model used in this work. The equivalent circuit lays the foundation for not only the magnetic model, but also for the control, which in turn decides the operating points for the loss analyses in the subsequent chapter. Consequently, the author recommends the reader to put effort into understanding the concept behind the equivalent circuit. Later in the chapter, the measurement techniques and processing of the measured data are also discussed in length. This is because 1) a part of the purpose of the thesis is to try to find cheap measurement solutions, 2) the signal processing has a big impact on the final results due to noisy signals, and 3) the same approaches are used for the loss measurements in the next chapter. The list below presents the full content of this chapter:

2.2 **The magnetic model** defines, discusses applications of and present established approaches to derive the magnetic model. Moreover, the section describes the IPMSM equivalent circuit used in this thesis;

2.3 **Dynamic tests for magnetic model derivation** describes the proposed test procedure and discusses measurement approaches and processing of data;

2.4 **Experimental tests** introduces the test setup and presents the experimental results;

2.5 **Summary** suggests possible application where the proposed test method can be used and concludes the chapter.

2.2 The magnetic model

The magnetic model is defined as the relationship between the linked magnetic flux and the currents in the stator windings of an electrical machine in the dq reference frame in this work; the dq reference frame is defined in the following section. Conventionally, inductances together with the linked magnetic flux from the permanent magnets describe this relationship for a permanent magnet synchronous machine as

$$\psi_d - \psi_m = L_d \cdot i_d^s \tag{2.1}$$

$$\psi_q = L_q \cdot i_q^s \tag{2.2}$$

where ψ_m denotes the linked magnetic flux from the permanent magnets, $L_{d,q}$ the stator self-inductances and $i_{d,q}^s$ the stator currents. The use of inductances imply a linear relationship between the currents and the linked magnetic fluxes. However, due to saturation and

cross-coupling phenomena this assumption does not hold in the whole operating range of the machine. Therefore, this thesis generally expresses the linked magnetic fluxes as matrices that are functions of the d- and q-axis currents. An equivalent circuit of the PMSM, which lays the foundation for the equations to derive the magnetic model, is presented in the following section. Furthermore, the section also presents both possible applications of the magnetic model, and established magnetic model derivation methods, to put the work in context. Much of what is presented here can be found in earlier publications by the author (see VII in the list of publications). However, an introduction to the relevant model and equations is important to follow the later sections of the chapter.

2.2.1 Reference frame and equivalent circuit

Reference frames

The electromagnetic equivalent circuits of the PMSM are usually expressed in either abc, $\alpha\beta 0$ or $dq0$ coordinates depending on their propose. An ideal abc model assumes a perfect three phase symmetric system. Mathematically, the voltages of the circuit are expressed as

$$\begin{bmatrix} u_a \\ u_b \\ u_c \end{bmatrix} = \begin{bmatrix} \widehat{u}\cos(\omega t) \\ \widehat{u}\cos(\omega t - \frac{2\pi}{3}) \\ \widehat{u}\cos(\omega t + \frac{2\pi}{3}) \end{bmatrix}$$

where $\widehat{u}$ is the amplitude of the voltage and ω is the electrical angular velocity[1]. In this frame, the voltages are often expressed in root mean square (rms) values, which are given by

$$U_{rms} = \sqrt{\frac{1}{T}\int_t^{t+T} u(t)^2 dt} = \frac{\widehat{u}}{\sqrt{2}} \tag{2.3}$$

for sinusoidal voltages, where T is the time of one fundamental period. The rms values are constant in steady-state operation, and since the system is symmetric, one equivalent circuit, which includes the stator resistance and inductance, and the electromotive force due to the linked magnetic flux from the permanent magnets, is enough to model the whole machine. The model makes it possible to estimate the current and the power straight forwardly assuming that the machine is excited with sinusoidal voltages.

[1]This example transforms the voltages. However, other variables, such as the current and the linked magnetic flux are also transformed in the same manner.

In a conventional three phase machine, the three phases are generally spatially separated by 120 electrical degrees. In any point in time, the three phase voltages u_a, u_b and u_c, which are vectors in the spatial plane, yield a resulting voltage vector when they are added together (if they are added as scalars the results becomes zero). This is illustrated in Figure 2.1, which shows the resulting vector when $\omega t = \frac{2\pi}{3}$.

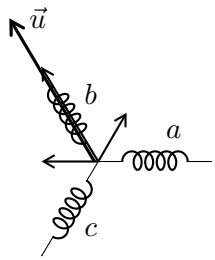

Figure 2.1: The spatial voltage vector at $\omega t = \frac{2\pi}{3}$.

The vector rotates with the angular velocity ω in the spatial plane. Due to the symmetry, the magnitude of the rotational vector remains constant regardless of the time (assuming that the amplitude of the phase voltages are equal and constant). Since the vector rotates in a spatial plane, it can be placed in a two dimensional orthogonal coordinate system. This greatly facilitates analyses of the vector as a function of time. The mathematical operation that derives the orthogonal coordinates from the three phase coordinates is generally denoted the $\alpha\beta 0$ transformation and is formulated as

$$\begin{bmatrix} u_\alpha \\ u_\beta \\ u_0 \end{bmatrix} = k \begin{bmatrix} 1 & -\frac{1}{2} & -\frac{1}{2} \\ 0 & \frac{\sqrt{3}}{2} & -\frac{\sqrt{3}}{2} \\ \frac{1}{\sqrt{2}} & \frac{1}{\sqrt{2}} & \frac{1}{\sqrt{2}} \end{bmatrix} \cdot \begin{bmatrix} u_a \\ u_b \\ u_c \end{bmatrix}$$

where u_α and u_β are orthogonal and u_0 is the zero-sequence voltage that is zero in a perfectly symmetrical excitation of the machine. The parameter k is a scaling factor that can be chosen freely, but is usually $\frac{2}{3}$ which gives a amplitude invariant transformation (the resulting vector amplitude equals the amplitude of the phase quantities), or $\sqrt{\frac{2}{3}}$ which gives a power invariant transformations (the power can be calculated from the current and voltage vectors without scaling). This work uses $k = \sqrt{\frac{2}{3}}$, but much of the published literature uses $k = \frac{2}{3}$. Figure 2.2 shows the $\alpha\beta$ (supposing the zero sequence voltage is zero) coordinates system together with the resulting vector from Figure 2.1. The vector is scaled according to the power invariant transform ($k = \sqrt{\frac{2}{3}}$). Control algorithms often favour constant reference values to time varying in stationary operation. With this in mind, the

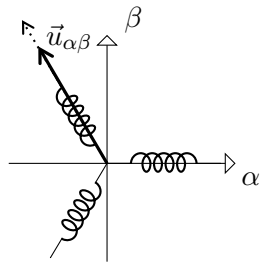

Figure 2.2: The spatial voltage vector in the $\alpha\beta 0$ frame $\omega t = \frac{2\pi}{3}$.

$\alpha\beta 0$ vector can be placed in a reference frame that rotates with the electrical fundamental angular velocity. In the new reference frame, the vectors are constant as long as the amplitude or phase angle of the transformed system do not change. The rotating coordinates are often denoted the $dq0$ or the synchronous coordinates and can be derived by

$$\begin{bmatrix} u_d \\ u_q \\ u_0 \end{bmatrix} = \begin{bmatrix} \cos(\theta) & \sin(\theta) & 0 \\ -\sin(\theta) & \cos(\theta) & 0 \\ 0 & 0 & 1 \end{bmatrix} \cdot \begin{bmatrix} u_\alpha \\ u_\beta \\ u_0 \end{bmatrix}$$

where θ is equal to $\omega t + \zeta$, where ω is the synchronous electrical angular velocity and ζ is the offset that makes it possible to align the coordinate system freely. In the case of permanent magnet synchronous machines, ζ is generally chosen so the d axis of the synchronous coordinate system aligns with the flux from the permanent magnets. Figure 2.3 shows the voltage vector from Figure 2.2 placed in the dq coordinate system (supposing the zero sequence is zero). Due to convenience this work treats the machines in the dq reference frame.

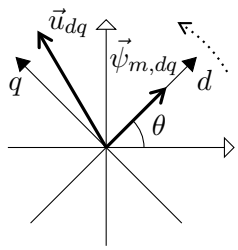

Figure 2.3: The spatial voltage vector in the $dq0$ frame $\omega t = \frac{2\pi}{3}$.

Equivalent circuit for the magnetic model derivation

There exist many designs of equivalent circuits that represent the PMSM in dq coordinates. The most basic circuit only includes the stator inductance and resistance, and the induced voltage due to the linked magnetic flux. More elaborate models include cross-coupling inductance phenomena, equivalent iron-loss resistances, cogging torques, magnetic saturations and spatial harmonics [13–16]. Figure 2.4 shows a graphical representation of the circuits that represent the machine in this work.

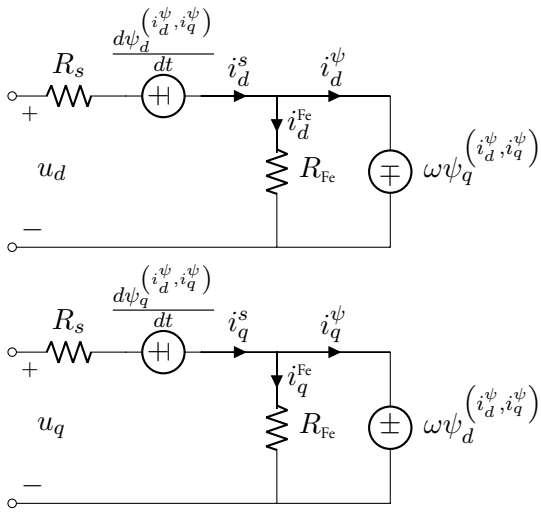

Figure 2.4: Equivalent circuit of the PMSM in the d and q reference frame.

The parameter R_s in the circuits represents the stator winding resistance. This resistance is modelled as a constant, but in reality it changes with the temperature and the frequency. However, these dependencies have a small impact on the magnetic model derivation results when measurements from both generator and motor operation are used, and they are therefore excluded from the model (this is shown in the following section).

The voltage sources in series with the stator resistances represent the electromotive force (emf) that arise when the linked magnetic fluxes in dq coordinates change, and the voltage sources in the rightmost part of the circuits represent the induced emf due to the fundamental angular velocity of the flux linkage. The flux linkage have a non-linear relationship with the dq currents; however, if the magnetic model of the machine is known, look-up tables (LUTs) can provide the values of the linked magnetic fluxes for specific current combinations. Therefore, there is no need to introduce additional parameters to take the saturation and cross-coupling phenomena into account.

The equivalent circuits also feature an iron-loss resistance R_{Fe} in parallel with the voltage

sources that represent the induced voltages. The iron loss resistance models the eddy-current losses due the fundamental component of the linked magnetic flux. However, the actual relationship between the eddy-current losses and the frequency is very difficult to predict (section 3.4.1 in the following chapter discusses this in detail), which implies that the value of R_{Fe} changes with frequency. Consequently, the iron loss resistance is included in the circuits only to give an indication of how the eddy currents affect the linked magnetic flux. In particular, the current flows in different direction through the iron loss resistance depending on the sign of the electrical angular velocity. This, as it is shown in the following section, has implications when the linked magnetic flux is derived from the measurements.

Model equations

Kirchoff's voltage law yields the voltage equations for the circuits in Figure 2.4

$$u_d = R_s i_d^s + \frac{d\psi_d^{\left(i_d^\psi, i_q^\psi\right)}}{dt} - \omega \psi_q^{\left(i_d^\psi, i_q^\psi\right)} \tag{2.4}$$

$$u_q = R_s i_q^s + \frac{d\psi_q^{\left(i_d^\psi, i_q^\psi\right)}}{dt} + \omega \psi_d^{\left(i_d^\psi, i_q^\psi\right)} \tag{2.5}$$

This thesis analyses the machine with constant dq currents. With this in mind the time derivative of the linked magnetic flux is approximately zero, and (2.4) and (2.5) can be rewritten to

$$u_d = R_s i_d^s - \omega \psi_q^{\left(i_d^\psi, i_q^\psi\right)} \tag{2.6}$$

$$u_q = R_s i_q^s + \omega \psi_d^{\left(i_d^\psi, i_q^\psi\right)} \tag{2.7}$$

Reformulations of (2.6) and (2.7) give the magnetic flux from the current, stator resistance, voltage and electrical angular velocity

$$\psi_q^{\left(i_d^\psi, i_q^\psi\right)} = \frac{R_s i_d^s - u_d}{\omega} \tag{2.8}$$

$$\psi_d^{\left(i_d^\psi, i_q^\psi\right)} = \frac{u_q - R_s i_q^s}{\omega} \tag{2.9}$$

According to the equivalent circuits (Figure 2.4), the iron-loss currents $i_{d,q}^{\text{Fe}}$ (where $_{\text{Fe}}$ stands for "iron") changes with the sign of the angular velocity. Consequently, the flux changes

depending on if the machine works as a motor or as a generator, even if the stator currents are the same. However, the change is very small, and the mean value of the generator and motor magnetising currents ends up as approximately i^s_{dq} (where s stands for "stator") independent of how fast the machine rotates, supposing that the magnitude of the angular velocity during motor and generator operation are the same. The mean value of the linked magnetic fluxes can therefore be calculated if the voltages for two angular velocities with opposite signs but equal magnitudes and a specific current combination are known

$$\psi_q^{\left(i_d^s, i_q^s\right)} = \frac{\frac{R_s i_d^s - u_d^{\left(|\omega_\psi|\right)}}{|\omega_\psi|} + \frac{R_s i_d^s - u_d^{\left(-|\omega_\psi|\right)}}{-|\omega_\psi|}}{2} = \frac{-u_d^{\left(|\omega_\psi|\right)} + u_d^{\left(-|\omega_\psi|\right)}}{2|\omega_\psi|} \tag{2.10}$$

$$\psi_d^{\left(i_d^s, i_q^s\right)} = \frac{\frac{u_q^{\left(|\omega_\psi|\right)} - R_s i_q^s}{|\omega_\psi|} + \frac{u_q^{\left(-|\omega_\psi|\right)} - R_s i_q^s}{-|\omega_\psi|}}{2} = \frac{u_q^{\left(|\omega_\psi|\right)} - u_q^{\left(-|\omega_\psi|\right)}}{2|\omega_\psi|} \tag{2.11}$$

where $|\omega_\psi|$ is the magnitude of an arbitrary angular velocity. As seen above, (2.10) and (2.11) do not include the stator resistance in the expressions. Consequently, there is no need to measure the resistance accurately before the tests, and the calculations become less sensitive to changes in the temperature and the angular velocity (supposing that the temperature during motor and generator operation is approximately the same). Furthermore, measurements over the whole speed range can be used and averaged to derive the linked magnetic flux for the specific current combinations.

Apparent and differential inductances

For control purposes, it may sometimes be interesting to formulate the relationship between the linked magnetic fluxes and the currents as inductances. Since the relationships between the currents and linked magnetic fluxes are nonlinear, the inductances must be divided into two types: one that relates the linked magnetic fluxes with the magnitudes of the currents, and one that relates the change of the linked magnetic fluxes with the change of the currents. The first type is called the apparent (or the static) inductance. Mathematically, it can be derived by

$$L_{d\,\text{apparent}}^{\left(i_d^s, i_q^s\right)} = \frac{\psi_d^{\left(i_d^s, i_q^s\right)} - \psi_m}{i_d^s} \tag{2.12}$$

$$L_{q\,\text{apparent}}^{\left(i_d^s, i_q^s\right)} = \frac{\psi_q^{\left(i_d^s, i_q^s\right)}}{i_q^s} \tag{2.13}$$

where the linked magnetic flux from the permanent magnets is approximated by

$$\psi_m = \psi_d^{\left(i_d^s=0, i_q^s=0\right)} \tag{2.14}$$

The second type is called the differential (or the dynamic) inductance. Since there often exists a magnetic cross-coupling between the d and q axes, four differential inductances must be identified

$$L_{dd\text{ differential}}^{\left(i_d^s, i_q^s\right)} = \frac{\partial \psi_d^{\left(i_d^s, i_q^s=\text{constant}\right)}}{\partial i_d^s} \tag{2.15}$$

$$L_{qq\text{ differential}}^{\left(i_d^s, i_q^s\right)} = \frac{\partial \psi_q^{\left(i_d^s=\text{constant}, i_q^s\right)}}{\partial i_q^s} \tag{2.16}$$

$$L_{dq\text{ differential}}^{\left(i_d^s, i_q^s\right)} = \frac{\partial \psi_d^{\left(i_d^s=\text{constant}, i_q^s\right)}}{\partial i_q^s} \tag{2.17}$$

$$L_{qd\text{ differential}}^{\left(i_d^s, i_q^s\right)} = \frac{\partial \psi_q^{\left(i_d^s, i_q^s=\text{constant}\right)}}{\partial i_d^s} \tag{2.18}$$

The dynamic inductances can be used for e.g. online setting of gains for optimal dynamic performance of current controllers.

2.2.2 Applications of the magnetic model

Control

The primary purpose of the magnetic model is to help with the design of optimal current control algorithms. Since the stator currents together with the linked magnetic fluxes yield the torque, the currents can be controlled to obtain the desired torque at specific speeds if the magnetic model of the machine is available. The equation below expresses the torque of an IPMSM as a function of the magnetic flux and the current

$$T_{em} = n_{pp}\left(\psi_d^{\left(i_d^\psi, i_q^\psi\right)} i_q^s - \psi_q^{\left(i_d^\psi, i_q^\psi\right)} i_d^s\right) \tag{2.19}$$

where n_{pp} is the number of pole pairs. A rewrite together with the simplification from (2.1) and (2.2) give

$$T_{em} = n_{pp}\left((L_d i_d^s + \psi_m) i_q - L_q i_q^s i_d^s\right) \tag{2.20}$$

that can be rewritten to

$$T_{em} = n_{pp}\left(\psi_m i_q^s + i_q^s i_d^s (L_d - L_q)\right) \tag{2.21}$$

where $\psi_m i_q^s$ and $i_q^s i_d^s (L_d - L_q)$ are called the permanent magnet and the reluctance torque, respectively. Equation (2.21) indicates that many current combinations result in the same torque. Consequently, control strategies can be designed to chose different currents for different purposes. The most established strategy – the max torque per amp (MTPA) algorithm – aims to create as much torque as possible with as little current as possible [17]. The absolute value of the total current vector is formulated as

$$|i^s| = \sqrt{i_d^{s2} + i_q^{s2}} \tag{2.22}$$

The goal is to minimise (2.22) for a certain torque. Since the simplest torque control algorithms generally adjusts the q-axis current to achieve a requested torque, it makes sense to express the d-axis current as a function of the q-axis current that achives the required torque with as little total current as possible [18]. To achieve this, (2.21) is firstly rewritten so that i_d becomes a function of i_q and T. Secondly, the i_d in (2.22) is replaced by the new expression, and the result is derivated and put equal to zero; this operation creates a relationship between the torque and the q current. Mathematically, the process can be described as

$$|i^s| = \sqrt{\left(\frac{\frac{T_{em}}{n_{pp}} - \psi_m i_q^s}{i_q^s (L_d - L_q)}\right)^2 + i_q^{s2}} \tag{2.23}$$

$$\frac{d|i^s|}{di_q^s} = 0 \rightarrow \tag{2.24}$$

$$T_{em} = n_{pp} 0.5 i_q^s \left(\psi_m + \sqrt{\psi_m^2 + 4 i_q^{s2} (L_d - L_q)^2}\right) \tag{2.25}$$

When the relationship between the torque and the q-axis current is available, a substitution of (2.25) into (2.21) gives the d-axis current reference as a function of the q-axis current reference in the control algorithm

$$i_d^* = \frac{0.5\left(\psi_m + \sqrt{\psi_m^2 + 4(L_d - L_q)^2 i_q^{*2}}\right) - \psi_m}{(L_d - L_q)} \tag{2.26}$$

where i_d^* and i_q^* are the d- and q-axis current references, receptively. Equation (2.26) yields the MTPA trajectory supposing constant inductances, which can be a sufficient approximation in some operating points. However, there are many situations where (2.26) does not hold. Figure 2.5 shows a graphical representation of the MTPA curve together with limitations for currents and flux-linkages as functions of the angular velocity, and lines that show current combinations that give specific torques.

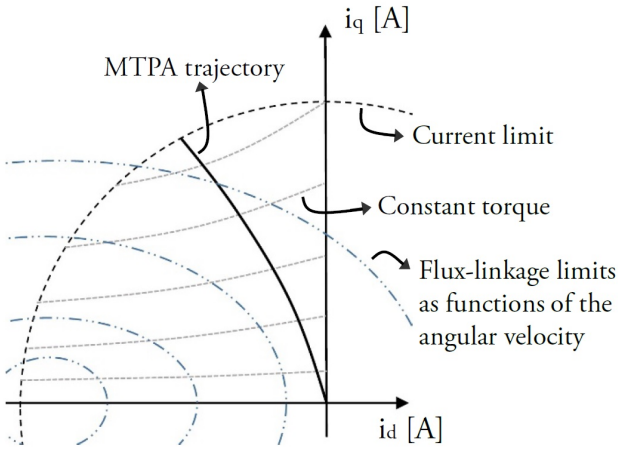

Figure 2.5: Typical MTPA curves for IPMSMs.

The feasible operational area is within the flux-linkage and current limit circles. These limits change the relationship between the d- and q-axis currents: the q-axis current becomes a function of the d-axis current when the machine reaches the maximum linked magnetic flux for a certain torque and speed since field weakening dictates the possible current combinations. Furthermore, the maximum current circle puts a definitive limit to the maximum torque. In addition to this, the apperant inductances change significantly in overload operation. To overcome these problems, the literature suggests different methods to estimate the machine parameters online, which is generally achieved with signal injections or analysis of the back emf [19, 20]. However, online identification introduces more complexity to the control system, which can be a drawback due to an increased computational load. Therefore, the analytical approach to obtain the MTPA trajectory (or any control trajectory) online can be problematic.

Another strategy uses look-up tables (LUTs) to find the MTPA current combinations. The LUTs can be calculated offline if the aforementioned linked magnetic flux matrices together

with the DC-link voltage, the modulation strategy of the pulse-width modulation (PWM) and the current limit are known. The objective is to minimise the currents for specific torques and speeds while staying within the given constraints: The maximum current limit cannot be breached and the magnitude of the voltage vector related to the applied currents and the angular velocity cannot trespass the maximum voltage. Consequently, the derivation of the LUTs becomes a constrained optimisation problem where (2.22) is the objective function that should be minimised. The optimisation is subject to three hard constraints: equation (2.19) sets an equality constraint for a certain torque, and the maximum current and voltage set two strict inequality constraints

$$i^s_{max} > \sqrt{i^{s2}_d + i^{s2}_q} \tag{2.27}$$

$$u_{max} > \sqrt{u^2_d + u^2_q} \tag{2.28}$$

where i^s_{max} is the maximum stator winding current, generally limited by the power converter or temperature constraints of the windings, and u_{max} is the maximum voltage. The voltage is limited by the DC-link voltage and depends on the modulation strategy of the PWM. With a symmetrical suboscillation modulation (see Appendix C) and a power-invariant transformation of the voltages the limit is given by

$$u_{max} = k_{max}\frac{U_{dc}}{\sqrt{2}} \tag{2.29}$$

where k_{max} is a factor that allows for a margin between the magnitude of the maximum resulting voltage vector and the absolute voltage limit of the system. The solution to the aforementioned optimisation problem yields tables with the dq-axes current references as functions of the torque and the speed. The dq-axes current references are obtained online by

$$i^*_d = f_d(n, T_{em}) \tag{2.30}$$

$$i^*_q = f_q(n, T_{em}) \tag{2.31}$$

where i^*_d and i^*_q are the controller references for the dq-axes currents, n is the rotational speed and f_d and f_q are interpolation functions for the LUTs. These functions give the optimal currents as defined by the objective function if the DC-link voltage is constant. However, it is not uncommon that the DC-link voltage from a battery varies quite significantly during operation. Therefore, it is often preferable to make the LUTs functions of the maximum voltage divided by the magnitude of the angular velocity rather than the

speed [21]. Note that a voltage divided by the angular velocity can be interpreted as a linked magnetic flux. Consequently, the division gives an indication to the maximum allowed flux linkage for the specific operational point (see Figure 2.5 for a graphical illustration of these limits). The maximum linked magnetic flux is derived as

$$\psi_{max} = \frac{u_{max}}{|\omega|} \tag{2.32}$$

and the new dq-axes currents reference functions become

$$i_d^* = f_d(\psi_{max}, T_{em}) \tag{2.33}$$
$$i_q^* = f_q(\psi_{max}, T_{em}) \tag{2.34}$$

It is possible to take other aspects, such as the temperature dependence of the remanent flux and the magnetic coevercity of the magnet into account in the optimisation procedure. However, this adds another dimension to the LUTs, which in turn results in heavier computational load for the interpolation algorithms online. It should also be added that the objective function does not necessarily need to minimise the current. It can for example be formulated to minimise the losses in the machine or the whole motor drive system [22].

Temperature tracking

The magnetic model of the machine is temperature dependent mainly because the remanent flux and the magnetic coercivity of the permanent magnets change with the temperature [23]. As a consequence, it is possible to track the temperatures of the permanent magnets if the d-axis flux can be estimated online. Such parameter estimations are possible to perform if current pulses are injected in the system[2] [25]. However, the pulses can have a negative impact on the performance of the machine and introduces complexity to the control system. Nevertheless, it is possible to derive d-axis linked magnetic flux in steady-state without knowledge of the resistance value if the q-axis linked magnetic flux is known. Since the permanent magnet flux is aligned with the d axis, the temperature has a significantly higher impact on the d-axis compared to the q-axis flux (this is confirmed in the result section later in the chapter). Considering the q-axis flux to be known, the d-axis flux can be estimated by

[2]In steady-state, there are three temperature-dependent variables, the dq-axes fluxes and the stator resistance, but only two equations, and identification is consequently impossible [24].

$$\psi_d^{\left(i_d^\psi, i_q^\psi\right)} = \frac{u_q^* - \frac{i_q^s}{i_d^s}(u_d^* + \omega\psi_q^{\left(i_d^\psi, i_q^\psi\right)})}{\omega} \tag{2.35}$$

where u_d^* and u_q^* are the voltage reference values of the controller, ω is the electrical angular velocity, i_d^s and i_q^s are the currents and $\psi_d^{\left(i_d^\psi, i_q^\psi\right)}$ and $\psi_q^{\left(i_d^\psi, i_q^\psi\right)}$ are the linked magnetic fluxes in the stator windings. A comparison between the estimated d-axis flux and a LUT provides information about the permanent magnet temperature. In the next iteration, the q-axis flux is given by the previous temperature estimation and the dq-axes currents through another LUT, and (2.35) together with the first LUT can once again estimate the temperature. Since (2.35) divides i_q^s with i_d^s, the algorithm does not give sufficient results when the d-axis current is low. However, salient-pole IPMSMs are rarely operated with a low d-axis current, except when the torque reference is zero, since that yields a non-optimal current control. Consequently, the temperature tracking should not be engaged with a too low torque reference, but works sufficiently when the torque increases. On another note, the estimation also demands a good compensation for the dead-times and non-linearities of the power converter to make sure the reference voltages correspond to the actual phase voltages as much as possible. Nevertheless, such compensations are generally included in control algorithms for applications that demand high performance (e.g. for automotive applications). There should also be a low-pass filter after the output of the temperature LUT since the estimation of the d-axis flux is sensitive to noise. However, the dynamics of the permanent magnets' temperatures are so slow that the bandwidth of the filter can be low enough to give a stable temperature estimation.

The procedure above gives a hypothetical example of how the magnetic model can be used to derive the temperature of the permanent magnets in PMSMs. The method has not been implemented and tested, but indicates that it is theoretically straight forward to use the magnetic model results in this context. Future work lies in investigating such possibilities further.

Additional use

In addition to help with current control strategy design and temperature tracking, the magnetic model can be compared with simulation models to confirm their validity. The magnetic model gives a clear indication if the flux characteristics of the simulations are modelled correctly, which in turn is important for accurate efficiency simulations.

2.2.3 Established methods to derive the magnetic model

Electromagnetic characterisation of PMSMs has been an active research area in recent years and still is; especially autonomous tests without extra equipment (often called self-commissioning) and online methods attract alot of attention. This is mainly due to the increased interest in applications such as electrical vehicles where the machine operates over a wide speed and torque range. Both self-commisioning and online methods are often designed to work after the machine is installed. Post-installation testing makes it possible to optimise the current control algorithm of the machine continuously throughout the machine's lifespan, and it is also possible to track changes in e.g. the linked flux from the permanent magnets to control the health of the machine. However, offline charcterisation before installation, e.g. evaluation in the end of a production line, are also important since the magnetic model characteristics give possibilities to develop control methods, and to find eventual defects in the machines in advance of operation. There exist many publications on the subject of electromagnetic characterisation which of a few that the auther finds most representative are refered to in the following section. An elaborated walkthrough of magnetic model identification methods can be found in [8].

Online methods

Experimental methods to derive the magnetic model of PMSMs are generally divided up into two main categories: online methods, which characterise the machines during operation, and offline methods. Online parameter identification is a powerful tool for e.g. sensorless control and condition monitoring of machines [25, 26]. The parametrisation builds upon real-time system identification strategies such as recursive least-square identifications, extended Kalman filters and model-reference based minimisation amongst others [24, 26]. The methods do not necessarily need initial values of the parameters, but generally perform better when good first estimations are available. The approaches cannot derive all parameters during steady-state conditions and therefore work during either transient conditions or with signal injection (alternatively, some parameters are excluded from the identification). Even though the online methods are interesting and relevant, this work focuses on offline methods that can be used for end-of-line testing and state-of-health tests. However, a combination of a look-up table (LUT) based current controller and an online identification scheme to control the validity of the LUTs would be interesting as future work.

Offline methods

The offline methods can be divided up in three categories: tests during constant speed, during standstill and during acceleration and/or braking.

1. **Constant-speed methods.** The constant-speed methods generally involve a load machine to keep the speed of the test object constant even though the currents, and consequently also the torque, change. The most straight-forward method assumes a constant resistance and obtains the flux linkages from (2.8) and (2.9) [27–29]. Unfortunatly, both the stator resistance and the permanent magnet flux vary with temperature. These variations cause uncertainties in the estimations. However, temperature models can be used to foresee the temperature's influence, and the change can consequently be compensated for in the identification [30]. Furthermore, the problem with changes in the stator resistance due to temperature can be solved by using measurements from both generator and motor operation: If the d-axis current remains, but the q-axis current changes sign (maintaining the same amplitude), it is possible to derive the fluxes similarly as in (2.10) and (2.11) [31]. This removes the need for information about the resistance of the stator windings as long as the temperature of the conductors does not change significantly between the two operating points. The biggest drawback of constant-speed methods is the extensive equipment and time costly installation they entail. Therefore, they are most applicable to prototype or benchmark testing where the machines are evaluated thoroughly.

2. **Standstill methods.** The standstill methods do not demand an additinal load machine and can derive the magnetic model of the test object after installation, supposing that the current controller software can be modified to meet the needs of the methods. Traditionally, the methods require a locked rotor. However, recent publications generally evaluate the methods without locking the rotor with good results. To take saturation and cross-coupling phenomena into account in the results, a DC voltage with a superimposed AC signal with an appropriate frequency can be applied to the machine. The relationship between the amplitude and frequency of the AC voltage and the resulting AC current yields the inductances [32, 33]. The methods perform well without locking the rotor supposing the excitation voltages are applied in a sufficient manner. Another approach excites the machine with a hysteresis current controller which applies a square voltage wave to the machine. The flux can be obtained by integrating the voltage minus the voltage drop due to the stator resistance [34, 35]. These methods generally perform very well without locking the rotor supposing that the square voltage wave alternates from positive to negative values with a sufficiently high frequency. However, the integration might give rise to drifting that must be taken into account when the fluxes are estimated. An obvious drawback of the standstill methods is that the magnetic flux from the permanent

magnet cannot be estimated but must be known beforehand. This is problematic since the permanent magnets are the component of the machine which electromagnetic characteristics are most likely to change over time.

3. **Dynamic methods.** The last category of magnetic model characterisation strategies, which is the least investigated, performs the tests when the machine accelerates and/or brakes [36]. A dq current combination is applied to the stator windings, whereupon the machine accelerate freely due to the torque the currents generate. Once the machine reaches a certain speed, new currents, which generate a torque in the opposite sign compared to the first, are applied. With a sufficient current sequence, data from both acceleration and braking can be used to derive the magnetic model without knowing the value of the stator resistance. These methods avoid the drawbacks of both the constant-speed and the standstill procedures: they do not demand a load machine and time demanding test setups, and they include the linked magnetic flux from the permanent magnets in the identification. However, post-installation testing requires that the shaft of the machine can be decoupled from the load (if the load cannot rotate freely). Furthermore, the mechanical dynamics of the rotor might be very fast if the torque is high compared to the moment of inertia of the rotating parts of the machine. The method presented in this thesis, which we call the dynamic test method, is a part of this category of magnetic model identification strategies.

2.3 The dynamic test method for magnetic model parameter determination

The dynamic test method evaluates a machine with measurements from when it accelerates and brakes, and the only thing that limits the mechanical dynamics during the tests is the moment of inertia of the rotating parts. As a consequence, the shaft of the test object does not have to be connected to a dynamo that assures a constant speed throughout the test, and the complexity of the test setup is thereby significantly reduced. The exact value of the moment of inertia of the rotating parts is irrelevant since it does not yield any necessary information to estimate the linked magnetic flux of the machine[3]. However, the moment of inertia must be high enough so that the rotor does not reach the maximum speed too quickly. On the other hand, it is desirable to make the tests as short as possible to avoid an increase in temperature in the windings and in the permanent magnets of the machine. The following section describes the approach of this work.

[3]However, an estimation of the mechanical torque on the rotor shaft requires detailed knowledge about the moment of inertia. This is discussed further in chapter 3.

2.3.1 Test execution

The list below describes the test sequence that has been used throughout this work

1. **The machine is accelerated up to a pre-defined speed**. A speed controller accelerates the machine until the pre-defined speed is reached.
2. **The test currents are applied to the machine**. The test currents brake the machine towards zero speed and continue to accelerate the machine in the opposite rotational direction until it reaches the pre-defined speed.
3. **The machine is braked back to zero speed**. A speed controller brakes the machine back to standstill.

The rotor position and the voltages are measured during the sequence, and a post-processing procedure estimates the magnetic model from measurements from point 2 in the list above.

Figure 2.6 shows an example of the part of the dynamic test sequence that is used for the magnetic model derivation (point 2 in the list above). This test evaluates the current combination $i_d = -40$ A, $i_q = 20$ A. The active part of sequence (point 2) takes about 0.65 seconds to perform. Together with the starting acceleration up to -1750 rpm (point 1 in the list above) and the braking from 1750 to 0 rpm (point 3 in the list above) the complete sequence takes about 1.5 seconds to execute. Considering a resting time around 2 seconds between the current combinations it takes less than six minutes to evaluate 100 current combinations (the testing time is of course dependent on how much torque the currents create, the maximum speed and the moment of intertia of the rotating part of the machine).

As Figure 2.6 shows, the voltages in the dq frame contain significant harmonics. The harmonics are expected since the induced voltages in the machine are non-sinusoidal: The current controller aims to keep the currents as sinusoidal and consequently tries to generate inverter voltages that follow the induced voltages as much as possible; notice that the currents contain much less harmonics than the voltages. Since the harmonics do not contain information that is relevant for the magnetic model estimation, they should be filtered in an appropriate way before the calculations. Section 2.3.3 discusses the post-processing procedure of the measured data.

Alternative Sequences

The previous section presents one example of a dynamic test sequence. The sequence is designed for easy implementation and to avoid that the iron losses influence the results. It

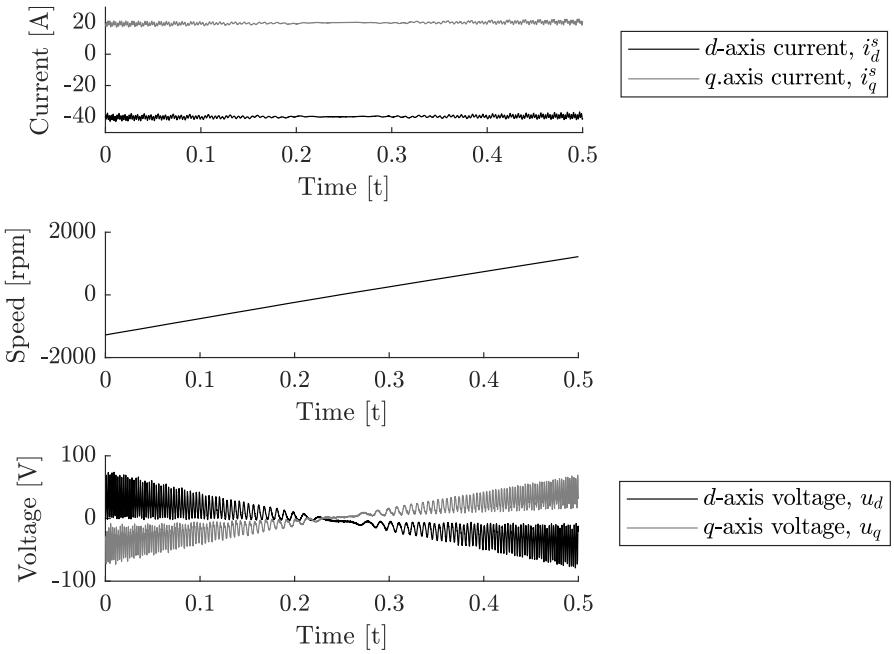

Figure 2.6: A dynamic test sequence.

is however possible to design the sequence in different ways. An example of an alternative design accelerates and brakes the machine with the same rotational direction [36]. This approach makes it possible to shorten the sequence, and some position error sensitivity can be eliminated. However, with such an approach the iron losses can affect the results negatively. This can be understood by considering the equivalent circuits of the IPMSM (Figure 2.4). Since the rotational direction does not change, the induced voltages maintain the same sign throughout the whole sequence. Consequently, the signs of the iron loss currents ($i_{d,q}^{\text{Fe}}$) also remain. This results in magnetising currents ($i_{d,q}^{\psi}$) which are either always greater or smaller than the stator currents ($i_{d,q}^{s}$). On the contrary, if rotational direction changes but the currents remain, which is the case in the algorithm that is proposed in this work, the sign of the iron loss currents change. As a consequence, the magnetising currents are higher than the stator currents in one rotational direction, but smaller in the other. Therefore, the impact of the iron losses almost disappears if measurements from both generator and motor operation are used in the derivation. In the end, the test sequence should be designed to suit the intended application as good as possible.

Current control and overlying algorithm

The mechanical dynamics of the machines potentially become very high during the tests, and the current controller of the drive system must consequently perform well during high accelerations and retardations. The direct current controller (DCC) meet these prerequisite in a satisfactory way (see paper IV in the list of publications). Nevertheless, due to the variable switching frequency the DCC is rarely used in automotive applications. Instead, the field oriented PI controller (FOC) is a more common alternative. However, without knowledge of the magnetic model of the machine, accurate estimations of the induced voltages cannot be feedforwarded in the FOC algorithm. This leads to bad load disturbance rejection performance and the controller becomes sensitive to fast accelerations. On the other hand, if the linked flux is approximately known – either from background data, or from a first test iteration where one accept a drift in the current – the emf can be estimated. In previous works the author performed tests with the DCC, but all the tests of this work were made with an FOC; see Appendix C for a thorough description of the current controller. The FOC was chosen as control because of three reasons:

1. Most variable speed drive control systems work with some kind of pulse width modulation based current controller that needs feedforwarding to perform well. Consequently, if machines should be tested after installation, the method would probably run with a controller similar to the FOC.
2. Since the FOC works with constant switching frequency it is easier to obtain a quasi-instantaneous mean value of the voltage (it is straight forward to integrate over one switching period since the switching frequency is constant and known).
3. The reference value of the FOC can be used directly to derive the magnetic model.

To obtain accurate results, the whole range of tests is run twice. In the second iteration, the estimated linked magnetic flux from the first iteration is used to feed forward the induced voltage to the current controller. This enhances the performance of the controller and makes the currents more equal to their references. Consequently, the estimated relationship between the currents and the linked magnetic fluxes becomes more accurate. In addition, the temperature of the test object is measured before the testing: Since the tests are so quick the temperature does not increase much during each iteration. However, if the machine is tested quickly with many testing points with high current, the temperature might increase significantly from the first current combination to the last. The temperature measurements are necessary for a detailed evaluation of the temperature characteristics of the machine, but can be left out for e.g. fast in-situ testing. Figure 2.7 shows the overlaying algorithm of the magnetic model identification that was used throughout this work.

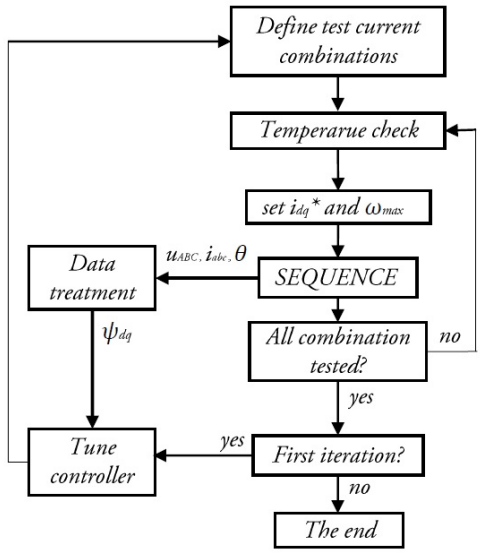

Figure 2.7: Overlaying algorithm for the magnetic model derivation.

2.3.2 Parameter measurements

As mentioned above, the obtained voltage and position data from the dynamic test sequence contain the necessary information to derive the magnetic model. Therefore, it is worth to describe approaches to measure these parameters. This section discusses measurement techniques in general, but focuses on the methods that were used during the experiments of this work.

Position measurements

The choice of position sensor and demodulation technique can influence the results of the magnetic model derivation quite much. If there already exists a position sensor installed on the machine it can be used for the testing (this is a prerequisite for a machine already installed in a vehicle). In the case of traction IPMSMs a resolver, which was employed during the experiments of this work, is frequently used. A resolver works as a rotating transformer. An excitation signal in the rotor windings induces voltages in two stator windings that are positioned in quadrature. The amplitudes of the induced voltages in the two windings give information about the rotor position as

$$u_{r1} = \widehat{u} \sin \omega_e t \sin \theta \tag{2.36}$$
$$u_{r2} = \widehat{u} \sin \omega_e t \cos \theta \tag{2.37}$$

assuming that the resolver has the same number of poles as the machine. The parameters ω_e and θ in (2.36) and (2.37) are the excitation angular velocity and the rotor position, respectively. The first step to obtain the position from u_{r1} and u_{r2} is to remove the excitation signal ($\sin \omega_e t$). The most straight forward way to achieve this is called the fringe detection technique (FDT) [37]. The FDT measures u_{r1} and u_{r2} when $\sin \omega_e t$ reaches its peak, which results in signals that are only functions of the peak value the of voltages $\widehat{u}$ and the rotor position θ. After the excitation signal is removed, an arctangent operation on the obtained signals yields the rotor position as

$$\hat{\theta} = atan \left(\frac{\widehat{u} \sin \theta}{\widehat{u} \cos \theta} \right) \tag{2.38}$$

where zero division is avoided using the CORDIC algorithm [38]. This demodulation method is generally called the trigonometric method. The trigonometric method tends to give quite noisy results if it is used in environments with a lot of disturbances. Instead, the general recommendation is to use a angle tracking observer (ATO) for demodulation [39]. Figure 2.8 shows a flowchart that describes the concept of the ATO.

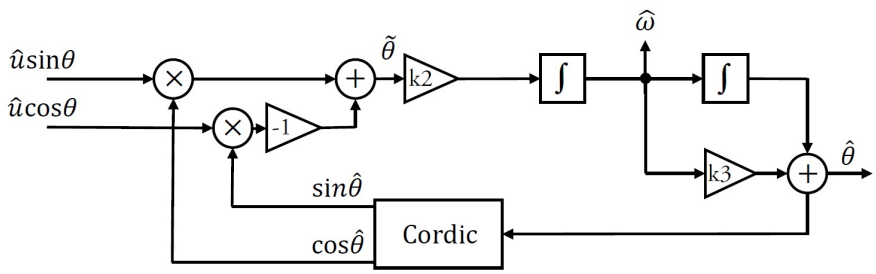

Figure 2.8: Flowchart of the basic angle-tracker-observer algorithm.

The estimated position error, which is calculated by (supposing $\widehat{u} = 1$ for convenience)

$$\tilde{\theta} = \theta - \hat{\theta} \approx \sin(\theta - \hat{\theta}) = \sin \theta \cos \hat{\theta} - \cos \theta \sin \hat{\theta} \tag{2.39}$$

is suppressed by the feedback loop. In addition to a more stable angle derivation, the ATO also gives a direct and accurate estimation of the angular velocity. However, the ATO also imposes a small delay on the angle derivation during mechanical dynamic conditions, which is unfavorouble for dynamic testing applications [40]. There exist techniques to compensate for the delay in the ATO, but due to the simplicity of the algorithm and the controlled environment, the trigonometric method is chosen as the demodulation technique throughout this work.

As in all experimental procedures that derive the electromagnetic characteristics of a PMSM, the results from the dynamic tests are sensitive to disturbances in the rotor position measurements. Typical disturbances of the position measurements include

- A constant offset of the position.
- A position error that depends on the speed.

Figure 2.9 shows illustrations of the impacts of the disturbances.

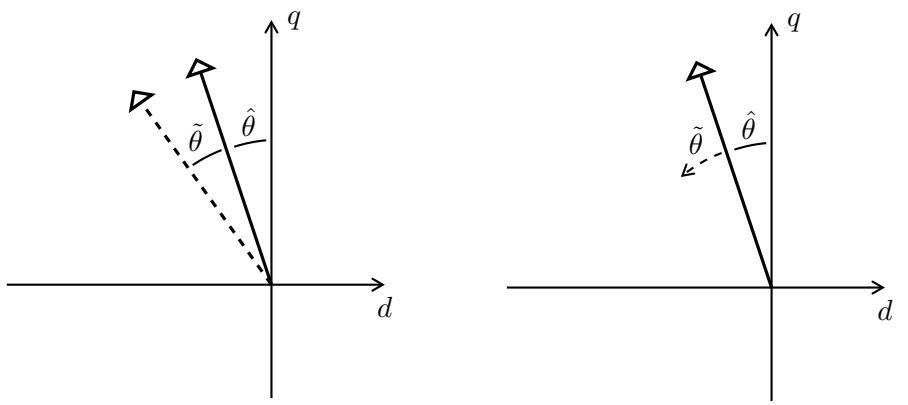

(a) Shift in torque angle due to offset in the resolver measurements. $\hat{\theta}$ is the estimated angle and $\tilde{\theta} + \hat{\theta}$ is the actual.

(b) Shift in torque angle due to speed-dependent error in the position demodulation. $\hat{\theta}$ is the estimated angle and $\tilde{\theta} + \hat{\theta}$ is the actual.

Figure 2.9: Impact of errors in the position measurements.

A constant position error (Figure 2.9a) normally occurs when the d axis in the dq coordinate system is not aligned with the linked magnetic flux from the permanent magnets. This make the apparent synchronous coordinate system differ from the actual. Consequently, the linked magnetic flux maps become erroneous. The errors have especially severe impacts in the high field weakening region since the q current – which affects the torque significantly – changes the most. Figure 2.9a shows an example of how an error in the positions measurements changes the operating point of the machine.

A speed-dependent position error (Figure 2.9b) occurs when the rotor of the machine has time to rotate before the position is demodulated and used in the dq transformations. Since the demodulation and time between the sampling and the transformation is constant, the error increases with the speed. Furthermore, the direction of the rotation influences the direction of the error. Figure 2.9b shows an example of how a speed-dependent position error causes the operating point to change depending on the speed.

Voltage measurements

Phase voltages of machines connected to switching power converters are not trivial to measure due to their rapid dynamics. The voltages are typically measured with high bandwidth voltage probes, but the conversion between analog measurements to digital signals need to be significantly faster than the converter switching frequency to obtain a satisfactory number of samples per switching period. Furthermore, the A/D converters also need high resolutions for accurate measurements. Considering this, the amount of saved data per second can be overwhelming. If the data is processed in real-time in steady-state – as is the case with power analysers and oscilloscopes – this does not introduce a problem since only a few fundamental periods of the voltage must be stored continuously. However, if the data must be saved over a complete dynamic test cycle, the size quickly becomes unhandable.

One way to overcome this problem is to integrate the voltages in real time and save the mean value for each switching period. The integration greatly reduces the data that must be saved, and it also yields enough information about the voltage to derive the magnetic model of the test object. However, even though fast and accurate A/D converters can achieve highly accurate voltage measurements with a reasonable size, they are expensive, and the signal processing of the instantaneous measurements can be challenging. With this in mind, other methods for obtaining the voltage are looked into. Three main approaches are considered here:

- **Analog circuits**. Traditionally, analog circuits have been used to perform the integration of the voltages due to lack of fast analogue-to-digital (A/D) converters of a reasonable price, and they still give good results in controlled laboratory environment [41, 42]. The circuits can achieve good accuracies, but are sensitive to electromagnetic interference and changes in the temperature.

- **Duty-cycle measurements**. Another approach uses differential probes on each converter leg to observe when the actual switching occurs. The switching instances then yield the duty-cycles of the three converter legs. When the duty-cycles are known multiplications between the cycles and the converter DC-link voltage give an approximation of the mean value of the voltage of each switching period. This approach

takes all dead-time effects and delays that can occur from the controller to the actual switching instance into account. However, compensation for the voltage drops over the semiconductor devices and rise and fall times are still necessary. This can be done straight forwardly if datasheet information of the semi-conductor devises are available.

- **Current controller voltage references**. The voltage reference signals from the current controller gives the most easily accessible estimations of the phase voltages. If the nonlinearities of the converter are compensated for by the controller, the references can give a very good approximation of the mean value of the voltages for one switching period. The approach is especially attractive when an already installed machine and drive performs self-commissioning without being separated from its application.

Since one of the main purposes of this work is to make the measurements as simple and cheap as possible, the two last procedures (the duty-cycle measurement approach and the reference values) are chosen as voltage estimation methods. It should be mentioned that earlier publications discuss the impact of voltage measurements quite extensively and reach the conclusion that the duty-cycle measurements yield quite inaccurate results [29, 31]. However, these publications fail to take the voltage drops over the semiconductor components into account.

To clarify the duty-cycle measurement procedure, Figure 2.10 presents the different variables that are used to estimate the voltages.

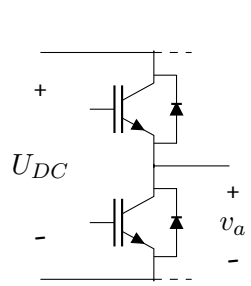

(a) Voltage measurement clarification.

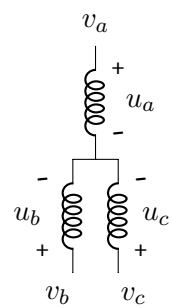

(b) Simple equivalent model.

Figure 2.10: Converter and machine voltages defined.

High-bandwidth differential voltage probes, connected to high-speed digital inputs, measure v_a, v_b and v_c. The digital signals give information about if the voltages are close to U_{DC} (which gives a digital 1) or to zero (which gives a digital 0). When the control system

obtains the signals an algorithm accumulates the digital ones and zeros over one switching period and divides by the number of samples. The operation yields the duty cycle of each converter leg. A multiplication between dutycycles and U_{DC} together with compensations for the voltage drops over the semi-conductor components give estimations of v_a, v_b and v_c.

The voltage drop over the semi-conductor components can be estimated if the sign of the current is known. Figure 2.11 illustrates the resulting voltage drops depending on the current (the current does not flow through the IGBT and diode at the same time – when the IGBT opens the current flows through the free-wheeling diode when the magnetic energy in the machine starts to discharge).

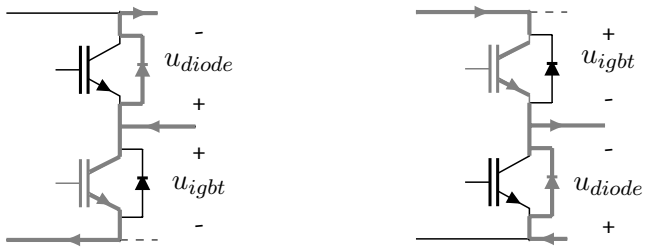

(a) Voltage drops when the current is negative.

(b) Voltage drops when the current is positive.

Figure 2.11: Illustration of how different signs of currents affect the voltage drop over the semi-conductor components.

Regardless if the current flows through the diode or the IGBT, the voltage drop always decreases the phase potential when the current is positive and increases it when the current is negative. The diode and IGBT have slightly different forward voltage drop characteristics, but the amount of time that the current flows through each component during one switching period is given by the duty cycle. The semi-conductor voltage drop in one half-bridge converter over one switching period can be formulated mathematically as

$$u_{drop} = \begin{cases} -d \cdot u_{igbt}(i) - (1-d) \cdot u_{diode}(i), & sgn(i) = +; \\ d \cdot u_{diode}(i) + (1-d) \cdot u_{igbt}(i), & sgn(i) = -; \end{cases}$$

where d is the duty cycle and u_{diode} and u_{igbt} can be found in the datasheet as functions of the current. The resulting phase potentials become

$$v_a = d_a \cdot U_{DC} + u_{a-drop} \quad (2.40)$$

$$v_b = d_b \cdot U_{DC} + u_{b-drop} \quad (2.41)$$

$$v_c = d_c \cdot U_{DC} + u_{c-drop} \quad (2.42)$$

To obtain the phase voltages in relationship to the neutral point of the wye connected machine, it is necessary to estimate the potential of the neutral point. The potential of the neutral point is calculated by

$$v_n = \frac{1}{3}\left(v_a + v_b + v_c\right) \tag{2.43}$$

The phase voltages are given by the phase potentials minus the potential of the neutral point of the wye connection

$$u_a = v_a - v_n \tag{2.44}$$
$$u_b = v_b - v_n \tag{2.45}$$
$$u_c = v_c - v_n \tag{2.46}$$

If voltage references from the current contoller are used for the identification they generally require compensation for the converter nonlinearities. There exist numerous strategies to compensate for the nonlinearities (mainly the dead-times) and there is still ongoing research on the subject [43, 44]. These papers generally propose methods that work online, and the compensation strategies are often used to facilitate accurate online parameter estimation [45]. However, there are also suggestions on methods that do the compensation straight forwardly offline with look-up table approaches [46]. This type of compensation strategy is used in this work, and a description of the method can be found in Appendix C.

Figure 2.12 shows comparisons between the measured voltage and the voltage reference with and without compensation during motor and generator operation. The compensation yields a significantly better match between the reference value and the measured voltage. However, the difference between the measurements and the reference without compensation is approximately the same in motor and generator operations, but with different signs. Since the calculation of the magnetic model uses measurements both from generator and motor operation, the difference tend to cancel out and the final results become approximately correct. Therefore, the converter nonlinearity compensation makes a small difference to the results of the magnetic model characterisation considering the derivation strategy of this work. Nevertheless, a compensation is recommended to assure good results.

Comments

This section describes methods to obtain the variables that derive the magnetic model and focuses on the approaches that have been used throughout this work. Of course, other

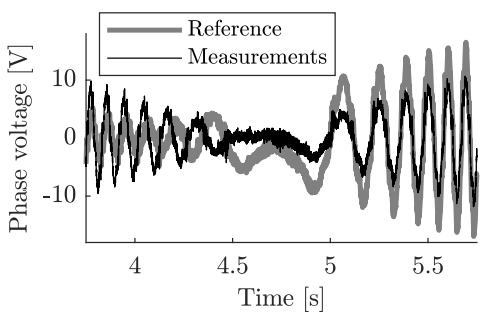

(a) Measurement vs. reference without non-linearity compensation.

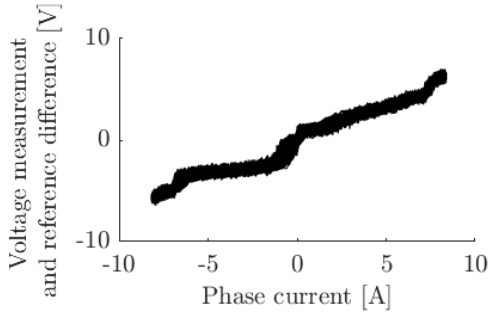

(b) Difference between the measured voltage and the reference without compensation.

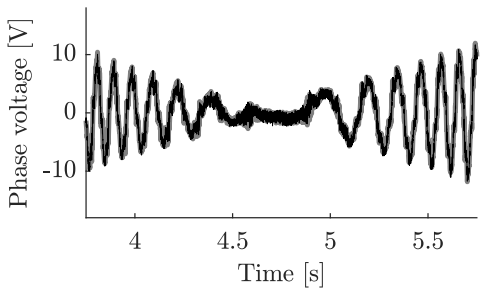

(c) Measurement vs. reference with non-linearity compensation.

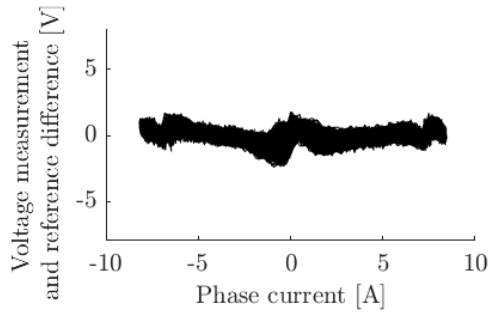

(d) Difference between the measured voltage and the reference with compensation.

Figure 2.12: Phase voltage measurements and controller references, and the difference between them.

methods can be considered as well. The position can be obtained by an externally mounted enconder instead of a resolver (if there is not an encoder already installed on the machine). The encoder significantly simplifies the demodulation and gives possibilities to increase the resolution of the position measurements in a straight forward manner. Furthermore, it is also possible to evaluate the possibility of obtaining the magnetic model with a sensorless approach. Nevertheless, most traction machines feature a position sensor, and this work does therefore not evaluate whether this is possible with a good result or not.

2.3.3 Post-processing

Once the voltage and the position measurements are obtained, the linked magnetic fluxes, and consequently also the magnetic model, can be derived by (2.10) and (2.11). However,

the measured data require processing to give good results. Since the induced voltage of a machine can be highly nonsinusoidal, especially with high field-weakening currents, the dq representations of the voltages tend to be very noisy. Furthermore, the angular velocity is derived from the derivative of the position which makes it very sensitive to position sensor noise. Another thing worth pointing out is that (2.10) and (2.11) have the angular velocity in the denominator. Consequently, the calculations become unstable when the rotational speed approaches zero. Therefore, samples at low speeds should not be used in the magnetic flux estimations; the lower fourth of the measurements are suitable to be left out of the post-processing calculations. The following sections present and discuss the data post-processing strategies that are used in this work.

Position

Since the position measurements yield the electrical angular velocity through derivation, noise in the data affect the results of the magnetic model estimation significantly. Furthermore, due to the uneven reluctance in the stator core there are fluctuations in the rotation of the rotor. As only the fundamental component of the angular velocity contains the useful information for the magnetic model derivation, these fluctuations should not be taken into consideration when deriving the magnetic model. Therefore, the position measurements need to be filtered before proceeding with the angular velocity derivation.

The data can be filtered in many ways, but it is very important that the filtered signal follows the measured position locally, and that it does not introduce a time delay. Considering this, a spline fit approach suits the demands of the filtering well. The spline fit algorithm divides the vector of data in a specified number of segments. Polynominal functions of chosen orders are fitted to the data in each segment by means of least-square minimisation, with the constraint that the derivative in each break point is the same for both intersecting functions. In addition, other constraints, such as making the functions more robust to outliers in the data, can be introduced as well. Since this thesis does not focus on data processing, the premade excellent Matlab function "splinefit" by Jonas Lundgren was used for the data filtering throughout the project [47].

Figure 2.13a and Figure 2.13b show the obtained position signal, and the position when is unwrapped, which means the discontinuous jumps between -180^o and 180^o are removed. Since the magnitude of acceleration is lower during the acceleration than the retardation phase of the test sequence, the machine turns more revolutions when it accelerates. This is seen explicitly when the position signal is unwrapped (Figure 2.13b): The position grows bigger than the starting point in the end of the sequence. The unwrapping of the position facilitates the filtering considerably since it makes it change continuously throughout the sequence. Figure 2.13c and Figure 2.13d show a local comparison between the measurements and fitted position, and the position residuals, respectively. The residuals are calculated by

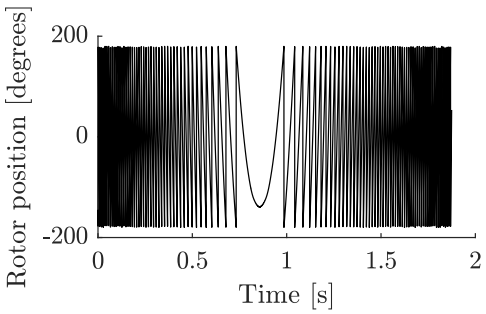

(a) Position measurements expressed in a ±180 degree frame.

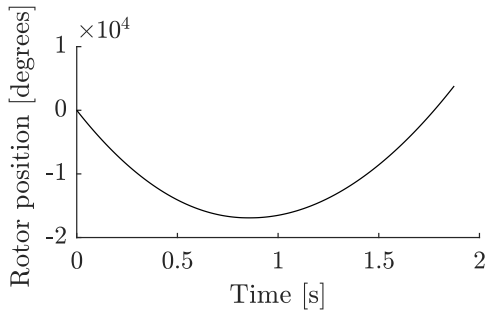

(b) Position measurements expressed as a continuous quantity.

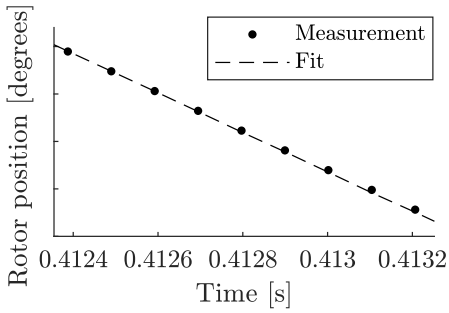

(c) Position measurements and model zoomed in.

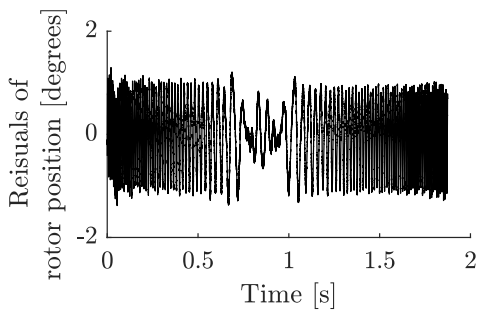

(d) Position measurements vs. model residuals.

Figure 2.13: Position measurements and filtering.

$$\Delta\theta = \theta_{meas} - \theta_{fit} \tag{2.47}$$

The graphical residual analysis is a good tool to spot if the filtering behaves well throughout the whole sequence. As Figure 2.13d shows, the quasi-instantaneous mean value of the residuals does not deviate significantly from zero through out the test, and the spline fit consequently works well. The mean residual value is in this case 0.02 degrees which is a satisfyingly low value.

Voltage

As stated above, only the fundamental frequencies of the voltages give useful information for the magnetic model estimation. Nevertheless, due to the converter switching and spatial preconditions, the phase voltages always contain significant harmonics that must be filtered away. Firstly, the switching harmonics that the pulse-width modulation gives rise to should

be removed. However, with the voltage measurement technique that this thesis discusses (section 2.3.2) the voltage is integrated over one switching period online, and the switching harmonics therefore disappear automatically. In addition to the PWM noise, the voltage also contains spatial harmonics due to the geometry of the machine. These harmonics also exist in the reference signal since the controller tries to follow the induced voltage as much as possible (to keep the currents as sinusoidal as possible). A preferable approach to filter away the spatial harmonics of the data is to first transform the voltages to dq quantities without any filtering. By doing so, the odd harmonics are transferred to the dq voltages (but with one order down[4]). However, the fundamentals of the dq voltages change approximately linearly with the angular velocity which makes the filtering much more straight forward compared to oscillating voltages.

The filtering can be conducted in different ways: One alternative is to assume that the voltages have a completely linear relationship with the speed. With such an assumption the dq voltages can be described by linear functions as

$$u_d^{\omega<0} = k_1 + k_2\omega \tag{2.48}$$
$$u_d^{\omega>0} = k_3 + k_4\omega \tag{2.49}$$
$$u_q^{\omega<0} = k_5 + k_6\omega \tag{2.50}$$
$$u_q^{\omega>0} = k_7 + k_8\omega \tag{2.51}$$

These functions can then be used to calculate the linked magnetic fluxes according to (2.10) and (2.11). Number II in the list of publications present results that are derived in this manner. The assumption that the speed and the voltages have a completely linear relationship is however not true due to phenomena such as iron losses. Therefore, another attractive alternative is to use a spline algorithm to approximate the quasi-instantaneous voltage over the whole measurement interval, similar to the strategy that the preceding section presents for the rotor position. Figure 2.14 shows measured voltages in the dq coordinates together with spline fits and the resulting residuals. As seen, the harmonic contents of the voltages are significant. In particular, there is a very prominent sixth harmonic in the dq reference frame that likely arises due to winding configurations, saturation phenomena and the spatial asymmetry in the stator due to the teeth and the slot openings.

[4]This statement is correct if harmonics with a negative phase sequence are considered "negative": A fifth harmonic with a negative phase sequence (i.e. a "minus" fifth harmonic) becomes a sixth harmonic with a negative phase after the transformation (i.e. a "minus" sixth harmonic).

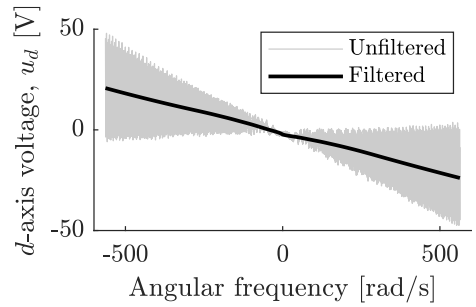

(a) Unfiltered and filtered d-axis voltage measurements.

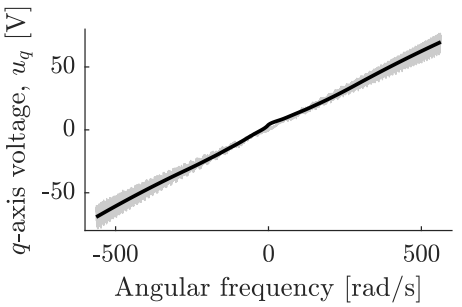

(b) Unfiltered and filtered q-axis voltage measurements.

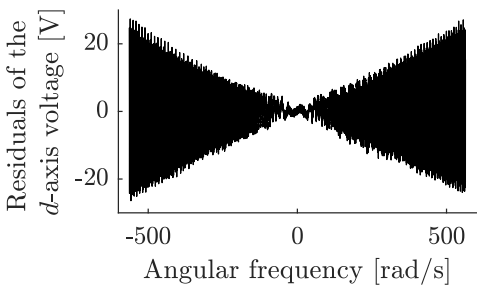

(c) Residuals of the d-axis voltage.

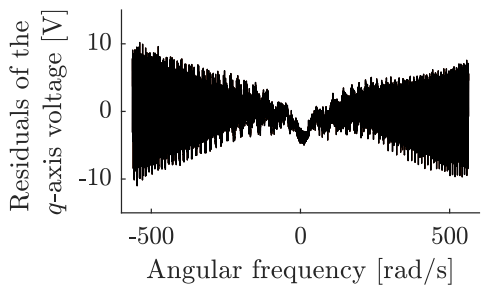

(d) Residuals of the q-axis voltage.

Figure 2.14: The voltage reference, measurement and the difference between them for u_{an}.

Comments

This section presents alternatives to process and filter the position and voltage measurement data from a dynamic test sequence. The presented approaches make use of a spline algorithm that creates polynomial functions for local segmented pieces of the data. However, the spline algorithm does have some drawbacks: The fitting can add additional noise such as oscillations in the filtered data, which is mainly due to that the derivative of two intersecting polynomial functions must be the same. However, this does generally not cause a problem since 1) the derivation uses data over the whole test sequence and 2) the additional noise is usually insignificant compared to the useful information. Nevertheless, it is recommend to graphically investigate the filtered position and voltage to make sure that the eventual oscillations are not significant.

Another point worth mentioning is that a decrease of the controller gains can be favourable. The decrease results in more sinusoidal voltages, but also in more harmonics in the currents, which, out of a operational point of view, can be unfavourable since the iron losses

increase. However, the iron losses do not affect the outcome of the magnetic model derivation significantly, and the gains can consequently be adjusted specifically for the testing procedure to avoid strong harmonics in the voltage.

2.4 Experimental tests

To try out the proposed magnetic model identification method the author, together with colleagues, prepared a test rig for a thorough evaluation. Appendix A and C present detailed information about the test object and the control and data acquisition hardware and software of the tests. The following section describes the proposed and implemented setup of the tests, the procedure of the testing and the final results from the experiments.

2.4.1 Setup

The dynamic sequence for the magnetic model derivation sets the basic requirements of the test setup: The test object is mounted on a firm foundation, and the shaft of the machine features a small flywheel to slow down the mechanical dynamics throughout the tests. To be able to achieve different and approximately uniform temperatures of the test object, an insulating material wraps the machine completely. As the following section explains, it is necessary to measure the temperature of the rotor at times during the testing. This is made possible by a PT100 sensor mounted close to the permanent magnets in the machine. However, the associated cables of the sensor rotate together with the rotor, and it is therefore not obvious how to reach them without affecting the setup. To achieve this, a small tube is mounted on the rotor of the machine. During the tests, the associated cables of the permanent magnet thermal sensor rotate inside the tube. When the machine stands still, one can reach the cables to measure the temperature of the rotor. A point worth mentioning is that the tests also require temperature sensors in the windings of the test object to control the temperature rise during the testing (the test objects of this work have such sensors installed). Furthermore, the sensor of the winding together and the sensor of the rotor can show if the temperature is approximately uniform in the machine. Figure 2.15 shows the test object of this work when when it is installed according to the proposed setup.

2.4.2 Test procedure

The test procedure starts with heating the stator windings electrically by accelerating and braking the machine with sufficiently high currents. When the windings have reached a certain temperature, a speed controller brakes the machine to standstill, whereupon the temperature sensor of the permanent magnet is connected to a measuring device. When

Figure 2.15: Test object isolated for tests.

the rotor and the winding have approximately the same temperature, the algorithm performs a complete dynamic test cycle, as described by Figure 2.7. The temperatures in the windings are monitored all the time during the whole test. Since the majority of the losses are copper losses (due to a relatively low speed limit in the test sequence), and since the thermal time constant between the windings and the permanent magnets is very high, the winding temperature is allowed to increase 5^oC throughout the whole test procedure – this is considered a low enough increase to leave the permanent magnet temperature almost unaffected within the time frame of a test. When all current combinations have been tested for the specific temperature, the windings are once again heated electrically until they reach a new chosen temperature, whereupon the testing restarts. It should be said that, since it takes a while for the machine to reach quasi-uniform temperature, these tests demand a lot of time. However, as many of the previous sections mention, the testing goes very fast when the magnetic model parameters are determined for one temperature.

2.4.3 Results

Figure 2.16 shows the estimation results of the linked magnetic fluxes and the inductances with a machine temperature of 30^oC. Both the apparent and the differential inductances are shown. However, the differential cross-coupling inductances ($L_{dq\,\text{differential}}^{\left(i_d^s, i_q^s\right)}$ from (2.17) and $L_{qd\,\text{differential}}^{\left(i_d^s, i_q^s\right)}$ from (2.18)) are left out since they become significantly lower than the self-inductances ($L_{dd\,\text{differential}}^{\left(i_d^s, i_q^s\right)}$ from (2.15) and $L_{qq\,\text{differential}}^{\left(i_d^s, i_q^s\right)}$ from (2.16)). The magnetic flux results are shown with contour plots (Figure 2.16a) that give a quantitative representation of the results, and surface plots (Figure 2.16b) that present them in a more qualitative way. The inductances are shown with surface plots (Figure 2.16c). As expected the results show a significantly higher q- compared to d-axis inductance since the interior permanent magnets, which have a relative permeability of approximately one, are aligned with the d axis. In an ideal machine the dq-axes inductances are constant and the magnetic flux consequently

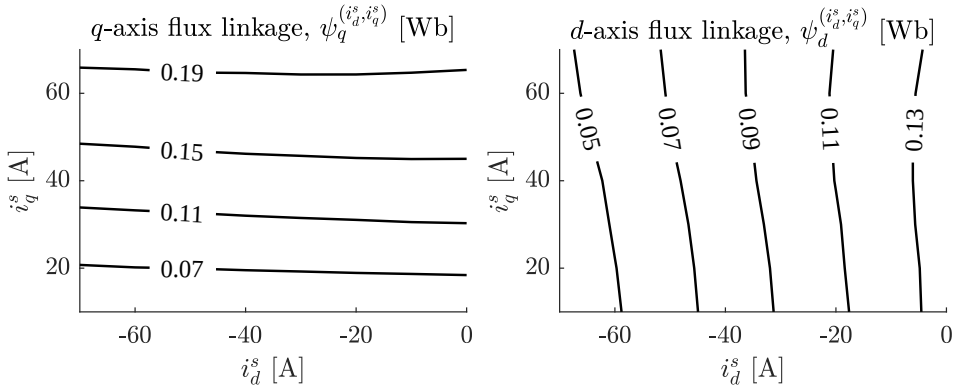

(a) Contour plots of the linked magnetic fluxes.

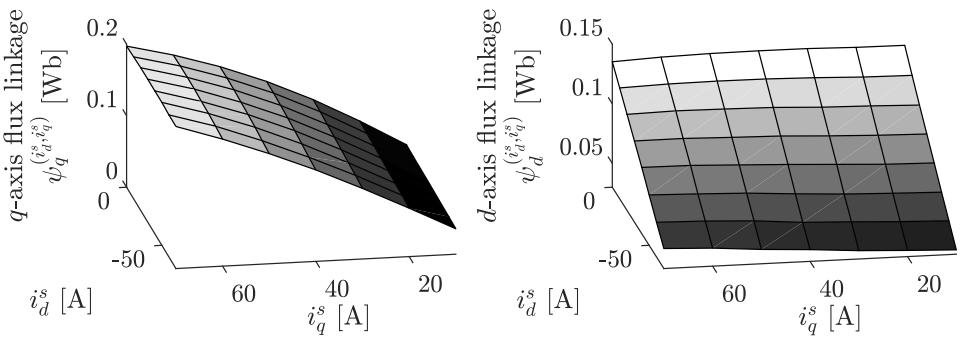

(b) Surface plots of the linked magnetic fluxes.

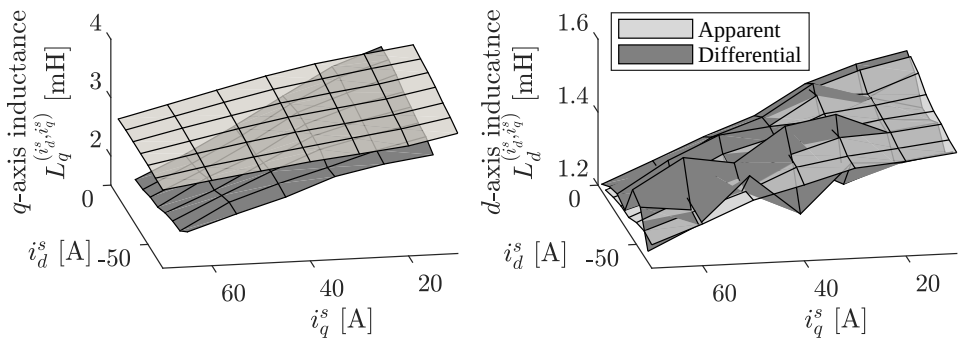

(c) Surface plots of the inductances.

Figure 2.16: Plots of the linked magnetic flux and inductance as a function of the dq currents with a machine temperature of 30^{o}C.

increases linearly with the current. Furthermore, there should be no cross-coupling, and the q-axis current should therefore not affect the linked magnetic flux in the d axis, and vice versa. However, due to saturation and flux leakage effects this is not the case. The q-axis inductance drops significantly when the q-axis current increases since the iron saturates. The drop can also be observed in the d-axis inductance due to cross-saturation of the magnetic flux, even though the effect is significantly lesser.

Comparison to steady-state measurements

To confirm the validity of the results from the dynamic method, additional tests were performed with a conventional constant-speed approach similar to the one presented in [27]. The constant-speed test procedure starts by connecting the test object to a similar machine by the rotor shaft. The additional machine keeps the rotational speed approximately constant regardless of which torque the test object produces. The resistance of one of the test object's windings is measured before the tests to assure that the temperature is 30^{o}C, whereupon different current combinations are evaluated at a constant speed (500 rpm). In between each current combination, the machine is allowed to rest so that the winding temperature decreases to its initial value. This assures a constant resistance value in the beginning of each current combination test. However, since the dynamo of the test setup is not strong enough to handle high torque transients, the controller of the test object must ramp up the currents to their reference. Therefore, the winding temperature might rise enough to affect the results noticeably; this is an important drawback of the constant-speed estimation approach. After the measurements, the linked magnetic fluxes are derived by (2.8) and (2.9) using the initial winding resistance value. Figure 2.17 shows the results of the comparison.

The estimated linked magnetic fluxes from the two methods fit remarkably well except in deep field-weakening region where the constant-speed tests show a slightly higher flux linkage in the d axis compared to the dynamic method. The reason for the difference is difficult to deduce, but a part of it can relate to an eventual underestimation of the stator resistance that would yield an overestimation of the flux. This is more likely to occur in high field-weakening operation points since it take longer time for the q-axis current to reach its reference (the torque increases faster with the q-axis current, which means the ramping of the current needs to be slower to guarantee the stability between the test object and the dynamo). Furthermore, the absolute value of the current is higher, which yields a faster increase of the temperature and consequently also the resistance of the winding. This explanation holds for the 0.07 [Wb] line in Figure 2.17 since the difference increase also for the q current, which relates to the linked magnetic flux estimation in d. However, for the 0.05 [Wb] line, the explanation is not sufficient since the offset between the dynamic and the constant-speed method is approximately constant regardless of the q-axis current. Nev-

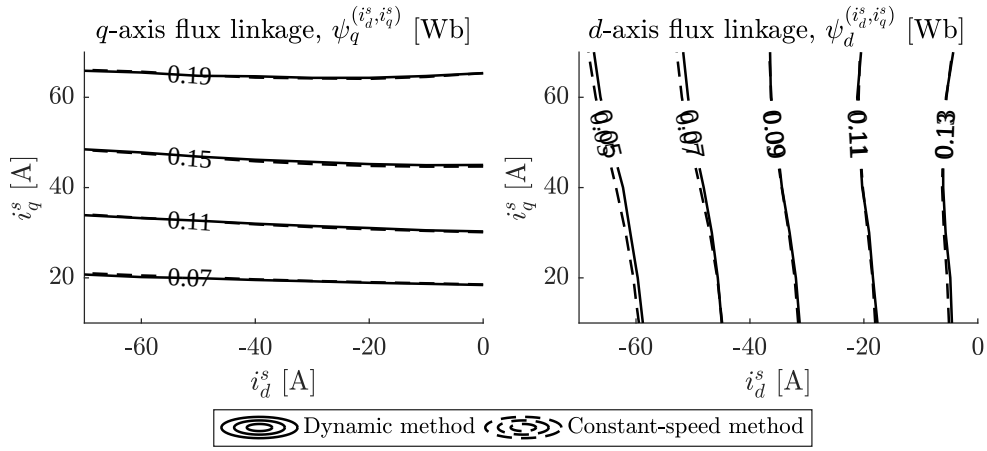

Figure 2.17: Comparison between the dynamic method and the constant-speed method results.

ertheless, the difference is still small enough to be regarded as negligible out of a validation point of view.

Influence of temperature

Figure 2.18 shows the results from the magnetic model derivation with machine temperatures of 30^oC, 60^oC and 90^oC. The linked magnetic flux in the d axis drops significantly with the temperature while the q-axis flux remains fairly constant except in high saturation where the flux increases with temperature. The drop in the d-axis flux is mostly due to the temperature's influence on the magnetic characteristics of the permanent magnets: The temperature also changes the electromagnetic properties of the electric steel of the core of the machine slightly, but this influence is low compared to the change of the remanent flux and the magnetic coercivity of the permanent magnets. The temperature's influence on the magnetic model is discussed further in Appendix B that presents the FEM model of the machine. When the d-axis flux decreases the saturation of the iron due to cross-coupling effects between the q- and d-axis flux decreases, and the iron in the q axis path consequently saturates less with the q-axis current.

Figure 2.18b shows a comparison between the results from the measurements and finite-element method (FEM) simulation results. Appendix B presents the FEM model together with a discussion about the sensitivity of the simulation results and an explanation to how the temperature dependence is included in the model. The results fit well considering that manufacturing tolerances in the machine make it difficult to achieve a perfect fit. The

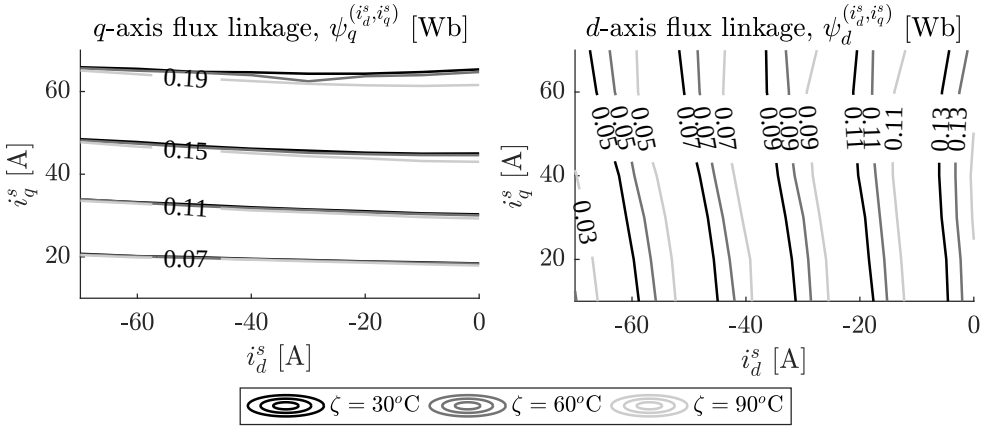

(a) Linked magnetic flux for the machine temperatures 30^{o}C, 60^{o}C and 90^{o}C.

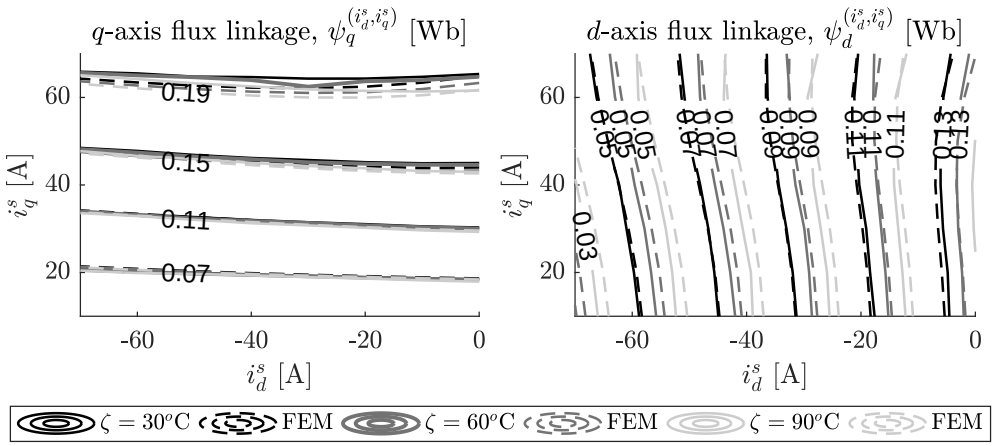

(b) Linked magnetic flux for different temperatures: measurements vs. FEM simulations.

Figure 2.18: Measurements and simulations of the linked magnetic flux for 30^{o}C, 60^{o}C and 90^{o}C.

only thing that changes in the FEM model with a temperature variation is the estimated magnetic coercivity characteristics of the permanent magnets. The results indicate that the change in the magnetic characteristics of the permanent magnets is the dominating factor for why the magnetic model of the machine varies with temperature.

Comparison between using voltage measurements and reference signal

This section presents a comparison between the results when the estimated voltage and the voltage reference from the current controller derive the magnetic model (the current controller and the generation of the voltage references are described in Appendix C). This is an important comparison for validation of the possibility to obtain an accurate estimation of the magnetic model without any voltage measurement equipment. The choice of current controller affects the results since they depend on how well the current controller's reference match the actual inverter voltages. Therefore, the conclusions drawn here are only valid for the specific current controller that was used throughout this work. Nevertheless, the results still indicate if it is possible to use voltage references instead of measurements or not. Figure 2.19 shows a comparison between the magnetic model estimation from the reference and measurements.

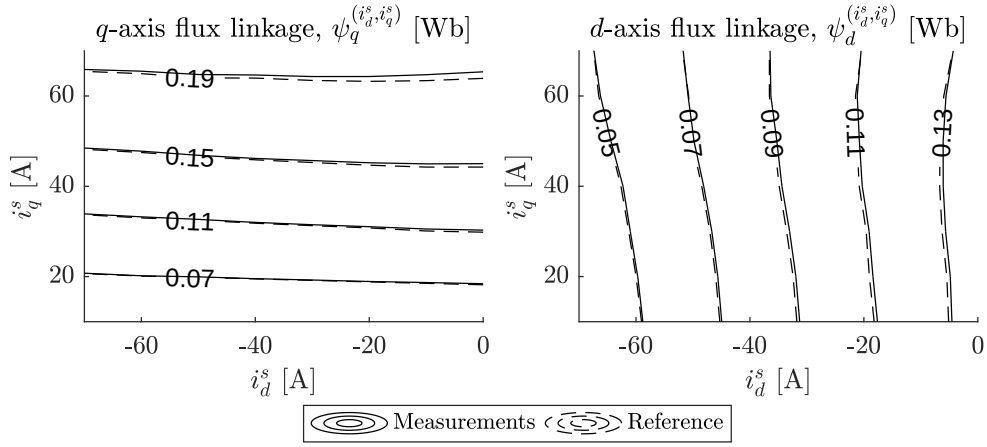

Figure 2.19: Linked magnetic flux, voltage measurement vs. reference.

The results are almost completely consistent and the voltage reference can therefore be used for the magnetic model parametrisation in in-situ implementations of the method.

2.5 Summary

The main purpose of this chapter is to show how the relationship between the currents and the linked magnetic fluxes in IPMSMs can be estimated with voltage and rotor-position measurements from when the machine operates under mechanical transient conditions. The chapter proves that the relationship can be obtained relatively easily, and with very

good results, if measurements from both motor and generator operation are used in the estimation. The following sections present possible applications of the method and conclude the chapter.

2.5.1 Possible applications

The magnetic model estimation method of this work can be analysed from two perspectives: On one hand, the method is capable of performing rapid characterisation of the magnetic model of a machine. On the other hand, the shaft does not need to be connected mechanically to any dynamo or load during the characterisation. The first perspective shows that the method suits end-of-line testing well. The test sequence can be designed to take no more than a minute to perform. Furthermore, in an automated process, tests can be set up quickly, even if a flywheel must be mounted on the shaft. With such tests, each manufactured machine can have an individual magnetic model map that could be used for e.g. optimal control algorithm designs. Furthermore, such tests also make it straight forward to control the health of e.g. the permanent magnets in the machines.

The second view point implies that 1) the dynamic method is a good alternative to evaluate prototype machines in different environments under different conditions (e.g. uniform temperature in the machine) and 2) that it makes it possible to evaluate already installed machines, supposing that the drive shaft can be disconnected from the load. As this chapter shows, the magnetic model can be derived with the temperature as a variable. Such models can be used to investigate if the permanent magnet flux decreases as expected with temperature. Furthermore, it is possible to use the models as look-up tables to track the change of the temperature of the permanent magnets online in a straight forward fashion. As mentioned above, post-installation testing requires that the shaft can rotate freely. Unfortunately, in many traction applications the machine cannot be disconnected from the wheels. However, in a workshop the vehicle can be lifted to release the wheels from the ground. In such situations, it is straight forward to perform the test, even if they might take relatively long time to perform due to the moment of inertia and the losses of the drivetrain.

Conclusions

This chapter presents a dynamic test approach that derive the electromagnetic characteristics of PMSMs, and shows how the method can be extended to include the temperature as a variable. The benefits of the approach include rapid testing times, relatively little necessary equipment and an insignificant increase of the machine temperature during the tests. Since the evaluated machine stands alone during the evaluation, it is straight forward to wrap it in insulating materials. This makes it possible to achieve an approximately uniform temperature distribution in the machine after electrical heating. As a consequence,

the magnetic model can be derived for arbitrary temperatures independent of the ambient temperature. Validation of the results show that the method performs well, and it can be considered mature enough to be of interest for the industry.

Chapter 3

Loss Analysis

3.1 Introduction

Estimation and modelling of power losses are fundamental parts of the overall performance evaluation and characterisation of electrical machines. However, the mechanisms and distribution of the losses in a machine are very complex, and to derive an accurate picture of where the losses arise is a difficult undertaking. When the magnetisation of the machine can be turned off, the indirect method yields a division between the mechanical losses, the iron losses during open circuit operation and the copper losses [48, 49]. However, when the magnetisation cannot be turned off a separation of speed-dependent losses into different componenets becomes rather limited and difficult[1]. Furthermore, the magnetic flux density distribution in the core of the machine contains a lot of harmonics when the machine works in field-weakening operation and saturation, and to find coherent analytical models over the whole operating range of a highly dynamic drive is therefore nearly impossible.

With this being said, it is still important to find approximate estimations and models of how the losses behave under different operation conditions. In recent years, many proposals have been presented on how to evaluate and model highly dynamic permanently magnetised machines over a wide operating range; [53] gives a review of many different types of power loss estimation and modelling methods, but the literature also presents numerous other approaches. Generally, the power loss models are based on results from conventional input-output tests (with a dynamo, a power analyser, and a torque sensor [48, 49]) or simulations, and there is relatively little research being published on alternative test approaches especially

[1] It is possible to perform tests with the indirect method if the magnetised rotor of the machine is replaced with one without permanent magnets in the first stage of the testing. This is however a quite demanding and difficult procedure since the non-magnetised rotor must replicate the initial rotor in terms of mass and bearing losses very well. Nevertheless, the litterature shows that these types of tests can yield accurate results [50–52].

dedicated to electrical machines. This chapter presents ways to derive the loss profiles of IPMSMs with measurements from from dynamic measurements, i.e. with the machine accelerating and braking rather than running at constant speed. The main goal is to provide a toolbox to analyse loss results from dynamic measurements and to show how the results can be used for modelling. The list below gives a brief introduction to the different sections of the chapter

3.2 **Conventional machine testing** gives a brief description of established test methods;

3.3 **Loss calculation** describes different approaches to calculate the losses from measurements;

3.4 **Models of losses** presents established models of loss phenomena in different parts of a machine, and describes the modelling approach of this thesis;

3.5 **Dynamic tests for loss estimation** explains the dynamic test approach for loss estimation and discusses aspects that are important;

3.6 **Experimental tests** gives a walkthrough of the preconditions and limitations of the testing, and shows results of the measurements, together with modelling results and validation;

3.7 **Summary** discusses the advantages and disadvantages of the method. Furthermore, suggestions to extensions of validation and possible additions to the test equipment are presented.

3.2 Conventional machine testing

Traditional machine test methods evaluate machines in both electrical and mechanical steady-state operation. Four reasons to this are:

1. During steady state operation it is enough to evaluate just a few periods of the fundamental frequency in order to obtain accurate results, and the amount of necessary data can therefore be held within reasonable limits, even though the sampling frequencies and the resolutions of the measurement system's A/D converters are high.
2. Many industrial machines operate with constant and well-defined torques and speeds. Therefore, it makes sense to evaluate these specific working points very carefully.
3. It is relatively easy to estimate the uncertainties of the results, which are essential for e.g. benchmarking.

4. The majority of the test methods that the standards propose work under these conditions.

The conventional setups generally include a dynamo that counteracts the torque from the test object, a torque sensor, power electronic drives for the test object and the dynamo, and a control and data acquisition system, which includes sensors, data communication systems, gate signal controls, and so forth. Figure 3.1 shows an example of a setup for conventional tests [48].

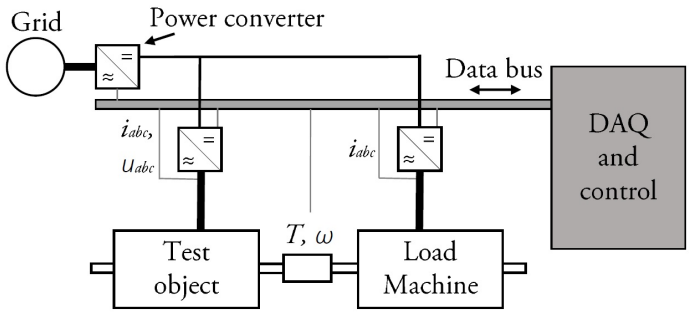

Figure 3.1: Typical test setup for classic (converter driven) input-output and indirect efficiency testing.

Tests with the setup in Figure 3.1 give information about e.g. the magnetic characteristics, the torque performance and the losses of the machine. The litterature generally proposes two methods to derive the losses of electrical machines: the input-output (or direct) method or the indirect method [48–52]: The input-output method measures electrical (or mechanical) input power and the mechanical (or electrical) output power and calculates the difference. This method derives the losses in a straight forward fashion but it does not give any explicit insight into the origin of the power losses or how they are distributed in the machine. The second approach, the indirect method, aims to find individual loss components and add them up. This is a well established method for machines where the magnetisation can be turned off. The tests typically include no-load tests (with and without a magnetised rotor if it is possible to turn it off). However, in the case of a radial-flux inner-rotor PMSM the rotor needs to be replaced with one that does not include permanent magnets when deriving the mechanical losses.

Figure 3.2 presents another type of setup that is used for efficiency and loss measurements of electrical machines: the calorimetric method (the drive system, the cabling and the DAQ/control system are left out of the figure for clarity). The calorimetric test measures the heat produced by the losses when the machine works under defined operating conditions. The machine is placed in a thermally insulated compartment (a calorimeter), and a fluid is inserter into and abstracted from the calorimeter with a controlled flow rate. Once the

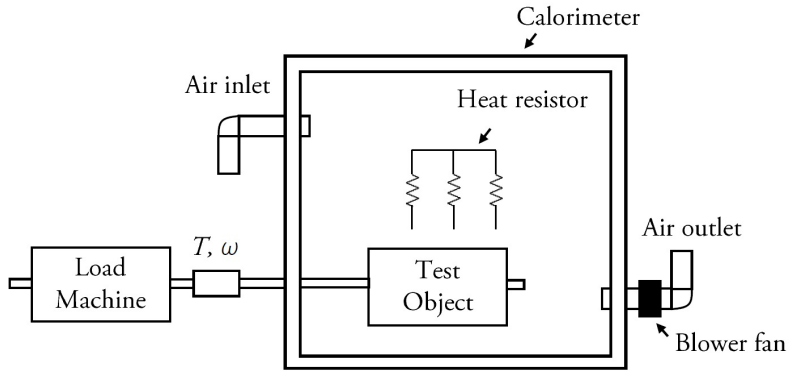

Figure 3.2: Typical test setup for calorimetric measurements.

temperature has reached steady state inside the calorimeter, a calculation of the difference between the inlet fluid temperature and the outlet fluid temperature yields the heat that the losses in the machine give rise to (the example in Figure 3.2 uses air as machine cooler, but it is also possible to use a liquid through a heat exchanger) [54]. The losses can be derived if the specific heat and density of the coolant is known and approximated to be the same at the inlet and outlet through

$$P_{loss} = C_p \dot{V} \rho_c \Delta\zeta \tag{3.1}$$

where C_p is the specific heat, $\dot{V}$ is the volumetric flow rate, ρ_c is the coolant density and $\Delta\zeta$ is temperature difference between the fluid inlet and the fluid outlet of the calorimeter.

Another variant of the calorimetric test replicates the temperature difference that the machine losses give rise to with a heating resistance, where the ohmic losses can be calculated accurately. Firstly, the machine is placed inside the calorimeter where it operates until the outlet fluid temperature reaches steady-state. Secondly, the machine stops to operate, and a resistance in the calorimeter is excited with a sufficient current so that the outlet fluid reaches the same steady-state temperature as for when the machine operated. Since the resistance and the current of the heater can be measured relatively easily and accurately, the power loss of the machine can be estimated. This method does not require knowledge of the specific heat and the density of the coolant, and it removes the uncertainty that the approximation that the properties of the coolant are the same in the inlet and the outlet gives rise to. However, the heater should preferably be placed in a fashion that replicates the placement and spatial features of the machine as much as possible. Ideally, the heater should be distributed on top of the machine [55]. The calorimetric method significantly decreases the uncertainty of the loss/efficiency measurements compared to the input-output method [7]. The main drawbacks of the calorimetric tests are the time for the installation

of the machine, and the long execution time of the tests. The inside of the calorimeter including the test object needs to reach thermal equilibrium before the tests. This can take several hours. If the machine operates over a wide speed and torque range as a traction machine does, the setup must be in thermal equilibrium for each operation point (each combination of torque and speed). This leads to extremely long testing times if the whole operation range of the machines should be evaluated.

3.3 Power loss calculation

The most straight forward approach that estimates the power losses in electrical machines calculates the difference between the electrical and the mechanical power. The instantaneous voltages and currents in the stator windings give the electrical power while the mechanical torque and the mechanical angular velocity give the mechanical power according to:

$$P_e = u_a i_a + u_b i_b + u_c i_c \tag{3.2}$$
$$P_m = T_m \omega_m \tag{3.3}$$

where $u_{a,b,c}$ are the phase voltages, $i_{a,b,c}$ the phase currents, T_m and w_m the mechanical torque and angular velocity, respectively, and P_e and P_m are the electrical and mechanical power. Normally, the conventional test approaches evaluate the machines when they rotate with constant speed (as described in the previous section). A sensor installed on the shaft in between the test object and the load machine measures the torque and the speed, and consequently also the mechanical power according to the expression above. However, when the machines operate during unloaded and dynamic conditions, the acceleration and the moment of inertia of the rotating mass yield T_m, and consequently also the mechanical power as

$$T_m = J\frac{d\omega_m}{dt} \rightarrow P_m = J\frac{d\omega_m}{dt}\omega_m \tag{3.4}$$

where J is the moment of inertia. Therefore, it is theoretically straight forward to estimate the losses of a machine during unloaded and dynamic operation if the moment of inertia is known, and the shaft speed, the currents, and the voltages are measured. Unfortunately it is challenging to measure all of the needed parameters accurately and to process and synchronise the measured data after the acquisition. Furthermore, estimations of the uncertainty of the measured data is complicated. Due to these reasons, little research looks into dynamic test methods for loss estimation. Nevertheless, this work does not focus on

accuracy but aims to give an approximate assessment of the losses, where the results can be used for thermal modelling and prediction of heat dissipation. With this focus, the dynamic approach provides an interesting alternative to the conventional test methods.

If the machine is controlled to maintain the same dq-axes currents in both motor and generator operation, the losses are approximately the same if the magnitude of the angular velocity is the same (the motor and generator operations are achieved by rotating the rotor in different directions). The copper losses do not change and the flux characteristics remain alike. As a consequence, the average of the loss estimations from the motor and the generator operation gives a good approximation of the losses. The averaging makes the calculations more robust to miscalculations of the powers. For example, if the calculations overestimate the mechanical power, which can be happen if the estimated moment of inertia value is too high, the loss calculations become too high in generator operation but too low in motor operation, and the averaging results in an approximately correct loss estimation. The losses are formulated mathematically as

$$\hat{P}_{loss,mg} = \frac{|P_e - P_m|^{\text{motor}} + |P_e - P_m|^{\text{generator}}}{2} \tag{3.5}$$

where the subscript $loss, mg$ stands for loss calculation with measurements from motor and generator operation.

Another approach, which estimates the speed-dependent losses of the machine, analyses the difference between the electromagnetic and the mechanical torque. As described in the previous chapter the electromagnetic torque is given by (2.19). Substituting the fluxes in (2.19) with the expressions form (2.8) and (2.9) the electromagnetic torque can be estimated with the measured voltages and currents, the electrical angular frequency and the stator resistance

$$\hat{T}_e = n_{pp} \left(\frac{u_q - R_s i_q^s}{\omega} i_q^s + \frac{R_s i_d^s - u_d}{\omega} i_d^s \right) \tag{3.6}$$

where n_{pp} is the number of pole pairs in the machine, u_d and u_q are the dq voltages, R_s the stator resistance, ω the electrical angular velocity and i_d^s and i_q^s are the dq-axes stator currents. The difference between the electromagnetic (3.6) and the mechanical torque (3.48) gives an estimation of the loss torque

$$\hat{T}_{loss} = |\hat{T}_e - T_m| \tag{3.7}$$

A multiplication between the estimated loss torque and the mechanical angular velocity yields an estimation of the speed-dependent power losses

$$\hat{P}_{loss,sd} = \hat{T}_{loss}\omega_m \tag{3.8}$$

As mentioned above, (3.8) only estimates the speed-dependent losses (hence the subscript $loss, sd$), and consequently excludes the speed-independent resistive losses in the stator windings. It should also be pointed out that since the estimation of $\hat{T}_e$ depends on the stator resistance, the temperature must be monitored throughout the tests due to its influence of the conductivity of the electrical conductors. Furthermore, the estimation assumes that the linked magnetic flux linkage is independent of the frequency, which is not true due to e.g. iron losses. Consequently, the estimation of $\hat{T}_e$ must be seen as quite an uncertain approximation. Regardless, $\hat{T}_{loss}$ makes it possible to graphically analyse the losses qualitatively in a way that $\hat{P}_{loss,mg}$ does not provide (at least not as explicitly as $\hat{T}_{loss}$). Furthermore, a comparison between $\hat{P}_{loss,sd}$ and $\hat{P}_{loss,mg}$ gives a good indication indication of whether the estimations are valid or not. Therefore, both loss estimation approaches help with analyses of the power loss characteristics of the machines.

To facilitate the notation of the modelling of the losses that section 3.4 presents, we assume that

$$P_{loss} \approx \hat{P}_{loss,mg} \tag{3.9}$$

and

$$T_{loss} \approx \hat{T}_{loss} \tag{3.10}$$

Consequently, the next coming section models P_{loss} and T_{loss} instead of $\hat{P}_{loss,mg}$ and $\hat{T}_{loss}$.

3.4 Power loss models

3.4.1 Established power loss models

If one is to analyse and model power losses in electrical machines it is important to understand where the losses occur and why. This section presents an overview of the main loss components in electrical machines and how they behave according to theory. In particular, the section focuses on the relationships between the power losses and the current and the frequency since these are the parameters that the models of this thesis are based upon.

Power losses in the iron core

Even though many papers present models that divide iron losses into separate parts that can be interpreted as different loss phenomena, more strict literature on applied physics conclude that all electromagnetic losses in ferromagnetic materials consist of energy dissipation due to eddy currents generated from magnetic domain wall movement [56]. Modelling of this loss phenomenon has attracted enormous amount of research (and still does). Nevertheless, this section only includes the aforementioned model approaches that separate the losses into different components; the separation approach is most relevant for this thesis since it shows explicitly how the losses approximately relate to the current and the frequency. In addition, the temperature's influence on the losses is also discussed due to its relevance in this context. However, it should be mentioned that the loss separation approach often is trumped by other loss models – like hysteresis models (e.g. the Preisach models, which should not to be confused with the hysteresis part of the loss seperation models), or empirical models based on the early work by Steinmetz – in terms of accuracy [57, 58].

The interaction between the eddy currents on a microscopic level is complicated to model, and since the energy dissipation (or energy loss per magnetisation cycle) starts already at seemingly zero frequency, it makes sense out of a model point of view to include a constant term when modelling the energy loss in ferromagnetic materials under magnetisation (this loss part is often called the static losses, or the work required for remagnetisation, in the literature). This transfers into power losses that are linearly dependent on the frequency. These losses also have a relationship to the peak of the magnetic flux density (B_p); a famous publication by Steinmetz concludes that the losses relates to $B_p^{1.6}$ while later publications, e.g. by Pry and Bean, prefer B_p^2 [59, 60]. The static energy loss is generally called hysteresis loss in terms of power and is included in the majority of all iron loss models that work with loss separation in the frequency domain. Mathematically, the hysteresis loss can be formulated as

$$P_h = k_h f B_p^{\alpha_h} \tag{3.11}$$

where k_h and α_h are material and geometry dependent constants and f is the frequency.

On a macroscopic level, the eddy current losses can be understood through Faraday's law of induction that relates the induced voltage to the derivative of the magnetic flux. Since the amplitude of the induced voltage relates linearly to the frequency and amplitude of the varying magnetic flux, the power losses due to the induced voltage that creates the eddy currents relate to the frequency and peak magnetic flux density squared (voltage squared divided by resistance yields the electrical power). This loss component is generally denoted the classical loss, or simply the eddy current loss and can, just like the hysteresis loss, be

found in most existing iron loss models. Mathematically, the classical loss is given by

$$P_c = k_c f^2 B_p^2 \tag{3.12}$$

where the constant k_c relates to the geometry and resistivity of the material.

For some applications, the simplified energy loss per magnetisation cycle model that only contains a static component and a dynamic component that relates linearly to the frequency is not sufficient. Considering that the eddy currents that the magnetic wall moment generates interact with each other on a microscopic scale, it stands to reason that the losses have a more complex relationship to frequency than the hysteresis and classical models present. Losses that do not fit into either the hysteresis or the classic model are generally grouped together and are called the anomalous or simply the excess losses. Studies by Bertotti [61] show, and explain why, these losses can be modelled as a function of the square root of the frequency in terms of energy per cycle. The excess power losses are formulated as

$$P_e = k_e f^{1.5} B_p^{1.5} \tag{3.13}$$

where k_e relates to the intricate magnetic and electrical properties of the material.

The temperature influences the conductivity of iron, and therefore also the iron losses. Since the conductivites of soft magnetic materials generally decrease when the temperature rises, the induced eddy currents, and hence the losses, decrease. The change of losses depends heavily on the rate of induction, where a higher B_p yields a greater difference in losses. Publications [62–64] show a slight linear decrease of losses in the temperature region of interest for silicon iron magnetic steels. However, the temperature has a much more significant impact on the losses in other soft magnetic materials [65]. Another point worth noticing is that if the temperature of the permanent magnets in the machine increases, the remanent flux density and the absolute value of the coercive field strength decrease as well. This leads to a lower peak magnetic flux density in the machine, which in turn results in lower losses (but also lower torque).

Power losses in the electrical conductors

This section treats the power losses in copper conductors in machine windings, but the same models that are presented here work for other winding materials as well. These losses can be divided up into a part that is due to the DC resistance of the winding, and an AC loss part that eddy currents give rise to. The electrical power loss density due to the DC resistance is formulated as

$$p_{DC} = \frac{(\jmath_{rms})^2}{\sigma_{\text{Cu}}} \tag{3.14}$$

where σ_{Cu} is the conductivity of copper, and $\jmath_{rms}$ is the root mean square value of the current density [66]. For a specific current in a well-defined circular winding, the power losses can be written as

$$P_{DC} = \frac{l}{r^2\pi}\frac{i_{rms}^2}{\sigma_{\text{Cu}}} = R_{DC} i_{rms}^2 \tag{3.15}$$

where l is the length, r is the radius of the conductor, i_{rms} is the root-mean-square current and R_{DC} is the DC resistance of the conductor. If the dq-axes currents are derived with a power invariant transform, (3.15) can be rewritten to

$$P_{DC} = R_{DC}\sqrt{i_d^{s2} + i_q^{s2}} \tag{3.16}$$

The eddy-current part of the copper losses is considerably more complicated to express and quantify accurately compared to the DC resistance part. The increased losses due to eddy currents can be divided into two major parts: The losses due to the skin effect and the proximity losses [67]. The skin effect arises due to the eddy currents inside the conductor in which the current flows. If the current in the conductor changes, eddy currents arise due to the induced magnetic field. These currents oppose the main current in the middle of the conductor, but enforce it in the outer periphery. Therefore, the net current remains, but the cross-sectional area of the conductor that conducts current decreases. As a consequence, the resistance of the winding increases, and therefore also the losses. The proximity losses arise from eddy currents that are induced by an external magnetising field. The field typically comes from parallel conductors in the windings or from the magnetising permanent magnets.

It is complicated to find accurate analytical expressions for the eddy-current losses due to their complex relationship with frequency. However, the components can be estimated separately and added together according to superposition [68]. Both components depend on the "skin depth" that, in circular conductors, is approximately given by

$$\delta = \sqrt{\frac{2}{\sigma_{\text{Cu}}\omega\mu_0\mu_{\text{Cu}}}} \tag{3.17}$$

where ω is the angular frequency of the current and μ_0 and μ_{Cu} is the magnetic permeability of free space and copper, respectively. The skin effect and proximity losses can be calculated

accurately with quite complicated equations that make use of the Bessel function of the first kind [69]. However, if the ratio between the radius r of a strand in the conductor and the skin depth is low, the additional power dissipation can be approximated by considerably simpler equations. Supposing $r/\delta < 2.2$, the additional resistance due to skin effect can be approximated by [70]

$$R_{skin} = R_{DC}\frac{1}{48}\left(\frac{r}{\delta}\right)^4 \tag{3.18}$$

Supposing the skin effect due to the external field is negligible, the proximity effect is approximately given by

$$P_{prox} = \frac{\pi l r^4 B_p^2 \omega^2 \sigma_{\text{Cu}}}{768} \tag{3.19}$$

where B_p is the peak value of the external magnetic flux density that passes the winding [71, 72]. These equations hold if the frequency and the radius of the conductor are relatively small; if not, the expressions overestimate the losses significantly. It should also be mentioned that the windings in low voltage, medium power electrical machines often are distributed quite randomly in the stator slots, which makes it challenging to foresee the external B field that crosses the individual conductors. Therefore, accurate estimations of the proximity losses generally demand time consuming simulations or measurements [73]. In addition, the aforementioned equations hold for circular strands, and e.g. rectangular conductors demand different equations.

Figure 3.3 shows calculations of the relative increase in resistance due to the skin effect, also called the skin-effect coefficient, which are derived by

$$k_{skin} = \frac{R_{skin} + R_{DC}}{R_{DC}} \tag{3.20}$$

Furthermore, the figure shows the proximity losses, calculated with (3.19), compared to more accurate calculations with equations from [69], over a large frequency spectra. A strand diameter of 2 mm, which is large for typical machines with a conventional winding scheme [74], is considered (the difference between the calculation approaches decreases significantly with a smaller diameter). Figure 3.3a shows the increase of resistance due to the skin effect, and Figure 3.3b shows the normalised proximity loss. Whether the approximation holds or not is dependent on the machine design, but for general state-of-the art machines designed for traction, the winding losses can be said to be dependent on the square of the fundamental frequency. It should be emphasised once again that this only

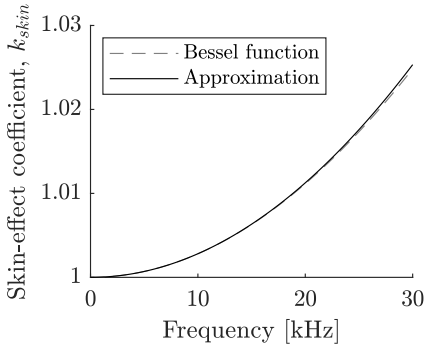

(a) Resistance change due to skin effect.

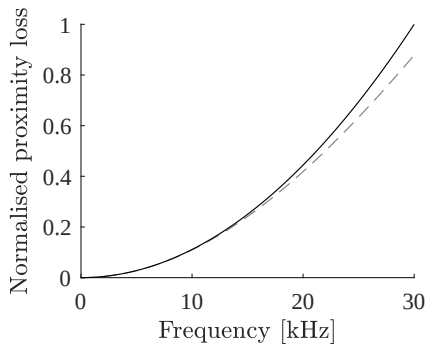

(b) Normalised proximity losses.

Figure 3.3: Comparison between accurate and simplified calculations of the skin effect and proximity losses.

holds for conventional circular windings. for different approaches such as non-circular hair pin windings a specific analysis should be made for each design.

Since the electrical conductivity of copper (and other conducting materials) depends on temperature, so do the resistive losses. The change of the electrical conductivity of copper with temperature is generally expressed as

$$\sigma_{\mathrm{Cu}} = \frac{\sigma_{\mathrm{Cu}0}}{[1 + \alpha_{\mathrm{Cu}} (\zeta - \zeta_0)]} \tag{3.21}$$

where α_{Cu} is the temperature coefficient of copper, which is approximately 0.004 1/K in the relevant temperature range [75], $\sigma_{\mathrm{Cu}0}$ is the electrical conductivity of copper at zero degrees Celcius, ζ is the temperature and ζ_0 is zero if the temperature is given in Celcius or 273 degrees if the temperature is given in Kelvin. This means the DC resistance, and hence the losses due to it, increase linearly with temperature. The eddy-current losses have a more complicated relationship with the temperature since the proximity effect in (3.19) decreases when the conductivity drops. Due to the complicated relationship, [76] suggests an empirical approach to find the relationship between the AC and DC losses in the windings. Whether this is necessary, or if (3.18) and (3.19) are sufficient to estimate the temperature dependence for round wires with a low r/δ ratio is out the scope for this work to investigate.

Power losses due to mechanical phenomena

The two major parts of mechanical losses in radial flux electrical machines with an inner rotor are friction losses in the bearings and windage losses in the airgap. The bearing manufacturer SKF provides generous information on how to estimate the friction torque in bearings [77]. Furthermore, an online tool for calculations of the bearing friction torque can be found in [78]. SKF suggests a division of the torque in four main components: rolling friction, sliding friction, friction due to the sealing of the bearing and oil drag friction. The bearings of test objects of this work are equipped with non-contact seals. Consequently, the rotating and stationary part of the bearings are not in contact with each other, and the losses in the seals are therefore negligible [79]. Furthermore, the bearings are lubricated with grease and the oil drag losses are therefore zero. The rolling friction torque is given by

$$T_{rr} = \Phi_{ish}\Phi_{rs}G_{rr}(\nu_g n)^{0.6} \tag{3.22}$$

where ν_g is the viscosity of the grease and n is the rotational speed. The factors Φ_{ish} and Φ_{rs} are the inlet shear heating reduction factor and the kinematic replenishment/starvation reduction factor, respectively. Both factors are geometry-dependent, empirical and decrease with the speed and the viscosity of the grease. The reduction factors have a significant impact on the friction torque at low bearing temperatures since the viscosity of the grease is high, but affect the torque less when the temperature increases. The parameter G_{rr} depends on the type, geometry, and the radial and axial load of the bearing.

The sliding friction torque is given by

$$T_{sl} = G_{sl}\mu_{sl} \tag{3.23}$$

where μ_{sl} is the sliding friction coefficient and G_{sl} is a parameter that depends on the bearing type, the geometry, and the radial and axial load. The sliding friction coefficient depends on the lubrication and is given by

$$\mu_{sl} = (\Phi_{bl}\mu_{bl} + (1 - \Phi_{bl})\mu_{EHL}) \tag{3.24}$$

where Φ_{bl} is the weighting factor for the sliding coefficient, μ_{bl} is 0.15 when the machines stands still and 0.12 when it rotates, and μ_{EHL} is the sliding coefficient in full-film conditions which is significantly lower than μ_{bl}. The factor Φ_{bl} decreases with the speed and the viscosity of the grease. Consequently, μ_{sl}, and therefore also the sliding friction torque, is higher in low speeds than in high. Furthermore, a higher temperature of the bearing, which lowers the viscosity of the grease, results in a greater sliding friction coefficient over

a longer speed span. When the radial load is fairly low the rolling friction dominates the sliding friction over the whole speed range. However, when the load gets close to 1 kN and the temperature is high, the sliding friction constitutes the greatest part of total bearing friction at low speeds since G_{sl} increases faster with the radial load compared to G_{rr}. All the empirical equations to derive the factors in (3.22) and (3.23) for various types and sizes of bearing types can be found in [77].

SKF online tool for the bearing calculation uses the aforementioned equations to calculate the friction torque of the bearings. Figure 3.4 shows the friction torque calculated with the online tool for the bearing "SKF 6208" that is mounted in one of the tested machines (Figure 3.4a) and retardation test results as a function of different temperatures (Figure 3.4b)[2].

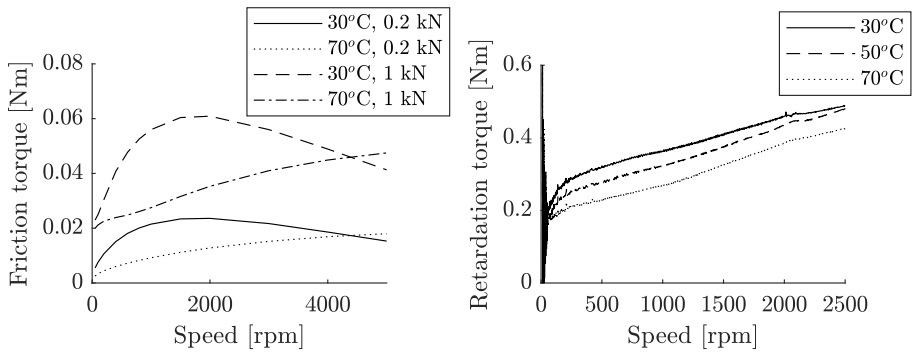

(a) Estimation of friction torque in a bearing.

(b) retardation tests at different temperatures.

Figure 3.4: Bearing friction torque analysis.

The calculations assume zero axial load, an operating temperature varying between 30 and 70^{o}C, and a radial load that varies between 0.2 kN (around 20 kg of mass) and 1 kN (around 100 kg of mass). Furthermore, the grease viscosity of the calculations is set to 96 mm^2/s at 40^{o}C and 10.5 mm^2/s at 100^{o}C (SKF LGHP 2 grease specifications). The effect of the reduction coefficients in (3.22) is seen clearly when the temperature of the bearing is 30^{o}C: the torque increases fast due to the high viscosity of the grease, but drops fast after the speed reaches a value where the reduction coefficients become significant. When the load is 1 kN and the temperature is 70^{o}C the torque is high at low speeds due to the sliding friction torque. However, when the speed increases the rolling friction is the dominating part of the total bearing friction torque.

As Figure 3.4 shows, the bearing friction torque has a very non-linear relationship with the speed, load and temperature, and is therefore difficult to separate from the other speed-

[2]The retardation test procedure is described in section 3.5.2

dependent loss torque components after testing. The retardation tests show that the temperature has a significant impact on the shaft torque (Figure 3.4b), and the trend is more or less in line with the expectations from the calculations (Figure 3.4a), even though the difference between the different temperatures is significantly larger in the results from the measurements. However, it should be pointed out that a large part of the retardation torque is due to iron losses that decrease with temperature as well. Since the relationships between the temperatures and the losses in both the bearings and the iron are complex, it is difficult to deduce which component that changes the most. In either case, the decrease of losses is consistent with the theory for both categories of loss phenomena.

The windage losses of an inner rotor radial flux machine can be estimated by considering the rotor and stator as two perfect cylinders in close proximity where the inner (the rotor) rotate in relation to the outer (the stator). This creates a so called Couette flow where viscous effects dominate and the inertial effects become negligible [80]. Considering a completely circumferential flow, the torque due to the Couette flow can be estimated by

$$T_{wind} = 4\pi v_{\text{Air}} \omega_m \frac{r_{ro}^2 r_{si}^2}{r_{si}^2 - r_{ro}^2} \tag{3.25}$$

where v_{Air} is the viscosity of air (which changes with temperature); ω_m is the angular speed of the rotor; and r_{ro} and r_{si} are the outer radius of the rotor, and the radius of the inner boundary of the stator, respectively. The equation above suggests a linear relationship between the windage torque and the mechanical angular velocity, and thus a power loss that depends on the angular velocity squared. However, after the rotor reaches a critical speed, so called Taylor vortexes appear in the air gap. A detailed analysis and description of this phenomenom is out of the scope of this thesis, but a good qualitative and quantitative explanation can be found in [80]. The critical angular speed when the air-gap width is negligible compared to the rotor radius is given by

$$\omega_c = 41.19 \frac{v_{\text{Air}}}{\rho_{\text{Air}} (r_{si} - r_{ro})^{1.5} \sqrt{\frac{r_{ro} + r_{si}}{2}}} \tag{3.26}$$

where ρ_{Air} is the density of air. After this angular speed is reached, the relationship between the windage torque and the angular speed becomes non-linear and hard to estimate. Furthermore, other flow regimes can occur after the first transition to Taylor vortex flows. These regimes further change the torque profile, and to do an accurate analytical estimation of the windage losses therefore becomes difficult. According to (3.26), the critical speeds for the two machines this work analyses become

$$n_{c,m1} = 1183 \text{ [rpm]}$$
$$n_{c,m2} = 2115 \text{ [rpm]}$$

Since these speeds are well within the operating range of the machine, the windage loss is difficult to predict. Furthermore, the irregularities in the stator due to the slot openings make the flow profile, and hence the torque due to windage, even more complex to foresee.

It should be mentioned that many publications suggest another equation for estimation of the windage torque

$$T_{wind} = \frac{\rho_{\text{Air}} \pi \omega_m^2 r^4 \mathcal{C}_{mc}}{2} \tag{3.27}$$

where $\mathcal{C}_{mc}$ is the moment coefficient and r is the radious [81–83]. Whether (3.27) holds or not depends on $\mathcal{C}_{mc}$. However, the calculations of [81–83] use a formula found in [84], which relates the moment coefficient to turbulent flows rather than flow domains as described in [80].

Power losses in the permanent magnets

Since permanent magnet materials are electrically conductive, eddy currents arise if magnets are subjected to a varying external magnetic field. In machines, this typically happens due to time harmonics (mostly due to the current ripple from the switching converter) and/or space harmonics (due to slotting effects and winding distribution). Generally, the losses in the magnets in IPMSMs with distributed winding schemes and sinusoidal modulations are quite small compared to the other speed-dependent loss components [85]. However, these losses may still have an important impact on the performance of the machine since 1) the rotor is rarely actively cooled, which means that the rate of heat transfer from the rotor to the stator and the surroundings is quite small, and 2) the skin effect yields highly concentrated losses. Considering this, the losses may lead to high enough local temperatures to irreversibly damage the magnets. With very short axial magnets, the loss density in the frequency domain can be quantified by

$$P_{loss,mag} = \frac{\sigma_{\text{pm}} l_m^2 \omega^2 B_p^2}{24} \tag{3.28}$$

where σ_{pm} is the conductivity of the permanent magnet material, l_m is the axial length of the magnet, and ω and B_p are the electrical angular velocity and the top value of the

external magnetic flux density, respectively [86]. However, in many cases the permanent magnets in machines are not laminated to the point that the aforementioned assumption holds. Therefore, the reaction field that the eddy currents in the permanent magnets give rise to must be taken into account for a more general solution to estimate the PM losses. To do this, an appropriate approximation assumes that the magnet is a rectangular conductive plate, and that the external magnetic field faces the plate perpecicular to its surface [87]. A change in the magnitude of the field gives rise to a current that circulate around the direction of the field vector. However, these currents give rise to a magnetic field that opposes the external source field. Therefore, the circulating currents in the plate are a function of both the external and the opposing field. A mathematical derivation of an expression for this includes Ampere's law, Faraday's law of induction, Helmholtz equations and Fourier series expansion and can be found in [86, 87]. A small modification of the method that includes the air gap in the loss estimation has proven relatively accurate for estimation of permanent magnet losses in IPMSMs [88, 89]. The equation is given by

$$P_{loss,mag} = abd\left(\frac{g_e}{d}\right)\frac{32\sigma_{\text{pm}}\omega^2 B_p^2}{4\pi}\sum_{n=1}^{\infty}\sum_{m=1}^{\infty}\frac{f_n(n,m)}{f_d(n,m)} \tag{3.29}$$

where a, b and d are the length, width and depth of the magnet, respectively; g_e is the effective air gap that is defined as the magnet depth plus the length of the physical air gap; σ_{pm} is the conductivity of the PM material; and ω and B_p are the angular frequency and the magnitude of the external flux density, respectively. The numerator $f_n(n,m)$ and denominator $f_d(n,m)$ of (3.29) are given by

$$f_n(n,m) = \left(\frac{1}{a(2n-1)}\right)^2 + \left(\frac{1}{b(2m-1)}\right)^2 \tag{3.30}$$

$$f_d(n,m) = \pi^4\left(\left(\frac{g_e}{d}\right)\left(\frac{(2n-1)}{b}\right)^2 + \left(\frac{g_e}{d}\right)\left(\frac{(2m-1)}{a}\right)^2\right)^2 + \omega\mu_0\sigma_{\text{pm}} \tag{3.31}$$

where $\omega\mu_0\sigma_{\text{pm}}$ represents the reactive field from the eddy currents in the permanent magnet. To visualise how the losses evolve with frequency according to (3.29), Figure 3.5 shows estimations of permanent magnet losses when varying the PM width and the segmentation of the magnets. The dimensions of the simulated magnet is 1 cm width, 10 cm axial length and 3 mm radial depth. Furthermore, the peak value of the external field is 0.01 T and the conductivity of the magnet is $6.7C \cdot 10^5$ S/m (0.01 T is an arbitrary value chosen to give an example of the losses, while the conductivity of the magnet is found in [23]). Both the change in width and the segmentation change the losses' relationship with the frequency (even if it is more prominent when the width increases). The field reaction of the permanent magnet is very visible when the width is 2 cm (Figure 3.5a), and it is clear that the reaction's

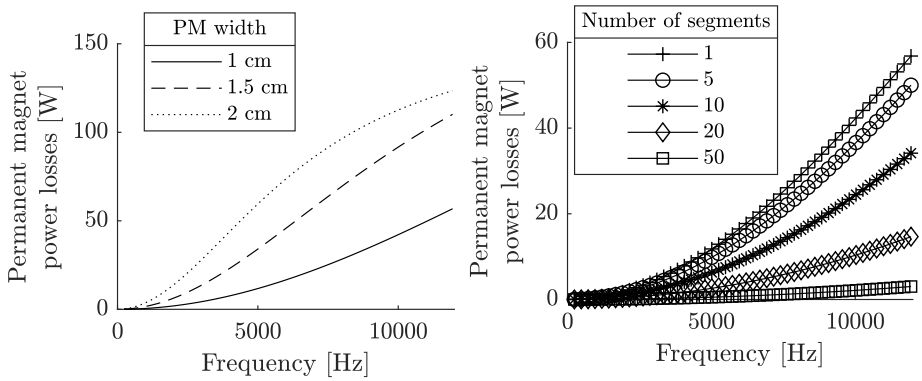

(a) Calculated losses in permanent magnets with different magnet width.

(b) Estimated losses in axially segmented permanent magnets.

Figure 3.5: Calculated permanent magnet losses for arbitrary magnets; the dimensions are described in the text.

influence of the losses is highly nonlinear and difficult to predict without calculations from e.g. (3.31).

Even though (3.29) yields a sound estimation of PM losses when the external field is sinusoidal and perpendicular to the surface of the magnet, the highly non-sinusoidal profile of the flux harmonics in the rotor of an IPMSM makes it challenging to estimate the permanent magnet losses accurately without FEM simulations. Studies show that in the case of machines where the permanent magnets are embedded in the rotor, time harmonics are the dominating cause of power losses in the permanent magnets [90]. However, this clearly depends on the number of slots per pole, winding distribution and current control strategies of the machines [85]. Furthermore, the placement of the magnets within the rotor also has an effect on the losses. As a conclusion, it is complicated to derive a direct connection between both the frequency and the magnitude of the currents and the losses in the permanent magnets. Consequently, this work does not attempt to distinguish the PM power losses form the total frequency-dependent power losses when the loss profiles of the machines are analysed.

Conclusions

The following main conclusions regarding the relationship between the power losses and the currents and the frequency can be drawn from the foregoing sections:

- The relationship between the frequency and the losses is very complicated. However,

the losses can be approximated to have a part that relates linearly to the frequency, consisting mainly of hysteresis losses and to a certain extent friction losses in the bearings. In addition, there is a part that relates to the square of the frequency consisting of macroscopic eddy currents in the iron, the windings and the permanent magnets, and to a certain extent windage losses. As described in the previous sections, these are crude estimations since the losses' relationship to the frequency changes a lot depending on dimensions, temperature, degradation and other factors. However, the simplification holds surprisingly well for the speed range that the following sections evaluate.

- The stator currents affect both the copper, the iron, and the permanent magnet losses. The microscopic eddy-current power losses in the iron (i.e. the hysteresis losses) tend to relate linearly to the frequency, while the rest of these losses relate to the square of the current, except in deep saturation, where the permeability of the iron, and hence the stator current's relationship to the magnetic flux density in the machine, change. Due to the spatial magnetic asymmetry of the stator (because of the slots and teeth) and the ripple of the current, the magnetic flux density in the machine tend to be nonsinusoidal, and it is therefore difficult to quantify the losses without FEM simulations. However, the losses due to the DC resistance and skin effect in the windings always relate to the square of the current, and since the DC resistance constitutes a large part of the losses in the machine in most operating points, the relationship is prominent in its loss profile (the following results section shows this explicitly).

3.4.2 Power loss models of this work

One of the purposes of this chapter is to find loss models that can be used for thermal modelling of machines. The models should estimate the losses using the same parameters the control system uses, i.e. the dq-axes currents and the frequency. One dynamic test sequence evaluates the losses for one specific current combination and the whole available speed range. Therefore, the first natural step in the modelling procedure is to find individual models that estimate the losses as functions solely of the frequency for each specific current combination. The second step combines these individual models to a holistic model that represents the loss behaviour of the whole operating range of the machine. Of course, as discussed earlier, the phenomena that govern the losses in electrical machines are very complex, and it is nearly impossible to find a model that takes all of them into account accurately. However, one can achieve an approximate model through the aforementioned steps with good results.

First step: models as functions of the speed

A loss model as a function of the speed (and consequently the angular velocity and the frequency) for one specific current combination can be created based on the loss torque estimations T_{loss} from (3.10) or on the power loss estimations P_{loss} from (3.9), depending on its purpose and the measurement data. The loss torque models provide good insights into the speed-dependent loss behaviour of the test objects. Considering the conclusions of section 3.4.1, the loss torque for one current combination can be modelled with a first order polynomial as a function of the magnitude of the angular velocity

$$\hat{T}_{loss} = \hat{k}_l + \hat{k}_q \left|\omega\right| \tag{3.32}$$

where $\hat{k}_l$ and $\hat{k}_q$ change depending on the currents. The first coefficient, $\hat{k}_l$, approximates the loss torque that does not change with the angular velocity. Consequently, it quantifies the losses that increase linearly with speed. Therefore, the subscript of the coefficient is l, which stands for linear, even though the coefficient stands alone in (3.32). The value of $\hat{k}_l$ depends mainly on the hysteresis losses in the core of the machine, but it also relates to e.g. standstill friction torque of the bearings. The second coefficient, $\hat{k}_q$, quantifies the loss torque that increases with the angular velocity, and consequently the losses that increase with the square of the angular velocity. It has the subscript q, which stands for quadratic due to its relationship with the losses. The coefficient $\hat{k}_q$ depends mainly on the macroscopic eddy-current losses in the iron core, but also on the eddy-current losses in the windings and the permanent magnets and on additional mechanical loss phenomena. The least-square method provides a straight forward solution to derive the model coefficients of (3.32). A finite number of torque observations and regressors are obtained for each dq current combination

$$\mathbf{T_{loss},}_N = \begin{pmatrix} T_{loss,1} \\ \vdots \\ T_{loss,N} \end{pmatrix}, \Phi_N = \begin{pmatrix} 1 & \left|\omega_1\right| \\ \vdots & \vdots \\ 1 & \left|\omega_N\right| \end{pmatrix}$$

where all the observations in the $\mathbf{T_{loss},}_N$ array are derived with (3.10). A least-square estimation gives $\hat{k}_l$ and $\hat{k}_q$ as [91]

$$\begin{pmatrix} \hat{k}_l \\ \hat{k}_q \end{pmatrix} = \left(\Phi_N^T \Phi_N\right)^{-1} \Phi_N^T \mathbf{T_{loss},}_N \tag{3.33}$$

Figure 3.6 shows typical examples of loss torque estimations form (3.10) together with the models from (3.32) for two dq-axes current combinations (remember that the coefficients in (3.32) differ for each current combination). It is straight forward to qualitatively estimate if the loss torque agrees with the proposed model from (3.32) by analysing the results graphically. If the loss torque estimation results show a very nonlinear relationship with the speed, one can suspect that either 1) there are errors in the measurements or 2) the estimations of the electromagnetic torques are insufficient. The graphical analysis also gives an explicit indication to if the estimations are too noisy to result in satisfying models. This happens when the magnitude of acceleration becomes high, generally due to a high resulting torque from the tested current combination and/or a low moment of inertia of the rotating parts of the machine. Figure 3.6b shows a typical example of loss torque estimations that are too noisy for modelling purposes.

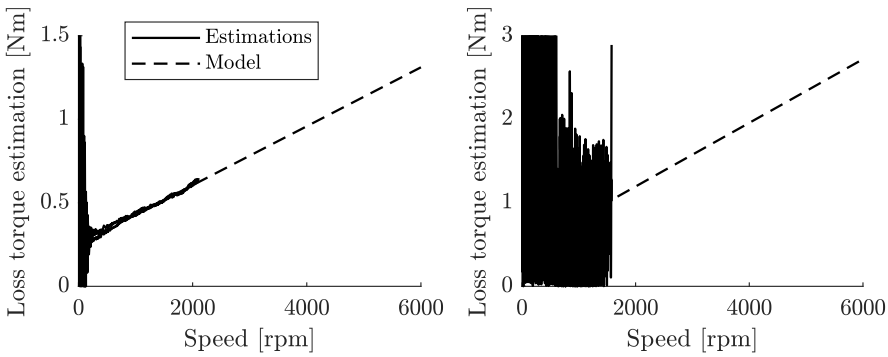

(a) Clean estimations fit for modelling. **(b)** Noisy estimations unfit for modelling.

Figure 3.6: Loss torque estimations and model example.

In addition to the loss torque estimations from (3.10), P_{loss} from (3.9) can be used as a base for modelling of the losses as well. The P_{loss} estimations are generally more resilient to noise than loss torque estimations, and the P_{loss} model approach is therefore advantageous if the tests are performed under high mechanical dynamics (however, the dynamics still must be fairly slow to yield good results). Furthermore, the P_{loss} estimations include the standstill losses, consisting mainly of losses due to the DC resistance in the copper winding. Consequently, the total losses can be modelled directly from the estimations, in contrast to (3.32) that only gives information about the losses that depend on the speed. However, compared to the T_{loss} estimations, P_{loss} results do not give the same possibility to explicitly analyse the speed-dependent loss behaviour of the machine graphically. According to the conclusions of section 3.4.1, the P_{loss} estimations can be modelled fairly accurately with a second degree polynomial

$$\hat{P}_{loss} = \hat{k}_{ss} + \hat{k}_l \left|\omega\right| + \hat{k}_q \omega^2 \tag{3.34}$$

where the coefficient $\hat{k}_{ss}$ quantifies the speed-independent losses, which consist mostly of ohmic losses in the stator windings but also of e.g. time harmonics due to the current ripple. The other two coefficients, $\hat{k}_l$ and $\hat{k}_q$, scale the estimations of the losses that increase linearly and quadratically with the speed, respectively, as in (3.32). An observation array and a regressor matrix are formulated as

$$\mathbf{P_{loss},}_N = \begin{pmatrix} P_{loss,1} \\ \vdots \\ P_{loss,N} \end{pmatrix}, \Phi_N = \begin{pmatrix} 1 & |\omega_1| & \omega_1^2 \\ \vdots & \vdots & \vdots \\ 1 & |\omega_N| & \omega_N^2 \end{pmatrix}$$

whereupon the coefficients in (3.34) are derived by least-square minimisation

$$\begin{pmatrix} \hat{k}_{ss} \\ \hat{k}_l \\ \hat{k}_q \end{pmatrix} = \left(\Phi_N^T \Phi_N\right)^{-1} \Phi_N^T \mathbf{P_{loss},}_N \tag{3.35}$$

A comparison between the coefficients from the model based on P_{loss} (3.34) and the coefficients from the model based on T_{loss} (3.33) is a good approach to analyse the validity of the models. Similar $\hat{k}_l$ and $\hat{k}_q$ in both models point toward good consistency of the results. It should be emphasised that (3.35) holds for one specific arbitrary dq-axes current combination. Consequently, the equation models the frequency dependence of the losses for one specific loading point.

Second step: models as functions of the currents

The second step of the modelling process aims to find appropriate models for the coefficients $\hat{k}_{ss}$, $\hat{k}_l$ and $\hat{k}_q$ from (3.33) and (3.35) as functions of the d- and q-axis currents. This makes it possible to estimate the loss torque and the power losses as functions of both the angular velocity and the currents. To derive models for the coefficients, the polynomials from the first modelling step, (3.32) and (3.34), are firstly assumed to give the true loss torque/power losses for each current combination. Furthermore, the coefficients are assumed to be functions of the currents only. Following this, the assumed "true" loss torque and power losses can be formulated as

$$T_{loss} = k_l^{\left(i_d^s, i_q^s\right)} + k_q^{\left(i_d^s, i_q^s\right)} \left|\omega\right| \tag{3.36}$$

and

$$P_{loss} = k_{ss}^{\left(i_d^s, i_q^s\right)} + k_l^{\left(i_d^s, i_q^s\right)} |\omega| + k_q^{\left(i_d^s, i_q^s\right)} \omega^2 \tag{3.37}$$

The list below presents the equations that are used to model the coefficients.

$k_{ss}^{\left(i_d^s, i_q^s\right)}$ The first coefficient, which represent speed-independent losses, is modelled as

$$\hat{k}_{ss}^{\left(i_d^s, i_q^s\right)} = \hat{R}_{eq} \left(i_d^{s2} + i_q^{s2}\right) \tag{3.38}$$

where $\hat{R}_{eq}$ is an unknown coefficient. Notice that $\hat{k}_{ss}$ has the unit Watt. Therefore, $\hat{R}_{eq}$ becomes an equivalent resistance with the unit Ω. The model is designed as (3.38) since the losses from R_{DC}, (3.15), dominate the speed-independent losses. Consequently, $\hat{R}_{eq}$ has a similar value to R_s in most machines if the dq currents are obtained with a power-invariant transformation. When estimating $\hat{R}_{eq}$, the observations are the estimated $\hat{k}_{ss}$ from (3.34) for different currents, and the observation array and the regressor array for the least-square minimisation therefore become

$$\mathbf{k}_{\mathbf{ss},N}^{\left(\mathbf{i_d^s}, \mathbf{i_q^s}\right)} = \begin{pmatrix} \hat{k}_{ss,1} \\ \vdots \\ \hat{k}_{ss,N} \end{pmatrix}, \Phi_N = \begin{pmatrix} i_{d,1}^{s2} + i_{q,1}^{s2} \\ \vdots \\ i_{d,N}^{s2} + i_{q,N}^{s2} \end{pmatrix}$$

The equivalent resistance is estimated by least-square minimisation according to

$$\hat{R}_{eq} = \left(\Phi_N^T \Phi_N\right)^{-1} \Phi_N^T \mathbf{k}_{\mathbf{ss},N}^{\left(\mathbf{i_d^s}, \mathbf{i_q^s}\right)} \tag{3.39}$$

$k_l^{\left(i_d^s, i_q^s\right)}$ Due to the highly non-linear behaviour of the microscopic eddy currents and the complicated characteristics of the mechanical losses, it is difficult to derive models based on physics that accurately predict the losses that increase linearly with the frequency. In this case, the model is based on the assumption that the losses relate to the square of the top value of the magnetic flux density (α_h in (3.11) is two). Furthermore, the d- and q-axis currents are assumed to affect the flux density linearly. In addition, a coupling term between the dq-axes currents is added to model cross-coupling phenomena between the magnetic fluxes that the currents give rise to. These assumptions result in the model

$$\hat{k}_l^{\left(i_d^s, i_q^s\right)} = \hat{k}_l^{\mathrm{I}} + \hat{k}_l^{\mathrm{II}} \cdot i_d^{s2} + \hat{k}_l^{\mathrm{III}} \cdot i_q^{s2} + \hat{k}_l^{\mathrm{IV}} \cdot i_q^s i_d^s \tag{3.40}$$

where $\hat{k}_l^{\mathrm{I}}$ is a function of the flux density in the machine due to the permanent magnets and the friction torque of the bearings. An observation array, based on $\hat{k}_l$ from (3.32) or (3.34), and a regressor matrix are formulated as

$$\mathbf{k}_{\mathrm{l},N}^{\left(\mathbf{i}_\mathbf{d}^\mathbf{s},\mathbf{i}_\mathbf{q}^\mathbf{s}\right)} = \begin{pmatrix} \hat{k}_{l,1} \\ \vdots \\ \hat{k}_{l,N} \end{pmatrix}, \Phi_N = \begin{pmatrix} 1 & i_{d,1}^{s2} & i_{q,1}^{s2} & i_{q,1}^s i_{d,1}^s \\ \vdots & \vdots & \vdots & \vdots \\ 1 & i_{d,N}^{s2} & i_{q,N}^{s2} & i_{q,N}^s i_{d,N}^s \end{pmatrix}$$

whereupon the coefficients from (3.40) are estimated by

$$\begin{pmatrix} \hat{k}_l^{\mathrm{I}} \\ \hat{k}_l^{\mathrm{II}} \\ \hat{k}_l^{\mathrm{III}} \\ \hat{k}_l^{\mathrm{IV}} \end{pmatrix} = \left(\Phi_N^T \Phi_N\right)^{-1} \Phi_N^T \mathbf{k}_{\mathrm{l},N}^{\left(\mathbf{i}_\mathbf{d}^\mathbf{s},\mathbf{i}_\mathbf{q}^\mathbf{s}\right)} \tag{3.41}$$

This model can prove to be insufficient when the machine saturates deeply since the relationship between the currents and the magnetic flux density is no longer linear. Therefore, the model must be validated to confirm that it represents the losses with satisfying accuracy.

$k_q^{\left(i_d^s, i_q^s\right)}$ The loss coefficient that relates to the square of the frequency is modelled based on the equation for the classical iron losses (3.12). Assuming a linear relationship between the currents and the magnetic flux density, the model becomes

$$\hat{k}_q^{\left(i_d^s, i_q^s\right)} = \hat{k}_q^{\mathrm{I}} + \hat{k}_q^{\mathrm{II}} \cdot i_d^{s2} + \hat{k}_q^{\mathrm{III}} \cdot i_q^{s2} + \hat{k}_q^{\mathrm{IV}} \cdot i_q^s i_d^s \tag{3.42}$$

where $\hat{k}_q^{\mathrm{I}}$ is a function of the flux density from the permanent magnets and mechanical loss phenomena, and $\hat{k}_q^{\mathrm{IV}} \cdot i_q^s i_d^s$ models the effects of magnetic cross coupling. The observation array and the regressor matrix are formulated as

$$\mathbf{k}_{\mathbf{q},N}^{\left(\mathbf{i}_\mathbf{d}^\mathbf{s},\mathbf{i}_\mathbf{q}^\mathbf{s}\right)} = \begin{pmatrix} \hat{k}_{q,1} \\ \vdots \\ \hat{k}_{q,N} \end{pmatrix}, \Phi_N = \begin{pmatrix} 1 & i_{d,1}^{s2} & i_{q,1}^{s2} & i_{q,1}^s i_{d,1}^s \\ \vdots & \vdots & \vdots & \vdots \\ 1 & i_{d,N}^{s2} & i_{q,N}^{s2} & i_{q,N}^s i_{d,N}^s \end{pmatrix}$$

and the coefficients from (3.42) are estimated by

$$\begin{pmatrix} \hat{k}_q^{\mathrm{I}} \\ \hat{k}_q^{\mathrm{II}} \\ \hat{k}_q^{\mathrm{III}} \\ \hat{k}_q^{\mathrm{IV}} \end{pmatrix} = \left(\Phi_N^T \Phi_N\right)^{-1} \Phi_N^T \mathbf{k}_{\mathbf{q},N}^{\left(\mathbf{i}_\mathbf{d}^\mathbf{s},\mathbf{i}_\mathbf{q}^\mathbf{s}\right)} \tag{3.43}$$

As shown in the coming section 3.6, these loss torque and power loss models yield satisfying results for the machines that are evaluated in this thesis within the tested current and speed range. However, the good results cannot be taken for granted in a general case, and the outcoming models must always be analysed before confirming their validity.

Conclusions

The sections above describe an approach to model the losses of an IPMSM based on measurements of the loss torque and the power losses. The main conclusions from the sections are

- The first step of the modelling treats each current combinations separately. Estimations of both T_{loss} and P_{loss} can be used as data for the modelling procedure. The loss torque model includes two constants, where the first represents a constant braking torque and the second a braking torque that increases linearly with frequency. The model based on the P_{loss} estimations includes three terms: one represents the speed-independent losses in the machine, one the losses that increase linearly with frequency, and one the losses that increase with the square of the frequency. Results from the following section 3.6 show that these models represent the losses of the evaluated test objects well.
- The second step derives models that estimate the constants of the individual P_{loss} models from the first step. The new models are based on analytical expressions of the DC resistive losses, the hysteresis losses, and the classical eddy current losses.
- It is very important to be attentive and flexible in the modelling procedure. The models of this section work as a good starting point and give good results for the machines that this work evaluate (within the tested current and speed range). However, even if the proposed models are based on a generic and somewhat physical approach, this thesis does not prove any generality of the developed models and they should be revised for each individual machine design.

3.5 Dynamic tests for loss estimation

3.5.1 Measurement procedure

The dynamic measurement procedure for the loss estimation tests is almost identical to the test procedure for the magnetic model derivation presented in section 2.3.1. Nevertheless, there are some additional aspects that must be taken into account.

Maximum speed

The rotational speed of the rotor should be as high as possible for each evaluated current combination to make the test range sufficiently wide. The derivation of the maximum angular velocity is not trivial since it depends on many things: Which DC voltage is available? Which modulation strategy is used? Should it be possible to go into over modulation during the tests? In either case, it is clear that the maximum angular velocity relates mostly to the induced voltage and the resistive voltage drop over the stator windings as long as the maximum speed limit for the bearings is not exceeded and the mechanical integrity of the rotating parts is not compromised. The magnitude of the voltage vector can be expressed as a function of dq-axes stator currents and linked magnetic fluxes, the angular velocity and the stator resistance by substitution with (2.6) and (2.7)

$$|\overrightarrow{u}| = \sqrt{u_d^2 + u_q^2} = \sqrt{\left(R_s i_d^s - \omega \psi_q^{\left(i_d^\psi, i_q^\psi\right)}\right)^2 + \left(R_s i_q^s + \omega \psi_d^{\left(i_d^\psi, i_q^\psi\right)}\right)^2} \tag{3.44}$$

The linked magnetic fluxes stay approximately the same regardless of the angular velocity, and their notation can therefore be rewritten for space convenience $\psi^{\left(i_d^\psi, i_q^\psi\right)} \approx \psi^{(i_d^s, i_q^s)} = \psi$. The expression for the magnitude of the voltage vector is expanded to

$$|\overrightarrow{u}| = \sqrt{R_s^2\left(i_d^{s2} + i_q^{s2}\right) + \omega^2\left(\psi_d^2 + \psi_q^2\right) + 2R_s\omega\left(i_q^s\psi_d + i_d^s\psi_q\right)} \tag{3.45}$$

If the dq currents and the linked magnetic fluxes are constant, the angular velocty is the only thing that affects the magnitude of the voltage vector. A rearrangement of (3.45) gives the expression for the maximum angular velocity of a specific current combination

$$\omega_{max} = \sqrt{\frac{R_s^2(\psi_q i_d - \psi_d i_q)}{(\psi_d^2 + \psi_q^2)^2} - \frac{R_s^2(i_d^2 + i_q^2) - |\overrightarrow{u}|_{max}^2}{\psi_d^2 + \psi_q^2}} - \frac{R_s(\psi_q i_d - \psi_d i_q)}{\psi_d^2 + \psi_q^2} \tag{3.46}$$

where $|\overrightarrow{u}|_{max}$ is the maximum allowed voltage, which is decided by the converter DC voltage and the modulation index. For example, a pure sinusoidal modulation (often denoted suboscillation modulation) allows a maximum voltage of $\frac{U_{dc}}{2}$, while introductions of various zero sequence components in the inverter voltage yield an increase in the allowed voltage. In this work, symmetrical suboscillation modulation (or simply symmetical

modulation) is applied. This modulation technique yields a maximum voltage vector magnitude of $\frac{U_{dc}}{\sqrt{2}}$ with a power-invariant transformation. The technique is explained further in Appendix C.

Moment of inertia of the rotating parts

A significant difference between the estimation of the magnetic model and the estimation of the power losses is that it is not possible to average all measurements over a complete dynamic test sequence when estimating the losses[3]. Therefore, the dynamic tests for the loss estimation require that the magnitudes of acceleration are significantly lower than in the magnetic model estimation tests. It is difficult to give an absolute recommendation to how fast/slow the dynamics should be to yield sufficiently accurate results. The experiments in this work show that a torque of around 50 Nm, which gives a magnitude of acceleration of around 185 m/s^2 is on the limit. Higher torques results in measurements that include too much noise to be analysed properly. However, variables such as stability of the mechanical test setup, the current controller of the drive and the intrinsic design of the test object surely affect this limit significantly.

In addition to have a sufficiently high moment of inertia it is necessary to have an accurate estimate of it to calculate the mechanical power from the measurements. One way to slow down the mechanical dynamics is to mount a flywheel on the shaft. If the moment of inertia of the rotor and the flywheel is known, the total moment of inertia of the rotating mass can be calculated with addition. However, sometimes information about the moment of inertia is not available. In such cases, one can compare the electromagnetic torque with the acceleration to find the moment of inertia. The acceleration of an unloaded electrical machine can be expressed as

$$\frac{d\omega_m}{dt} = \frac{T_{em} + T_{loss}}{J} \tag{3.47}$$

where T_{em} is the electromagnetic torque, T_{loss} is the loss torque and J is the moment of inertia. The magnitude of the loss torque is regarded as approximately the same independently if the machine works in generator or motor operation as long as the stator currents that yield T_{em} remain the same (the currents remain but the rotational direction of the rotor changes from motor to generator operation). However, in generator operation T_{loss} has the same sign as T_{em}, while it has the opposite when the machine operates as a motor. Therefore, the electromagnetic torque can be calculated as the mean value of the acceler-

[3]The averaging of data is possible when the proposed method estimates the magnetic model since it suppose that the flux linkage is independent of the speed, see section 2.3.1.

ation times the moment of inertia for motor and generator operation if the magnitude of the angular velocity is the same

$$\left(\left| \frac{d\omega_m^{|\omega_J|}}{dt} \right| + \left| \frac{d\omega_m^{-|\omega_J|}}{dt} \right| \right) = 2\frac{T_{em}}{J} \tag{3.48}$$

where $|\omega_J|$ is the magnitude of an arbitrary angular velocity. Combining (2.19) and (3.48), it is possible to find an expression for the moment of inertia of the machine

$$J = 2\frac{n_{pp}\left(i_q^s \psi_d^{\left(i_d^s, i_q^s\right)} - i_d^s \psi_q^{\left(i_d^s, i_q^s\right)} \right)}{\left(\left| \frac{d\omega_m^{|\omega_J|}}{dt} \right| + \left| \frac{d\omega_m^{-|\omega_J|}}{dt} \right| \right)} \tag{3.49}$$

Publications from the author show that this method of inertia estimation works well compared to a trifilar pendulum method; the study is presented in paper IV in the list of publications.

3.5.2 Retardation tests

The retardation test is an excellent complement to the dynamic tests for derivation and analyses of the losses. The test is well defined and included in testing standards for electrical machines [48, 49]. The list below describes the procedure

1. The machine is accelerated up to base speed where the induced voltage limits the angular velocity[4].
2. The reference current is set to zero and the phases are disconnected.
3. The internal power losses slow down the machine to zero speed. In this stage the shaft torque and speed yield the mechanical power, which corresponds to the losses in the machine.

The shaft torque and speed can be measured in different ways, but if a position sensor is mounted on the shaft of the machine, a multiplication between the derivative of the position (the speed) with the second derivative (the acceleration) and the moment of inertia

[4]It is however possible to reach significantly higher speeds if a field-weakening current is applied during the retardation. Nevertheless, this obviously affects the losses and therefore gives a different (but not necessarily less relevant) result.

of the shaft constitutes the most straight forward way to obtain the braking power. In addition to actually disconnecting the phases during the retardation, it is also possible to open the switches of the converter, or to set the reference of the current controller to zero. This gives additional information about the loss behaviour of the machine. In addition to the power losses from the retardation tests, the shaft torque during the braking process gives substantial information about the different components of the losses. This type of analysis is used to a high extent in the following sections.

3.6 Experimental tests

3.6.1 Experimental preconditions and limitations

The reader should notice that the current and the speed range of the results that the following section presents are limited considering that the machines are designed for traction applications (a more elaborated presentation of the machines can be found in Appendix A). The narrow range of the results is due to some important restrictions in the test setup that was used throughout the work:

- **Voltage limit.** The DC-link voltage for the power converter of the test setup was supplied by a rotating converter in which a grid connected induction machine drives a DC generator. This solution has some drawbacks: When the power dynamics of the load (in this case the test object) are high, the DC voltage tends to rise if the test object works as a generator, and fall if the test object works as a motor. Furthermore, the voltage oscillates when the machine changes fast from motor to generator operation, or vice versa. Because of this, the maximum speed of the results that are presented is lower than the actual tested maximum speed. The maximum DC voltage in the test setup was 400 V, with a maximum total swing of about 20 V at the maximum loading current. The voltage is sufficient for the first test object, but not the second one, which is rated for 600 V. The next section introduces the test objects of the study.

- **Current limit.** The maximum average DC current supply that could be achieved before tripping the fuse was 63 amperes. However, the power of the rotating converter limited the DC current to around 50 Amperes with a sufficiently high DC link voltage. Consequently, the maximum power of the system is around 20 kW.

- **Mechanical limits.** In addition to the electrical constraints, the maximum speed was limited by mechanical safety issues. The energy of the rotating mass becomes very high at high speeds – especially when a flywheel with a high moment of inertia is mounted on the rotor shaft. Therefore, the definitive maximum speed limit of

the tests was 5000 rpm (however, due to the aforementioned limitations of the DC source, the presented results does not exceed 4500 rpm).

The full description of the test setup including a presentation of sensors and drives is found in Appendix A.

Test objects

The first test object that this chapter evaluates – **machine 1** – is the same machine that acts as test object in chapter 2 and 4; appendix A presents details about the test objects of the thesis. The test object is a 20 kW machine designed to be operated with a DC-link voltage of 300 V. It has a base and a top speed of 3000 rpm and 15000 rpm, respectively, and a rated and a peak torque of 60 Nm and 100 Nm, respectively. A flywheel with a high moment of inertia was mounted on the rotor shaft during the tests to slow down the mechanical dynamics. This is crucial to derive usable results with the dynamic procedure. As a matter of fact, even with the heavier flywheel, the moment of inertia of the rotor shaft was still too small to measure losses at currents significantly higher than the rated. Therefore, the q-axis currents only reach 50 A, which results in a maximum acceleration of around 189 rad/s^2. This can be compared to the tests for the electromagnetic characterisation that evaluate the machine up to a q-axis current of 70 A, resulting in a maximum acceleration of 244 rad/s^2. These results confirm the need of a high enough moment of inertia of the rotating part of the machine for loss measurements over a wide speed and torque range.

The second machine that this work evaluates – **machine 2** – has a considerably higher power rating than **machine 1**. The test object is a 80 kW machine designed to be operated with a DC-link voltage of 600 V. It has a base and a top speed of 6000 rpm and 15000 rpm, respectively, and a rated and a peak torque of 125 Nm and 250 Nm, respectively. Due to the limitation of the test setup, the tests only cover a small part of the operating range of the machine in terms of both current and speed. Nevertheless, the following sections still confirm the usability of the evaluation and modelling approaches of this work. The same flywheel that was mounted on the rotor shaft of **machine 1** throughout the tests was also mounted on **machine 2**. Since **machine 2** has a lower nominal torque for the same current compared to **machine 1**, the mechanical dynamics did not limit the tests within the allowed testing current range of the electrical power source. However, at the loading point where the machine produces the highest torque (the maximum acceleration in this operation point is around 189 rad/s^2) the estimations are quite noisy.

Conventional tests

Unfortunately there was no possibility to test the machines with a dynamo and a torque sensor in the same facilities as where the dynamic tests were conducted due to lack of equipment and funds. This is of course a setback for the credibility and impact of this work. However, conventional tests with the input-output method were performed in AB Volvo's facilities on **machine 2** (but it should be emphasised that Dr Rasmus Andersson did perform the tests and not the author). The drive and control system at Volvo was not accessible and the controller of the machine could consequently not be affected. Furthermore, the DC bus voltage was set to 600 Volts while the maximum voltage at the dynamic test facilities was 400 V. Considering this, the results from the conventional tests and the dynamic tests are expected to diverge. Regardless, a comparison is still valuable to confirm that the results are relatively consistent.

Influence of the flywheel

During the tests of the machines, the same heavy flywheel was mounted on the rotor shafts of both the machines to decrease the magnitudes of acceleration. However, even though the slower dynamics help with the tests, the flywheel also introduces additional losses to the systems. At first, these losses were assumed to be so small that they would not affect the outcome of the results significantly. However, after analyses of results from retardation tests, it became apparent that the losses the flywheel introduces cannot be neglected in the total loss estimation of the machines. Figure 3.7 shows results of the loss torque form retardation tests of both machines when the flywheel is mounted and when it is not, and also the estimated retardation torque after a compensation strategy is introduced. The flywheel introduces similar losses to both the machines (with the exception of an additional small offset which is introduced in **machine 1**). Since the difference in loss torque depends on the speed, a reasonable theory is that the major part of the additional losses are due to windage torque. The torque due to windage on a rotational cylinder can be estimated by (3.27), where the moment coefficient is a function of the Reynolds number

$$\mathcal{C}_{mc} = \left(\frac{1}{-0.8572 + 1.25 \mathrm{Re}_{\phi} \sqrt{\mathcal{C}_{mc}}} \right)^2 \tag{3.50}$$

The rotational Reynolds number Re_{ϕ} in the equation above is expressed as

$$\mathrm{Re}_{\phi} = \frac{\rho_{\mathrm{Air}} \omega r^2}{v_{\mathrm{Air}}} \tag{3.51}$$

where v_{Air} is the viscosity of the air (equation (3.50) only holds if the flow is tubulent). Since (3.50) cannot be calculated analytically, it is not possible to introduce (3.27) directly as an

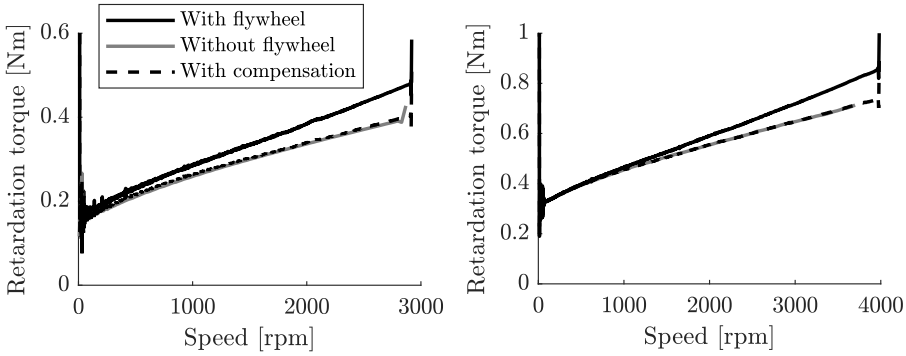

(a) Machine 1 **(b) Machine 2**

Figure 3.7: Retardation torque with and without the flywheel mounted on rotor shaft together with a compensation for the additional retardation torque that the flywheel introduces.

analytical compensation for each frequency. However, one can derive an estimation of the torque for a number of frequencies (for each frequency, the moment coefficient is derived numerically), and fit a polynomial that estimates the losses. Figure 3.8a shows the moment coefficient as function of the speed, and Figure 3.8b shows the resulting calculated windage torque for a number of speeds together with the fitted polynomial. The moment coefficient drops significantly when the speed increases, which means that the windage torque does not relate completely quadratically to to the speed as (3.27) suggests. However, a second order polynomial still suffices to approximate the calculated windage torque well. If the windage torque is estimated only by the aforementioned second order polynomial, it becomes too low to compensate for the extra torque the flywheel gives rise to. However, if the polynomial is scaled by a factor 2.8 the compensated torque fits almost perfectly. This scaling factor was derived empirically and does not have any known relationship to any physical phenomenon. Consequently, the author does not have any explanation or reason to why it results in such good compensations. Nevertheless, it should be emphasized that this model does not aim to give an explicit explanation to the extra torque; it is only designed to compensate for the torque the flywheel introduces. As such, the model gives sufficiently good compensation results regardless of the lack of physical understanding.

In addition to the speed-dependent torque, the flywheel introduces a speed-independent braking torque on **machine 1**. A probable explanation to this is that axial load that the flywheel introduces on the bearings give rise to an increase in the mechanical friction. However, it can also be due to a small error in the estimation of the moment of inertia. The additional braking torque is quantified to 0.012 Nm.

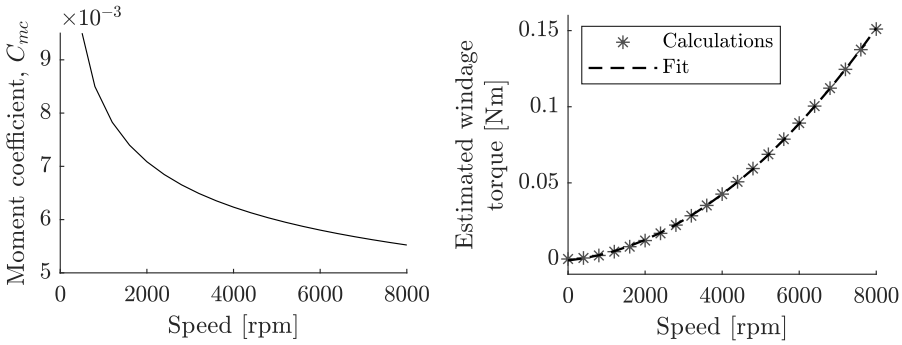

(a) Moment coefficient.

(b) Estimated windage torque and fitted polynomial.

Figure 3.8: Moment coefficient calculated with (3.50) and (3.51), and windage torque estimations together with a fitted second order polynomial.

Influence of the converter

The retardation test yields a straight forward way to investigate how the converter, and consequently also the current controller, affect the losses in the machine. Firstly, the machine is retarded without the converter. Secondly, the converter is connected, and the same current controller that controls the machine throughout the dynamics tests holds the current to zero while the machine retards. Two important aspects must be considered when performing the tests: Firstly, the quasi-instantaneous mean value of the electrical power must be zero during the retardations. If not, the acceleration does not yield only the losses, but it also reflects the power that flows in or out from the machine during the tests. If the electrical power is not zero it must be compensated for in the post-processing of the data. Secondly, the converter influences the losses differently depending on which loading point the machine operates in; even if the time harmonics from the current ripple are approximately equal, the harmonic content of the induced voltage changes with the current combination. The more harmonics the induced voltage contain, the harder it is for the current controller to output a voltage that yields a sinusoidal current. As a consequence, the harmonic content of the currents that correlates with the speed-dependent losses of the machine changes. Since the harmonic content of the induced voltage increases steeply with the field-weakening current, the speed-dependent losses due to the converter are expected to increase with a negative d current.

It is difficult to predict the current controller's influence on the machine losses. Therefore, simulations generally neglect the influence of the converter, which is one of the reasons why they often underestimate the losses. To minimise this error, one can create an approximate model that simulates the influence of the current controller from the retardation test results.

As discussed above, the model cannot be expected to accurately estimate the losses over the whole operating range since the harmonic content of the induced voltage changes. Nevertheless, the aforementioned compensation strategy is better than not taking the losses from the power converter into account at all. An analysis of the results from the retardation tests with and without a power converter shows that a model that increases linearly with the speed models the additional losses due to the converter quite well. This implies that the additional losses mainly consist of classical eddy current losses. However, it should be emphasised that the model does not aim to explain specific physical phenomena since that is out of the scope of this thesis. Instead, the model simply gives a quantitative estimation of the losses. Mathematically the model is formulated as

$$T_{converter} = \kappa \cdot |\omega_m| \tag{3.52}$$

where κ is an empirically derived constant and ω_m is the mechanical angular velocity. The compensation constants for the two evaluated test objects become

$$\kappa_1 = 4.29 \cdot 10^{-4} \tag{3.53}$$

$$\kappa_2 = 6.39 \cdot 10^{-4} \tag{3.54}$$

The results from retardation tests with and without converter together with the model for the losses are shown in Figure 3.9.

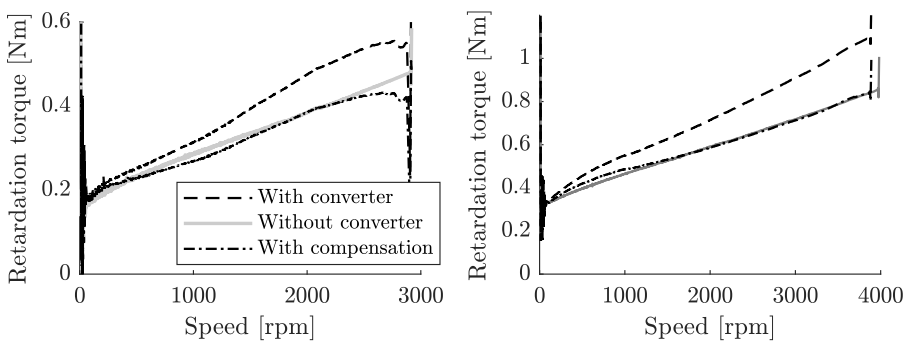

(a) Machine 1 **(b) Machine 2**

Figure 3.9: Loss torque measurements with and without a converter together with the compensated results.

3.6.2 Results from moment of inertia estimations

The moment of inertia of the rotating parts of the machines are estimated according to the method presented in section 3.5.1 with (3.49). The rotating parts include the rotors the flywheel that was used for both the machines throughout the tests. Table 3.1 shows the results for each tested current combinations.

Table 3.1: Moment of inertia estimation of the two machines [$\mathrm{kg \cdot m^2}$].

i_q^s/i_d^s	0	-10	-20	-30	-40	-50	-60	-70
10	0.2711	0.2705	0.2711	0.2708	0.2711	0.2707	0.2712	0.2720
20	0.2712	0.2702	0.2704	0.2711	0.2714	0.2696	0.2716	0.2718
30	0.2712	0.2702	0.2705	0.2709	0.2714	0.2718	0.2717	0.2717
40	0.2710	0.2705	0.2701	0.2708	0.2708	0.2720	0.2724	0.2718
50	0.2711	0.2705	0.2707	0.2705	0.2709	0.2717	0.2712	0.2720

(a) Machine 1

i_q^s/i_d^s	0	-10	-20	-30	-40	-50	-60	-70	-80
10	0.2815	0.2817	0.2815	0.2816	0.2818	0.2820	0.2820	0.2821	0.2820
20	0.2815	0.2819	0.2818	0.2818	0.2819	0.2819	0.2821	0.2821	0.2822
30	0.2819	0.2820	0.2819	0.2821	0.2821	0.2822	0.2821	0.2821	0.2822
40	0.2819	0.2820	0.2822	0.2821	0.2821	0.2821	0.2822	0.2822	0.2821
50	0.2820	0.2821	0.2821	0.2823	0.2823	0.2822	0.2823	0.2823	0.2821
60	0.2822	0.2823	0.2821	0.2823	0.2821	0.2822	0.2823	0.2823	0.2822
70	0.2823	0.2824	0.2822	0.2824	0.2823	0.2824	0.2822	0.2822	0.2820
80	0.2823	0.2823	0.2825	0.2823	0.2825	0.2824	0.2825	0.2821	0.2823

(b) Machine 2

The mean value and the standard deviation of the moment of inertia estimations of the two machines become

$$\overline{J}_1 = 0.271\ \mathrm{kg \cdot m^2} \tag{3.55}$$
$$\eta_1 = 0.000292\ \mathrm{kg \cdot m^2} \tag{3.56}$$

$$\overline{J}_2 = 0.282\ \mathrm{kg \cdot m^2} \tag{3.57}$$
$$\eta_2 = 0.0000807\ \mathrm{kg \cdot m^2} \tag{3.58}$$

The machines have unexpectedly similar moment of inertia values considering that **machine 2** is rated for a significantly higher torque than **machine 1**. However, the mounted

flywheel has a considerably higher moment of inertia than the rotors of both the machines. Consequently, the relative difference between the total moment of inertia of the two machines when the flywheel is mounted on the rotor shafts is small. Since the moment of inertia estimation of **machine 2** includes more data points the standard deviation of its results is lower compared to the estimations of **machine 1**. Nevertheless, both standard deviations are small enough to confirm that the results are consistent. Moment of inertia estimations of this kind is looked in detail in number IV in the list of publication.

3.6.3 Results of $\hat{P}_{loss,mg}$ estimations

Figure 3.10 shows qualitative representations of the $\hat{P}_{loss,mg}$ estimations from **machine 1** derived with (3.5) (the difference between the mechanical shaft power and the electrical power on the machine terminals averaged over motor and generator operation, see section 3.3).

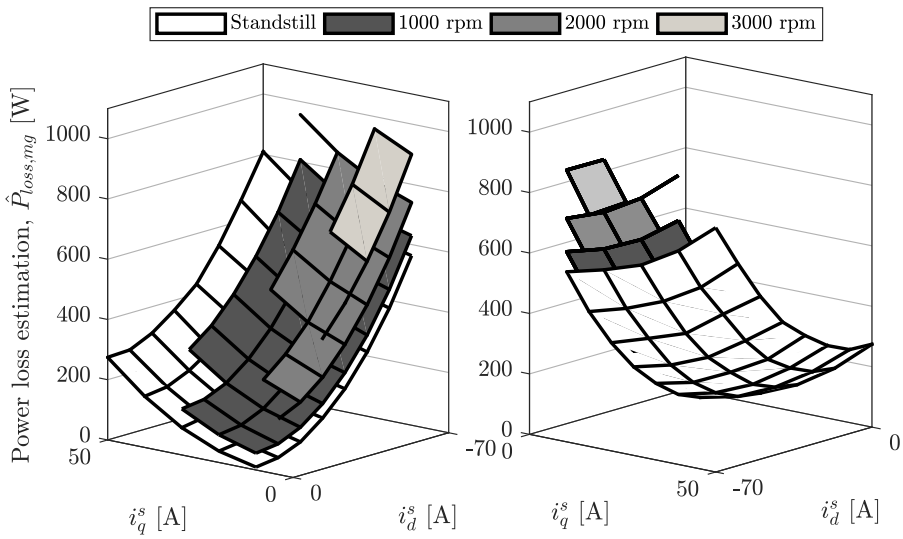

Figure 3.10: Estimated power losses ($\hat{P}_{loss,mg}$) results from **Machine 1**. The figures are shown from two different perspectives to clarify the results.

The results are shown as functions of all tested d- and q-axis currents, and for three speeds. The figure shows the results from two different perspectives for better visibility. The losses increase with the currents (mainly due to copper losses) and with the speed (mainly due to iron losses), which is in accordance with theory. Figure 3.11 shows the $\hat{P}_{loss,mg}$ estimations as in Figure 3.10 but for **Machine 2**. It is however hard to analyse the currents' influence on the speed-dependent losses in Figure 3.10 and Figure 3.11 since the speed-independent losses are very prominent.

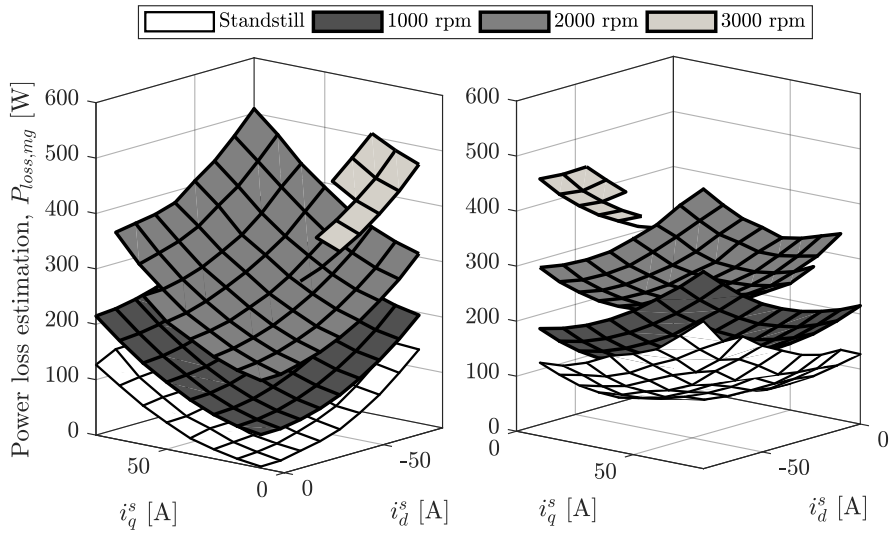

Figure 3.11: Estimated power losses ($\hat{P}_{loss,mg}$) results form **Machine 2**. The figures are shown from two different perspectives to clarify the results.

To give a clearer overview of the results, Figure 3.12 shows the losses as a function of the speed for different dq-axes current combinations; in Figures 3.12a and 3.12b, the d-axis current is zero and the q-axis current increases (from 10 to 50 A in steps of 10 A in **machine 1**, and 10 to 70 A in steps of 20 A in **machine 2**); in Figures 3.12c and 3.12d, the q-axis current is constant (10 A) and the d-axis current increases (from -10 to -70 A in steps of -10 A for **machine 1**, and 0 to -80 in steps of -20 A for **machine 2**). The figure shows that both the d- and the q-axis currents increase the losses in both machines. The results are quite surprising at a first glance since the fundamental part of the linked magnetic flux decreases with the negative d-axis current, which, according to the iron loss models in section 3.4.2, should result in reduced losses. However, the harmonic contents of the flux profiles of the machines increase in the field-weakening operation, and the losses consequently increase as well. Furthermore, the d-axis current imposes an external field on the permanent magnets. Even if this field should be constant, time and space harmonics make it vary. The variation yields eddy currents in the conductive coarsely laminated magnets, which in turn lead to additional losses.

Two other points worth to note from Figure 3.12 are that 1) the currents result in higher standstill losses in **machine 1** than in **machine 2**, and 2) **machine 1** reaches a lower speed at low field-weakening currents, and higher speed with high field-weakening currents compared to **machine 2**. The reasons for these phenomena are straightforwardly explained: the higher standstill losses in **machine 1** are due to a higher winding resistance, and the differences in speed are due to the different inductances in **machine 1** and **2**. The higher

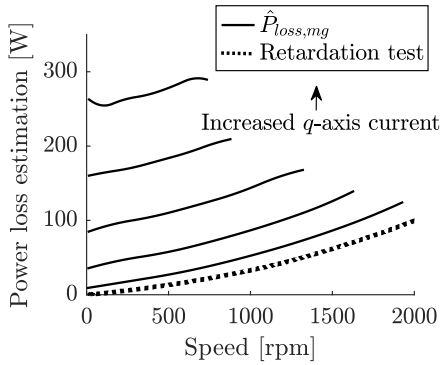

(a) Machine 1 i_q^s increases from 10 to 50 A in steps of 10 A.

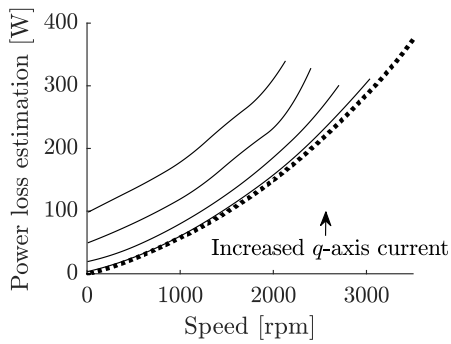

(b) Machine 2 i_q^s increases from 20 to 80 A in steps of 20 A.

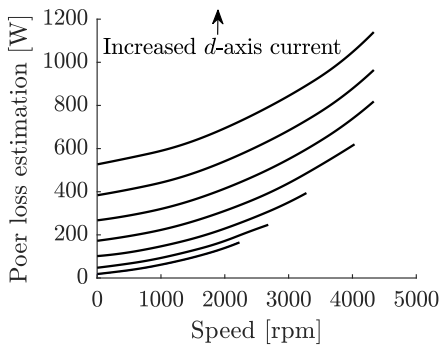

(c) Machine 1 i_d^s increases from -10 to -70 A in steps of -10 A.

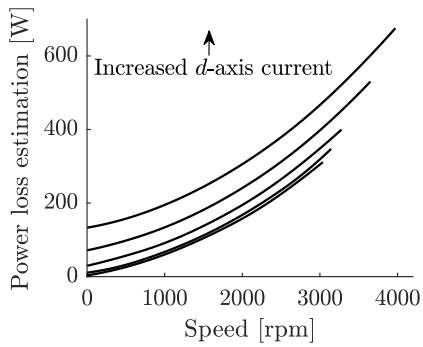

(d) Machine 2 i_d^s increases from 0 to -80 A in steps of -20 A.

Figure 3.12: $\hat{P}_{loss,mg}$ estimations for increasing d and q currents.

inductances of **machine 1** yield higher linked magnetic flux for the same current, which means that the q-axis currents generate a higher induced voltage, while the field-weakening currents lower the induced voltage more.

3.6.4 Analysis of $\hat{T}_{loss}$ estimations

A reasonable first step in the analysis of the loss torque is to examine how the electromagnetic torque estimations (derived by (3.6)) change with the frequency, and to compare them graphically to the mechanical torque estimations derived by (3.48). Figure 3.13 shows the electromagnetic and the mechanical estimated torque as functions of the speed for four different current combinations.

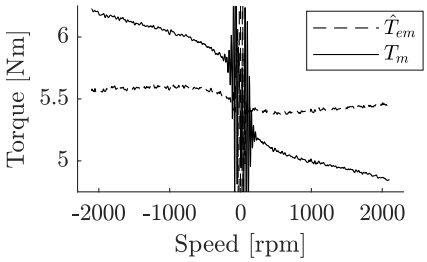

(a) Machine 1 $i_q^s = 10$, $i_d^s = 0$ A

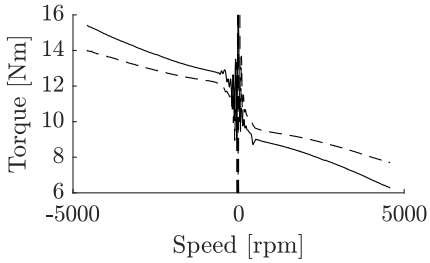

(b) Machine 1 $i_q^s = 10$, $i_d^s = -70$ A

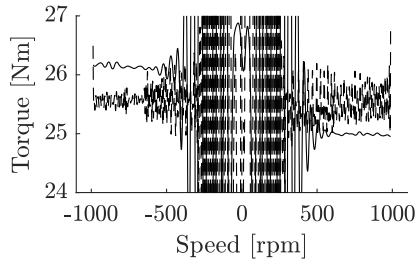

(c) Machine 1 $i_q^s = 50$, $i_d^s = 0$ A

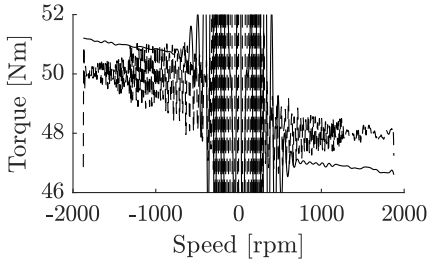

(d) Machine 1 $i_q^s = 50$, $i_d^s = -70$ A

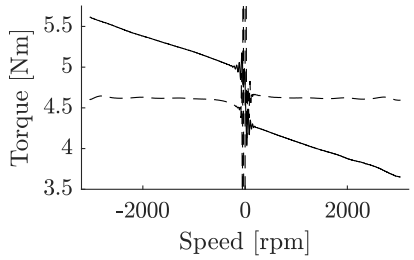

(e) Machine 2 $i_q^s = 10$, $i_d^s = 0$ A

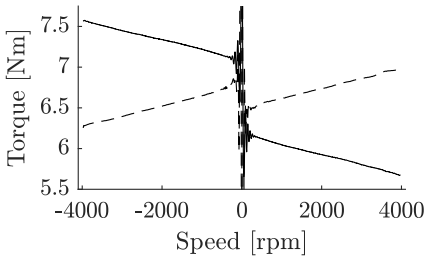

(f) Machine 2 $i_q^s = 10$, $i_d^s = -80$ A

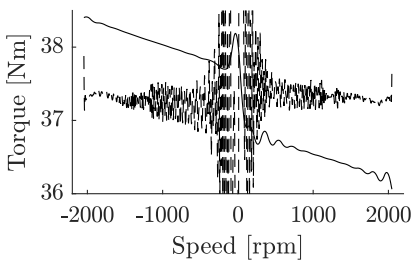

(g) Machine 2 $i_q^s = 80$, $i_d^s = 0$ A

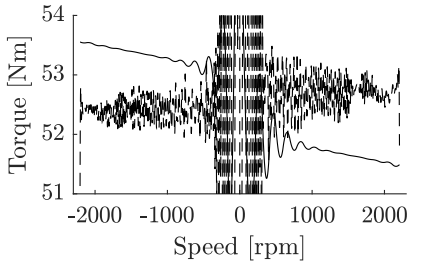

(h) Machine 2 $i_q^s = 80$, $i_d^s = -80$ A

Figure 3.13: Comparison between the estimated electromagnetic torque and the mechanical torque.

The figure illustrates two phenomena that should be noticed:

1. The electromagnetic torque estimations change with the speed. This is especially conspicuous in the results of **machine 1** when the field-weakening current is high (Figures 3.13b and 3.13d). The speed's influence on the electromagnetic torque estimations is not expected since the dq-axes currents remain the same over the whole speed range. However, since equation (3.6) does only remove the voltage drop due to the stator resistance from the dq-axes voltages when it estimates the linked magnetic flux, other phenomena that affect the voltage, but not necessarily the fundamental component of the electromagnetic torque, such as an increased AC resistance in the windings due to eddy-current phenomena, are not taken into account. Consequently, $\hat{T}_e$ does not only represent the electromagnetic torque, but it also includes other phenomena that affect the phase voltages of the machine. Another possible reason to why the torque estimations change is that the alignment of the dq-axes current reference frame can change depending on the speed and the rotational direction. Such a change can occur with e.g. an insufficient demodulation, and would affect the torque in deep field-weakening operation since a misalignment there primarily affects the q-axis current. However, it is difficult to investigate if a change in the alignment of the reference system actually occurs, and due to the complex phenomena that can affect the relationship between the speed and the electromagnetic torque, the author refrains from giving a definitive theory on the reason behind the results.

2. The estimations become so noisy at high q-axis currents that it is not possible estimate the loss torque in a useful way. Both machines have a top magnitude of acceleration of around 189 rad/s^2 when the current combinations that yield the highest torque are applied (Figures 3.13d and 3.13h). This magnitude of acceleration results in high oscillations, especially at lower speeds. The measurements can still be used to derive useful estimates of $\hat{P}_{loss,,mg}$ with (3.5). Nevertheless, it is clear that high accelerations introduce oscillations also in the $\hat{P}_{loss,,mg}$ estimations when the torque is high (Figures 3.12a and 3.12b). In either case, the noisy results indicate that the moment of inertia of the rotating parts of the machine should be increased to estimate the speed-dependent losses from the loss torque over the whole torque range.

Regardless of the limitations of the loss torque measurements, the results can be used to analyse the losses qualitatively. Figure 3.14 shows the loss torque as a function of the speed for different current combinations. An increase in the q-axis current (Figures 3.14a and 3.14b) yields a higher incline of the loss torque with speed. According to theory this implies an increase of the classical eddy current losses. The increase is expected since the amplitude of the fundamental component of the magnetic flux increases with the current.

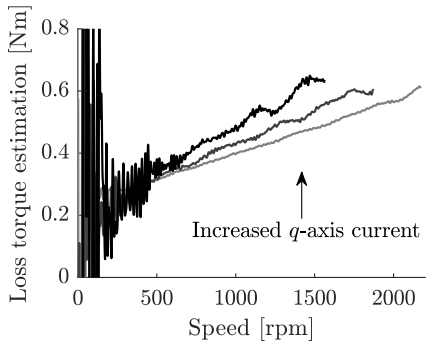

(a) Machine 1 $i_d^s = 0$ A, i_q^s increases from 10 to 30 A in steps of 10 A.

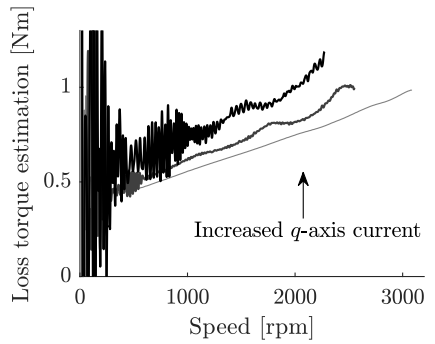

(b) Machine 2 $i_d^s = 0$ A, i_q^s increases from 10 to 70 A in steps of 30 A.

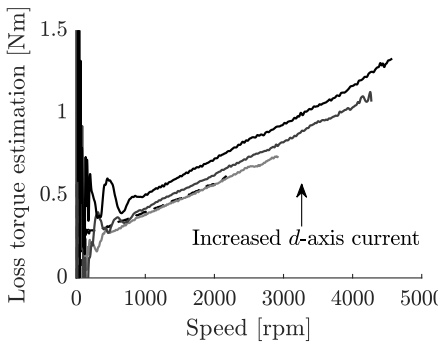

(c) Machine 1 $i_q^s = 10$ A, i_d^s increases from 0 to -60 A in steps of -20 A.

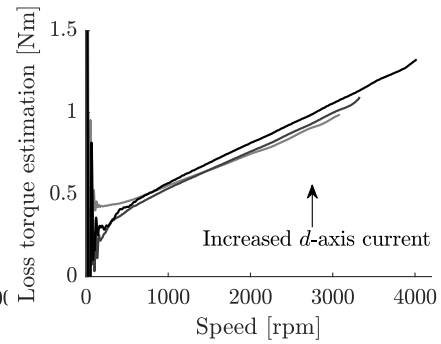

(d) Machine 2 $i_q^s = 10$ A, i_d^s increases from 0 to -80 A in steps of -40 A.

Figure 3.14: Analysis of $\hat{T}_{loss}$ increasing d- and q-axis currents.

However, the constant braking torque increases only marginally with the q-axis current – this is especially true for **machine 1** (fig 3.14a). Considering the fundamental component of the linked magnetic flux, the small increase is surprising since the hysteresis loss generally relates to the flux density squared in iron loss models. One possible explanation to these results is that there exists a big component in the constant braking torque that does not relate to the hysteresis loss (e.g. mechanical braking torque due to bad bearings). If the mechanical loss torque component is significant, it can be difficult to draw a conclusion regarding how much the total loss torque actually does increase when the linked magnetic flux increases. The trend of how the losses change with the d-axis current is not as clear as for the q-axis current (Figures 3.14c and 3.14d). This is not surprising since field-weakening currents introduce a lot of harmonics in the flux density of the machine, which makes it complicated to predict the losses. Both the incline and the offset increase when the d-axis

current increase, which implies an increase in both classical eddy currents and hysteresis losses. Possible explanations to these results are discussed in section 3.6.3.

In addition to analysing the estimations of the loss torque as a function of the speed, the speed-dependent power loss estimation results, $\hat{P}_{loss,sd}$ from (3.8), can be compared to the results from the $\hat{P}_{loss,mg}$ estimations. Figure 3.15a shows the comparison for a current combination that yields a relatively small torque ($i_d^s = -40$ A and $i_q^s = 20$ A). In addition, Figure 3.15b shows the difference between the $\hat{P}_{loss,sd}$ and the $\hat{P}_{loss,mg}$ estimations.

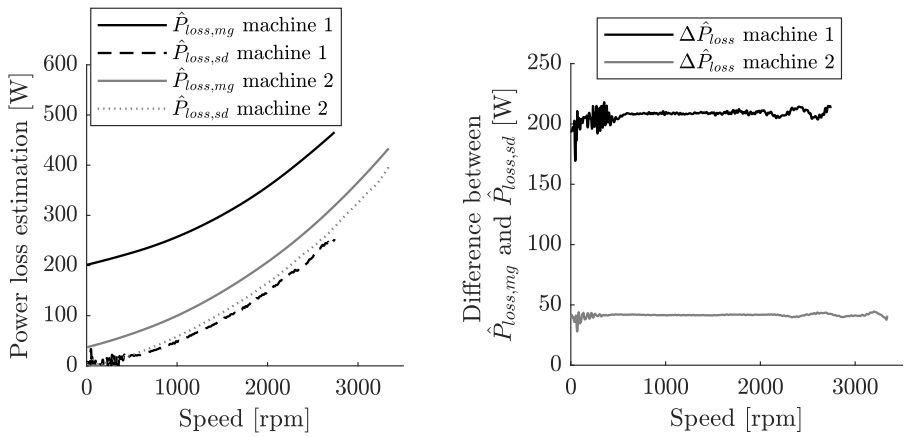

(a) Power loss estimations.

(b) Difference between power loss estimations.

Figure 3.15: Comparison between $\hat{P}_{loss,mg}$ and $\hat{P}_{loss,sd}$ estimations ($i_d^s = -40$ A, $i_q^s = 20$ A).

As expected, the calculations for each individual machine yield similar speed-dependent loss results, and the difference between the $\hat{P}_{loss,sd}$ and $\hat{P}_{loss,mg}$ calculations is approximately constant if oscillations and noise are disregarded. Calculations of the resistive losses according to (3.15) yields $P_R = 210$ [W] and $P_R = 42.9$ [W] for **machine 1** and **machine 2**, respectively (the measured resistance of the windings are given in Appendix A). The calculated powers correspond approximately to the derived quasi-constant estimations in 3.15b, which points towards accurate results.

Another point that must be addressed is the oscillations in the loss torque estimations that occur when the mechanical torque increases (see Figure 3.14a and Figure 3.14b). The oscillations may arise due to many different phenomena. However, since the spline fit approach, which is used for filtering the position, potentially adds noise to the signals (see chapter 2, section 2.3.3 for a more elaborated discussion regarding the filtering of the position measurements), the oscillations can also be due to the data post-processing. This underlines the importance of being attentive when analysing estimations that have been derived from pro-

cessed measurements. In this case, the oscillations are disregarded since they do not yield any explicit useful information to the analysis.

3.6.5 Sensitivity analysis

As discussed in section 3.3, the $\hat{P}_{loss,mg}$ estimations are resilient to measurement errors since data from both generator and motor operation are used in the loss estimation. To evaluate this statement, this section presents a sensitivity analysis where the value of the voltage measurements and the moment of inertia on the rotor axis change, whereupon the impact of the changes on the power estimation are evaluated. Errors in the current measurements are not considered since they affect the electrical power estimations in a similar way as errors in the voltages.

Figure 3.16 illustrates the outcome when the scaling factor of the DC-link voltage and the value of the moment of inertia are changed one percent (for **machine 1**).

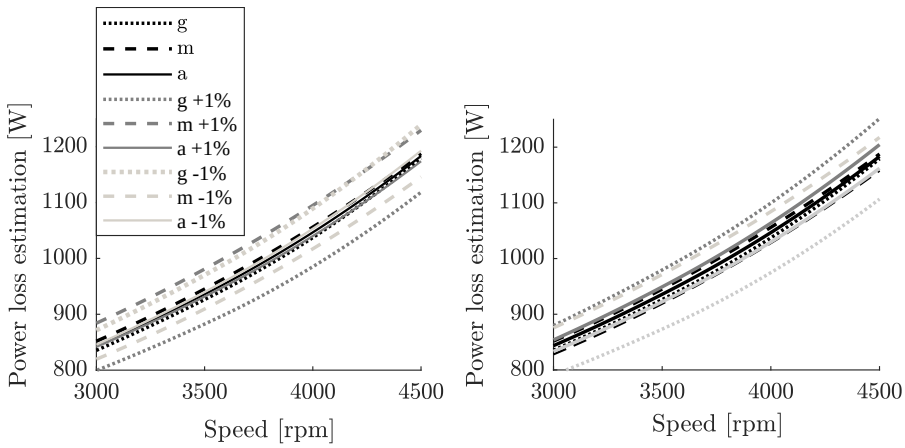

(a) Changes of the DC-link voltage scaling factor.

(b) Changes of the moment of inertia.

Figure 3.16: Influence of voltage and moment of inertia measurements; g stands for generator operation, m motor operation, and the a an average of the two.

The power when the parameters have increased and decreased are included in the figure. The evaluated operating point is i_d^s = -70 A and i_q^s = 10 A since this current combination is found to be most sensitive to errors in the parameters (the operating point yields the worse torque to current ratio, which means relatively small changes in the input parameters have a big impact on the relative errors).

Table 3.2 shows numerical values of the impact of changes in the gain of the voltages and in the moment of inertia. The table presents six parameters: number one and two are $\Delta\hat{P}_{abs}$ and $\Delta\hat{P}_{rel}$, which are the maximum absolute and relative difference between the results with and without an erroneous parameter, receptively.

Table 3.2: Impact of error in measurement parameters.

i_d^s/i_q^s [A]	$\Delta\hat{P}_{abs}$ [W]	BIAS$_{abs}$ [W]	η_{abs} [W]	$\Delta\hat{P}_{rel}$ [%]	BIAS$_{rel}$ [%]	η_{rel} [%]
$1.01 \cdot v_{abc}$						
0 /10	0.104	-0.062	0.021	1.01	0.240	0.274
-70/10	9.79	0.359	2.34	1.02	0.482	0.274
0 /50	2.61	-2.59	0.023	0.996	0.900	0.059
-70/50	-7.57	-6.60	0.615	0.998	0.778	0.130
$1.01 \cdot J$						
0 /10	-1.40	-0.585	0.409	0.949	0.798	0.239
-70/10	-21.8	-8.11	6.29	1.80	0.907	0.543
0 /50	-0.619	-0.279	0.18	0.194	0.095	0.059
-70/50	-4.41	-1.96	1.28	0.445	0.219	0.131

The differences are given by

$$\Delta\hat{P}_{abs} = \quad \hat{P}_{loss,mg} - \hat{P}^e_{loss,mg} \tag{3.59}$$

$$\Delta\hat{P}_{rel} = \quad 200 \left| \frac{\Delta\hat{P}_{abs}}{(\hat{P}_{loss,mg} + \hat{P}^e_{loss,mg})} \right| \tag{3.60}$$

where $\hat{P}_{loss,mg}$ and $\hat{P}^e_{loss,mg}$ are the power estimates without and with an erroneous gain, respectively. The four remaining parameter are the absolute and relative bias (BIAS$_{abs}$ and BIAS$_{rel}$) and standard deviations (η_{abs} and η_{rel}).

Changes in the DC-link voltage scaling factor

When the scaling factor of the DC-link voltage measurements is too high (see Figure 3.16a), the calculation underestimates the power losses in generator operation, but overestimates them in motor operation. However, an average of the two gives similar results as the original estimation without the error in the scaling factor of the DC-link voltage. A decreased gain yields similar results but opposite relationship between the sign of error and generator/motor operation. The behaviour is expected since a higher DC-link voltage scaling factor results in a higher electrical power, which means a lesser difference between the mechanical and electrical power in generator operation, but a greater difference when the machine operates as a motor.

It is difficult to identify a clear relationship between the DC-link voltage scaling factor and the losses (see table 3.2). However, there seems to be a bigger bias when the q-axis current increases; a higher q-axis current leads to higher mechanical dynamics, which in turn can lead to more noise in the voltage measurements.

Changes in the moment of inertia

When the estimated value of the moment of inertia increases (see Figure 3.16b), the difference between the mechanical and electrical power becomes greater in generator operation but lesser in motor operation (and vice versa when the moment of inertia decreases). However, the average value between the motor operation and generator operation when the moment of inertia estimation increases overestimates the losses slightly compared the average without any parameter change. Furthermore, the difference increases with speed. This is due to the difference in shaft torque when the machine works as motor and generator if the dq-axes currents are held constant; the higher the original torque, the higher the absolute change in the torque does a change in the moment of inertia inflict. Therefore, an increase or decrease in the moment of inertia value used in the estimations affect the mechanical power more when the machine brakes than when it accelerates. This phenomenon becomes more apparent with higher losses, but also if the electromagnetic torque changes with speed, which is clearly the case for this operating point (see Figure 3.13b).

The impact that a change of the moment of inertia has on the loss estimations is quite clear (see table 3.2). The current combination $i_d^s =$ -70 A and i_q^s = 10 A is by far the most sensitive to a change in the moment of inertia. As explained before, this is due to a relatively low average shaft torque but a relatively big difference between the torque in the generator and the motor operation (Figure 3.13b). The second worse operating point (of the four analysed points) in terms of absolute errors is the current combination $i_d^s =$ -70 A and $i_q^s =$ 50 A. However, the worse operating point results in an error that is more than four times as big as the second worse.

Conclusion of sensitivity analysis

The general conclusion from the sensitivity analysis is that an average between the motor and generator operation gives results that are less sensitive to errors in the input parameters compared to if only measurements from the motor or the generator operation are used. Furthermore, an erroneous moment of inertia generally has a greater impact on the results compared to a change in the voltage. The numerical results from table 3.2 show relatively moderate impact on the estimations for the relatively big change of the input parameters.

3.6.6 Loss models

First step

As discussed in section 3.4.2, loss models as functions of the speed for specific current combinations can be derived from both the $\hat{P}_{loss,mg}$ estimations, calculated with (3.5), and the $\hat{T}_{loss}$ estimations, calculated with (3.8)[5]. The loss torque estimations, $\hat{T}_{loss}$, provide an attractive starting point since they give a clear insight into whether the simplification that the speed-dependent losses can be approximated by a constant loss torque and a loss torque that increases linearly with the speed holds (see section 3.4.2 for the motivation of this modelling approach). Based on the results from Figure 3.14 this assumption is considered valid for the machines analysed in this work, within the analysed speed range. The model based on the $\hat{P}_{loss,mg}$ (based on (3.37), see section 3.4.2) estimations include the speed-independent losses, and it therefore models the whole loss profile of the machine. Consequently, it is more useful in other contexts, such as in thermal models. Figure 3.17 shows the $\hat{P}_{loss,mg}$ estimations from Figure 3.12a together with their resulting models.

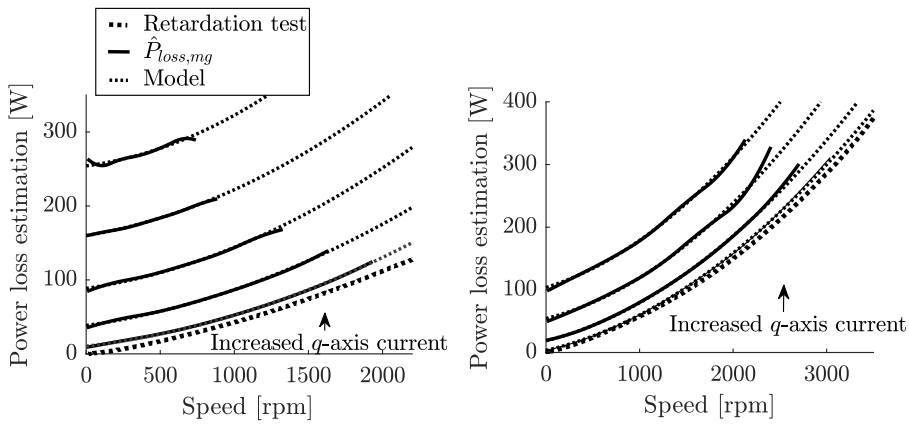

(a) Machine 1 i_q^s increases from 10 to 50 A in steps of 10 A.

(b) Machine 2 i_q^s increases from 20 to 80 A in steps of 20 A.

Figure 3.17: $\hat{P}_{loss,mg}$ estimations together with the resulting models. The same graphs without the model results can be found in Figure 3.12.

A good first step in the validation procedure of the models is to investigate how well the model constants for the $\hat{T}_{loss}$ (equation (3.32)) and the $\hat{P}_{loss,mg}$ models (equation (3.34)) agree. Figures 3.18a and 3.18c show the constants $\hat{k}_h$ and $\hat{k}_c$, estimated with least-square minimisation according to (3.33), for a set of dq current combinations. The constants match

[5]The header "First step" means individual models for each current combinations, as explained section 3.4.2.

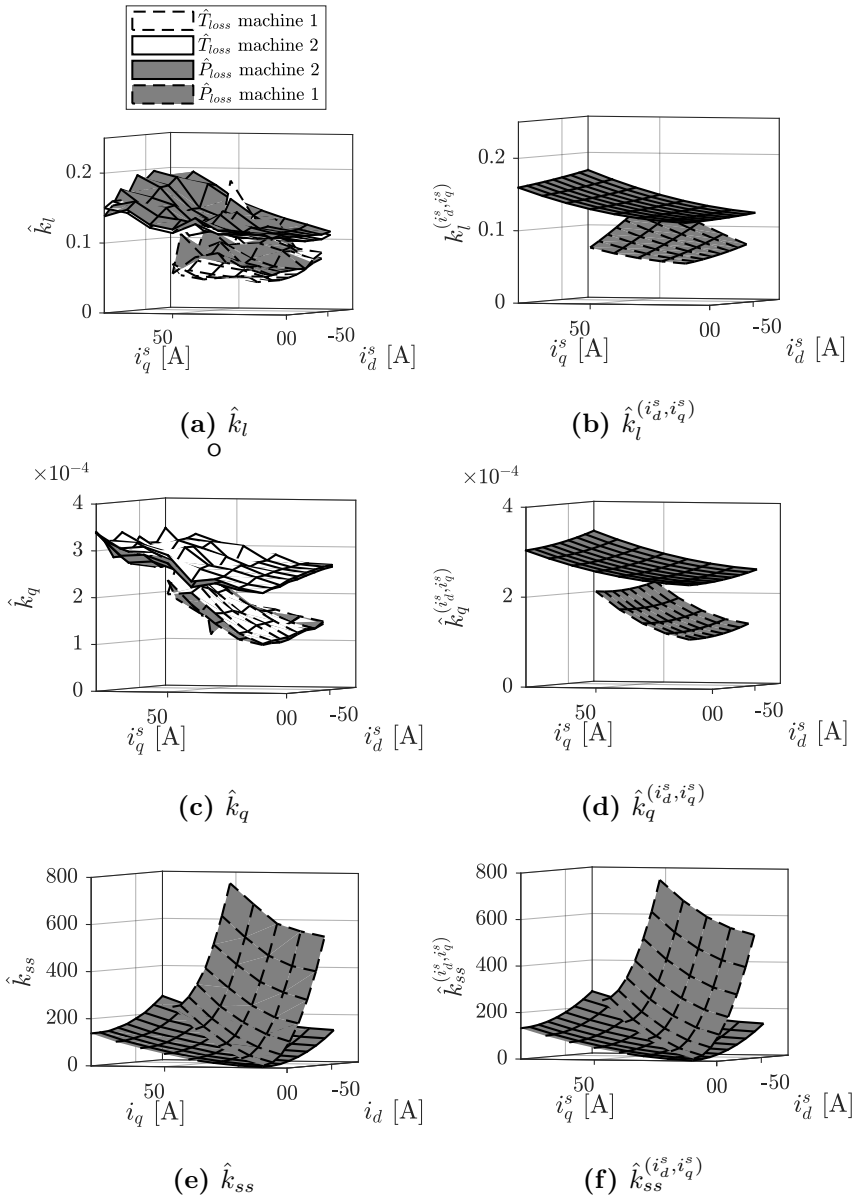

(a) $\hat{k}_l$ **(b)** $\hat{k}_l^{(i_d^s,i_q^s)}$

(c) $\hat{k}_q$ **(d)** $\hat{k}_q^{(i_d^s,i_q^s)}$

(e) $\hat{k}_{ss}$ **(f)** $\hat{k}_{ss}^{(i_d^s,i_q^s)}$

Figure 3.18: Loss model coefficients from $\hat{T}_{loss}$ (3.32) and $\hat{P}_{loss}$ (3.34) estimations. Figures (a), (c) and (e) show the constants from the individual models (the constants in equations (3.32) and (3.34)), while Figures (b), (d) and (f) show the resulting surfaces from the models of the constants (results from equations (3.38), (3.40) and (3.42)).

fairly well, though $\hat{k}_h$ is generally higher in the model from the $\hat{P}_{loss,mg}$ estimations, while the opposite is true for $\hat{k}_c$. The results can be interpreted as the $\hat{P}_{loss,mg}$ model supposes a little bit higher hysteresis losses and smaller classical eddy-current losses compared to the $\hat{T}_{loss}$ model. However, the results agree well enough to be considered good and consistent within the tested range of current combinations.

Figure 3.18e show the obtained constants that represent the standstill losses estimatied by the least-square minimisation of (3.34). Naturally, only the $\hat{P}_{loss,mg}$ models yield these constants since the loss torque does not give any information about the losses when the machines do not move. The results are very similar to the estimated losses due to the DC phase resistance. In other words, the values of the constants can be interpreted as the dissipated heat in the windings due to resistive losses that is independent of the speed.

Second step

The second step of modelling process creates models of the constants from the first step: Equations (3.38), (3.40) and (3.42) are used to model $\hat{k}_\Omega$, $\hat{k}_h$ and $\hat{k}_c$ as functions of the dq-axes currents. Consequently, the resulting models estimate the loss model constants as functions of the currents, whereupon the constants are used in (3.34) to estimate the losses as functions of the angular velocity. Figures 3.18b and 3.18d show constants derived from (3.40) and (3.42) with least-square minimisation according to (3.33) using the estimated constants from the first modelling step presented in the foregoing section. The models of the second machine yields higher $\hat{k}_c$ and $\hat{k}_h$, which results in higher losses using (3.34), than the first machine (see Figures 3.18b and 3.18d). This is expected since **machine 2** is rated for a significantly higher power than **machine 1** (see Appendix A). On the other hand, the modelled loss constants $\hat{k}_c$ and $\hat{k}_h$ of **machine 1** increase more with the q-axis currents compared to **machine 2**. The difference in current dependency is also expected since the first machine features significantly higher inductances than the second, which means that the flux density, and therefore also the losses, increase faster with the currents. The estimated constants from the model also increase with a negative d-axis current. As explained in the preceding sections, this can be because of complex flux distribution in the machine when the field from the magnets and the d-axis currents interact, and/or because of eddy currents that arise when the magnets are subjected to an external field that alternates due to time and space harmonics.

Figure 3.18f shows the model of the constant $\hat{k}_\Omega$, derived by least-square minimisation of (3.38) using the values of $\hat{k}_\Omega$ derived in the first modelling step (see Figure 3.18e). The match is very similar which implies that (3.38) gives an accurate estimation of the speed-independent losses of the machine.

Model validation

Model validation can be performed in many ways, but this analysis focuses on the model results that diverge most from the estimations[6]. Firstly, some fundamental parameters are derived: The mean and maximum deviation between the estimations of $\hat{P}_{loss,mg}$ derived with (3.5) and of the model results (derived from least-square minimisation of (3.38),(3.40) and (3.42) together with (3.34)) in both absolute and relative terms. The absolute deviations considering all operating points and available speeds become:

$$\Delta P_{max} = 39.2 \text{ [W]}$$
$$\Delta P_{mean} = 3.79 \text{ [W]}$$

where the maximum deviations occur in the operating point $i_q^s = 20$ A, $i_d^s =$ -80 A. In relative terms, the maximum and mean deviation are

$$\Delta P_{max} = 16.1 \text{ [\%]}$$
$$\Delta P_{mean} = 1.38 \text{ [\%]}$$

In this case, the maximum deviation occurs for the current combination $i_q^s = 20$ A, $i_d^s = 0$ A. Figure 3.19 shows comparisons between the two operating points that feature the worst match between power loss from the model (3.34) and the $\hat{P}_{loss,mg}$ estimations from (3.5). The significant maximum relative difference in $i_q^s = 20$, $i_d^s = 0$ (Figure 3.19a) is due to an oscillation in the estimations at zero speed. This is considered a minor issue since the absolute value of the deviation is low. The trend for the model from (3.34) and the estimation from (3.5) are similar in the operating point $i_q^s = 20$, $i_d^s =$ -80 (Figure 3.19b). However, one should be careful to note if the derivative of the losses start to deviate at high speeds (even though this is not obvious in this case). If the trend deviates, an extrapolation of the losses versus speed with (3.34) can quickly lead to a significant erroneous estimation. In either case, considering that Figure 3.19 shows results from the operation points where the model deviates the most from the estimations from the prior can be said to give an accurate picture of how the losses evolve with the currents and the speed.

[6]This section only shows results from **machine 1**, but the same analysis for **machine 2** yields similar results (with a bit more discrepancy due to the oscillations in estimations). Furthermore, only the model based on the $\hat{P}_{loss,mg}$ estimations is considered since it represents the whole loss profile of the machine.

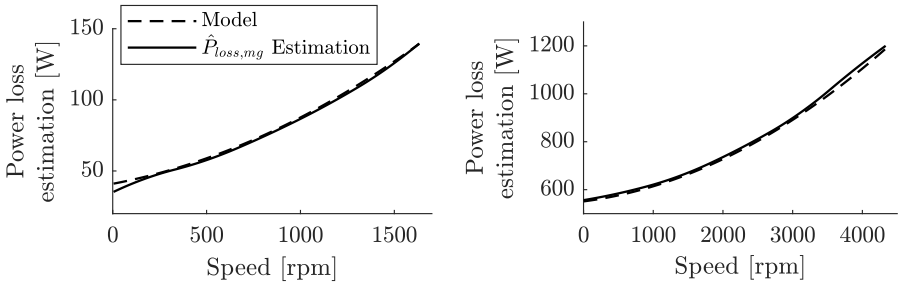

(a) Comparison between the model and the estimation for the current combination that yields the greatest relative difference between the two ($i_q^s = 20$ A, $i_d^s = 0$ A).

(b) Comparison between the model and the estimation for the current combination that yields the greatest absolute difference between the two ($i_q^s = 20$ A, $i_d^s =$-80 A).

Figure 3.19: Comparison between the model and estimations of $\hat{P}_{loss,mg}$ for the operating points that yield the greatest relative and absolute difference.

3.6.7 Comparison to FEM simulations

It is difficult to obtain accurate estimations of speed-dependent losses from finite-element method (FEM) simulations since phenomena such as power losses due to manufacturing (mostly due to damaged varnish by the edges and joining processes of the laminations [92]) are challenging to model. Furthermore, most FEM models simulate the machines in 2D since 3D models generally demand a significant simulation time. In addition, effects due to the characteristics of power converters and current controllers are excluded if the models are excited with sinusoidal currents. Therefore, it is common to adjust the FEM models with experimental measurements of the power losses after testing. On the other hand, experimental measurements that deviate unrealistically much from the uncalibrated simulation results point towards errors in the measurement procedure. Considering this, comparisons between the estimations based on experimental data and results from finite-element method simulations are relevant in this context. Figure 3.20 shows a comparison between calibrated FEM simulation results compared with $\hat{P}_{loss,mg}$ power loss estimations. The FEM simulation models that derived the results in this section are presented in Appendix B, and the calibration strategies are described below.

It is possible to compensate for the manufacturing's influence on the losses by multiplying the FEM simulation loss results with a factor, often referred to as the building factor. This is of course a significant simplification, but suffices for the scope of this work. The estimated compensated losses become

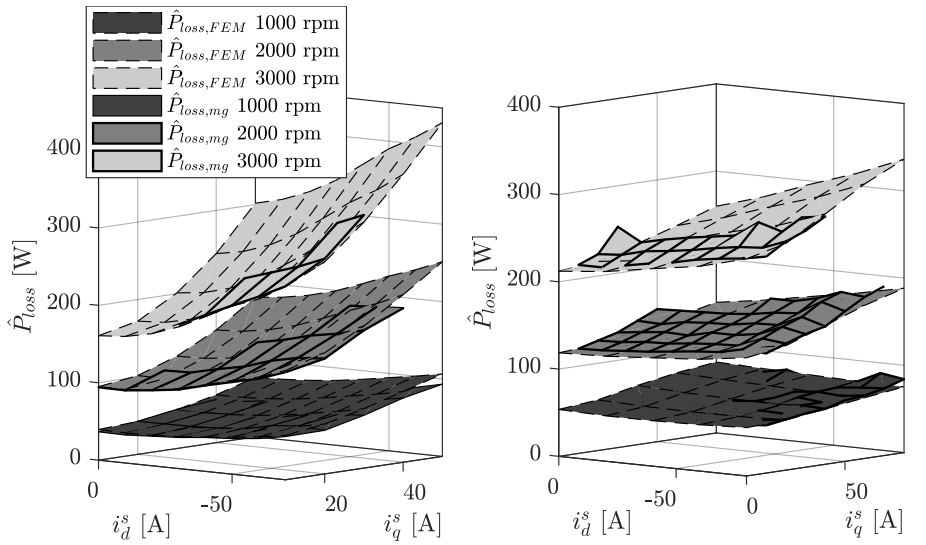

(a) machine 1 **(b) machine 2**

Figure 3.20: Measurements vs. FEM simulations using (3.54) and (3.55) for additional loss compensation for **machine 1** and **machine 2**, respectively.

$$\hat{P}_{loss,FEM_1} = P_{loss,FEM_1} \cdot \chi_1 \tag{3.61}$$

$$\hat{P}_{loss,FEM_2} = P_{loss,FEM_2} \cdot \chi_2 \tag{3.62}$$

where the scaling factors are derived empirically based on the measurements. For **machine 1** the scaling factor becomes $\chi_1 = 2.5$, and for **machine 2** it becomes $\chi_2 = 1.5$. Since the machines are laser cut and welded, these values are within a realistic range [92].

The aforementioned compensations do not make the results from the estimations from (3.5) and the simulations match completely. The most noteworthy differences arise when the d-axis current reaches a great negative value: The loss estimations from the measurements increase significantly more when the d-axis current increases compared to the simulation results. Since the magnetic flux profiles of the core and the permanent magnets become complicated in field-weakening operation, it is difficult to deduce the origin of the additional losses. However, the most probable reason for the increased losses is that eddy currents arise due to harmonics in the magnetic flux. Therefore, the difference between the experimental estimations and the simulation results are considered to be proportional to the square of the frequency. The new expressions for the compensated losses become

$$\hat{P}_{loss,FEM_1} = P_{loss,FEM_1} \cdot \chi_1 + \chi_{d1}(i_d) \cdot \omega^2 \tag{3.63}$$

$$\hat{P}_{loss,FEM_2} = P_{loss,FEM_2} \cdot \chi_2 + \chi_{d2}(i_d) \cdot \omega^2 \tag{3.64}$$

where ω is the electrical angular velocity, index 1 stands for machine 1 and index 2 stands for machine 2. Comparisons show that the additional losses increase fast with the d-axis current at low currents, but flattens out and remain constant once a sufficiently high field-weakening current is reached. Vectors that compensate well for the additional losses due to the d-axis current are presented table 3.3.

Table 3.3: Compensation factor for FEM simulations.

i_d^s [A]	-10	-20	-30	-40	-50	-60	-70	-80
χ_{d1} ($\cdot 10^{-4}$)	1.5	3	4.5	6	7	7	7	-
χ_{d2} ($\cdot 10^{-4}$)	-	1.65	-	3.3	-	4.4	-	5.5

Since the inductance is higher in **machine 1** compared to **machine 2**, the higher loss/current ratio is expected.

Another part of the speed-dependent losses that the FEM simulations do not take into account are the mechanical losses. These losses are often assumed to be small enough to be negligible. However, whether this is an accurate assumption or not clearly depends on the preconditions of the machines under test and the speed range of the tests. In this case, the test speeds are so low that the losses due to windage in the air gap are neglected. The bearing losses are, on the other hand, considered. This is especially relevant for **machine 1** that had been driven with high mechanical dynamics for a long time without bearing maintenance prior to testing.

As shown in section 3.4.1, the relationship between the losses in the bearings and the speed is complicated. Nevertheless, the losses can be approximated to increase linearly with the speed. Considering this simplification, an additional loss term is added to the loss calculations. Investigations show that this additional compensation is redundant for **machine 2**. For **machine 1**, however, the compensation for the mechanical losses is set to 0.07 times the angular velocity, which is a significant part of the speed-independent torque of the machine. This compensation yields a good match between the simulations and the measurements, but whether it is realistic that the bearings have such a big influence on the losses can be discussed. The final expressions for the losses of **machine 1** is formulated as

$$\hat{P}_{loss,FEM_1} = P_{loss,FEM_1} \cdot \chi_1 + \chi_{d1}(i_d) \cdot \omega^2 + \chi_b \cdot |\omega| \tag{3.65}$$

3.6.8 Comparison to constant speed tests

Figure 3.21 shows a comparison between the $\hat{P}_{loss,mg}$ estimations, calculated with (3.5), together with constant-speed tests using the input-output method and estimations of the resistive losses derived from (3.15) for **machine 2**[7].

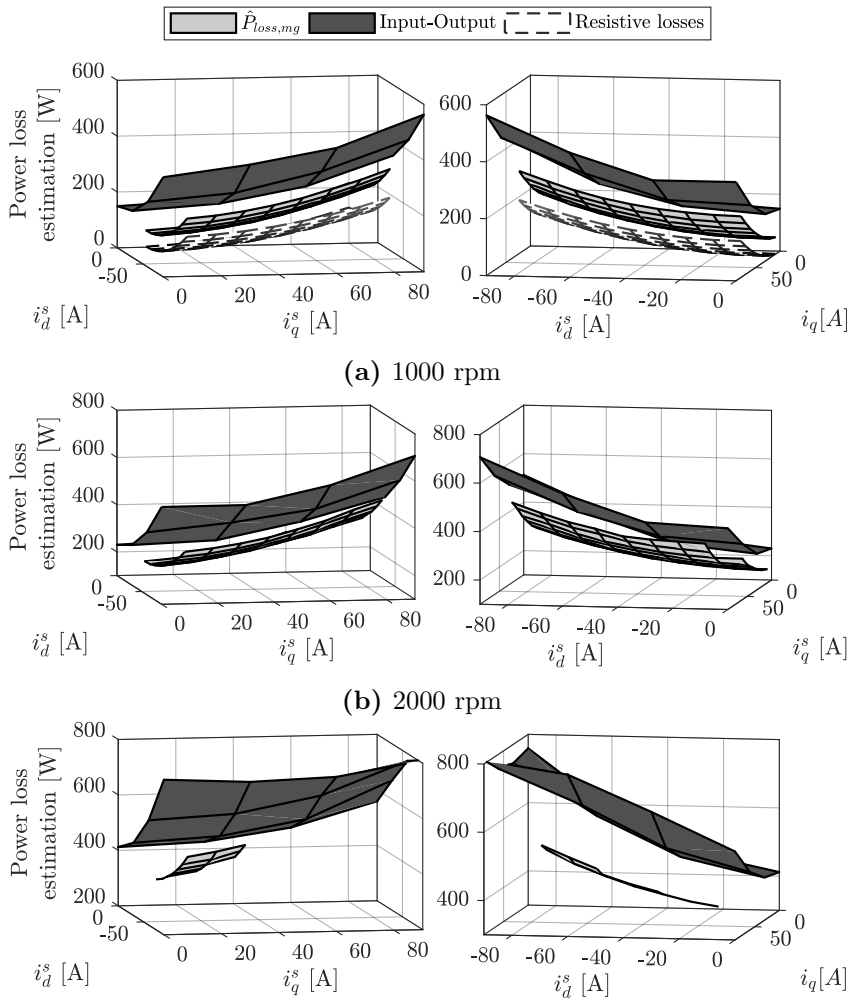

(a) 1000 rpm

(b) 2000 rpm

(c) 3000 rpm

Figure 3.21: Comparison between input-output measurements, $\hat{P}_{loss,mg}$ and estimated resistive losses. Notice the different scales on the Power loss estimation axis.

[7]The input-output tests were, as described in section 3.6.1, performed in facilities of AB Volvo with a different drive system.

There is a power loss offset between the $\hat{P}_{loss,mg}$ estimations and the input-output measurement results for each speed. Notice that the power loss estimation axis in the figure changes to make a closer analysis of the difference between the input-output measurements and the $\hat{P}_{loss,mg}$ estimations possible. However, this can make it seem like the difference is significantly greater at 3000 rpm (Figure 3.21c) rpm compared to 2000 rpm (Figure 3.21b), which it in actuality is not. In either way, the offset can be explained partly by the significantly higher DC link voltage in the input-output test setup, and partly by the difference in current control strategy, the converter and the switching frequency. However, regardless of the possible explanations, the offset is still much higher than expected. Unfortunately, the standstill losses were not measured with the input-output test setup, and it is therefore difficult to draw a final conclusions regarding how the measurements compare to the estimated resistive losses. However, if the constant speed input-output loss measurement results are extrapolated to zero speed, the results are between 50 and 100 Watts higher than the resistive loss calculations.

Despite the offset difference, the results agree quite well in terms of the speed dependency of the losses. This is further visualised in Figure 3.22, which shows a comparison between the $\hat{P}_{loss,mg}$ model from (3.34) together with (3.38), (3.40) and (3.42), and the measurements from the input-output method for four different dq current combinations. The offsets between the model results and the measurements are approximately constant up until 5000 rpm, where the model yields higher loss estimations. However, the trend of the conventional loss measurements is highly unexpected since the derivative of the losses against speed decreases when the speed reaches 5000/6000 rpm (Figure 3.22). This points towards measurement errors since (theoretically) the losses always increase more than linearly with the speed.

3.7 Summary

This chapter gives an in-depth picture of the power loss characteristics of two traction IPMSMs, and shows how measurements from accelerations and retardations can be used to analyse the losses. The $\hat{P}_{loss,mg}$ loss calculations, derived by (3.5), give estimations of the total losses losses in the machines. Since the machines are evaluated continuously over the whole speed range, the results give a direct, qualitative and complete picture of the loss characteristics. Furthermore, the results can be used quantitatively for modelling purposes. In addition, the loss torque analysis gives feedback on how the losses evolves with the speed, which in turn indicates which phenomena that dominate in the total loss profile. However, there are still challenging aspects of the procedures that must be considered. Below follows a discussion about the problems of the methods, and possible solutions to them.

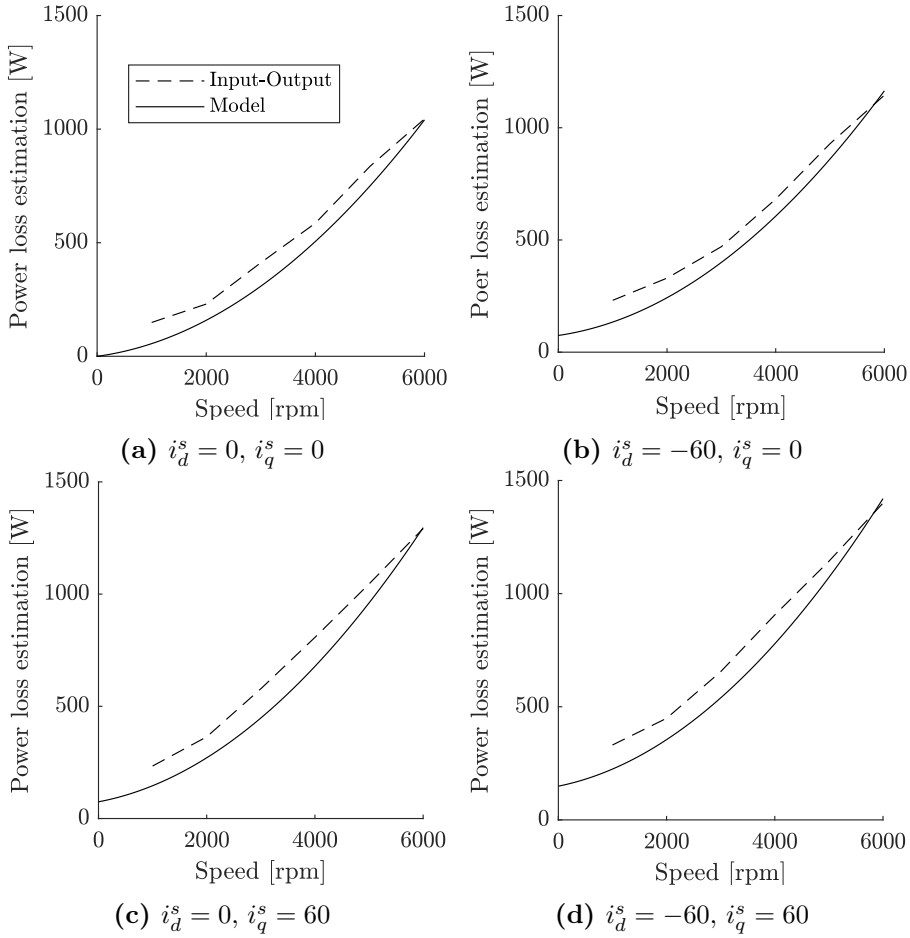

(a) $i_d^s = 0$, $i_q^s = 0$ **(b)** $i_d^s = -60$, $i_q^s = 0$

(c) $i_d^s = 0$, $i_q^s = 60$ **(d)** $i_d^s = -60$, $i_q^s = 60$

Figure 3.22: Comparison between loss model results and conventional measurements for four different current combinations.

Limitations and solutions

As the preceding sections show, $\hat{P}_{loss,mg}$ and $\hat{P}_{loss,sd}$ loss estimations from the dynamic measurements, calculated by (3.5) and (3.8), give good insights into the performance of a machine. In addition, the results are robust to measurement errors and agree well with theory. However, there are some points that must be addressed: In this work, the evaluated test range is limited. This is mainly due to 1) constraints in the voltage and current supply, and 2) safety issues due to the rotating mass. Furthermore, the moment of inertia of the rotating mass must be higher for higher torque ratings, which would result in even more kinetic energy in the rotating mass, and consequently more severe safety issues. Because of these limitations, the test setup should be modified to include higher speeds and torques in

the tests by matching the electrical power source to the needs, and by securing the flywheel with a sufficient mechanical safety installation.

An additional big challenge of the dynamic test method is to obtain uncertainty estimations of the results, which are important for standardised test procedures. It is especially challenging to derive the uncertainty for the mechanical power estimations since the speed and acceleration are the first and second derivative of the position, respectively. It is possible that these issues can be more or less resolved with different measurement and post-processing procedures. However, as is mentioned many times in this thesis, the dynamic method is not primarily intended for benchmarking tests. Instead, it should be seen as an approach to analyse, understand and model the loss characteristics of a machine relatively quickly and with relatively small means. Indeed, conventional measurements cannot provide as informative data sets without a very prolonged testing time, but, on the other hand, they produce results with low and quantifiable uncertainty. Therefore, the two methods are excellent complements to each other; one excels where the other one suffers.

Chapter 4

Thermal characterisation and modelling

4.1 Introduction

Thermal modelling of machines designed to occasionally operate with currents higher than what the windings can sustain indefinitely attracts a lot of attention from designers, manufacturers and users today. This is mainly because 1) the temperature limits how much current the windings can sustain without damage, and 2) permanent magnets can degrade or even demagnetise with too high temperatures. Consequently, good models can predict how cooling approaches of a machine affect its performance in terms of maximum torque and power. As in the case of the electromagnetic models of electrical machines, the thermal models can be divided into two main categories: numerical models (finite element models together with computational fluid dynamics simulations), and equivalent circuits. The numerical models are primarily used in the design phase of a machine, or during in-depth analyses of the spatial temperature distribution. However, due to difficulties in predicting e.g. the thermal conductivity in the insulation of the winding, and to find suitable meshes for the computational fluid dynamics (CFD) simulations, lumped-parameter equivalent circuits often perform almost as well as the numerical methods, even though they are significantly less demanding in terms of computational power. In addition, the parameters of the equivalent circuit can be calibrated relatively straight forwardly with experimental data if the model is designed in the right way. Therefore, this work focuses on a thermal equivalent circuit, which is designed based on the thermal sensors that are integrated into the test object of this work.

The equivalent circuit approach describes the thermal behaviour of a machine with a limited

set of lumped parameters. The circuits are similar to the electrical counterparts, where the temperature replaces the voltage, the rate of heat transfer the current, and the thermal resistance and capacitance the electrical resistance and capacitance, respectively. However, since the conductive path of the heat is much less unified compared to a conductor for an electrical current, the design of the thermal equivalent circuit is less intuitive than the electrical. In addition, the heat paths of a modelled machine include compositions of different materials and fluids (e.g. coolant fluids that acts as model boundaries and air in the air gap between the rotor and the stator). Consequently, the lumped parameters of the thermal circuits are generally complicated and difficult to estimate accurately with only analytical equations.

Since this chapter focuses mainly on modelling it introduces terminology from system identification theory to describe the equivalent thermal circuit. A model where pure analytical calculations estimate the parameters is defined as a white-box model, whereas models where experimental feed-back helps with the parametrisation are called grey-box models. Since lumped parameters can be difficult to estimates accurately with only analytic equations, many lumped-parameter models are calibrated with experiments. Consequently, these models can be labelled as grey-box models. It is possible to divide the experimentally calibrated thermal models into two categories: The first one identifies the components of the model individually, while the second category identifies optimal parameters of the model globally through some kind of optimisation procedure. Since the purpose of this thesis is to find methods to evaluate machines that are already assembled the focus lies on the second category.

The grey-box models of the aforementioned second category that can be found in the litterature either include the whole loss behaviour and operational range of the machines, or focus on the windings since they are prone to experience quick thermal transients. However, models that include the whole loss behaviour generally demand detailed knowledge about the loss characteristics of the test objects before the identification of the thermal properties begin [93–96]. The aforecited literature measures and estimates the losses with a conventional test setup, which includes a power analyser and a torque sensor[1]. Consequently, the modelling procedure becomes time consuming and the test setup becomes costly. On the other hand, most methods that estimate the temperature of the winding either includes only one step response, or many tests, to derive the thermal characteristics of the temperature evolution of the windings [97–101]. As a consequence, the model derivation procedures either work with little information about the overload characteristics of the machine, or demand prolonged testing procedures. Considering the requirements and limitations above, the goal of this chapter is to propose a modelling methodology that 1) require as little test equipment – which includes power supply, sensors, mechanical setups and so forth – as possible, and 2) only needs one test to derive the thermal behaviour of

[1]See chapter 3, section 3.2 for a description of a conventional test setup for loss estimation

the machine with the full current range. To achieve these goals, models that predict the thermal behaviour at standstill and low-speed operation are considered. Due to the scope of the model, the speed-dependent losses are not included, and they consequently do not have to be measured and characterised in the initialisation of the modelling. It should be said that the continuing ambition is to include the loss models from the previous chapter into the thermal equivalent circuits. However, due to time restrictions speed-dependent losses are not yet included, and the proposed models of this chapter consequently give a lot of room for future work. The list below describes the content of the chapter

4.2 **Thermal lumped-parameter models** gives an introduction to the lumped-parameter equivalent circuit approach to thermal modelling of machines. The section describes the physical meanings behind the components of the circuit to give the reader an understanding of the difficulties in estimating the models analytically. Furthermore, the section gives a brief introduction to the white-, grey- and black-box model concepts, and explains why the experimentally calibrated lumped-parameter circuit is a typical grey-box model.

4.3 **Test object and modelling procedure** describes the thermal modelling approach of this work. The modelling is based on the thermal sensors of the test object and of two cooling circuits: an oil circuit that cools the machine, and a water circuit that regulates the temperature of the oil. The section emphasises the importance to approach each machine design separately – especially if the cooling strategies differ. Two models are proposed: one that makes use of all the available sensors, and one that only includes the sensors that are normally available in a manufactured machine. In addition, the section describes the process of deriving good model parameters, including initial parameter estimations and calibration of the parameters with experimental data.

4.4 **Experimental procedure, setup and results** describes the setup of the experiments, together with the motivation behind the input current sequences for the identification and the validation, and the control for the two coolant circuits. Furthermore, parameter results from the identification, together with results from a thorough validation procedure are presented.

4.5 **Summary** summarises the results and discusses limitations and future work.

4.2 Thermal models of electrical machines

The most common approaches to model the thermal behaviour of electrical machines are based on either lumped-parameter models or finite-element method (FEM) models, which

are often coupled to electromagnetic simulations[2]. Since this thesis focus first and foremost on experimental work, simple lumped-parameter circuits, where the parameters can be found straight forwardly with grey-box modelling, are considered. Therefore, theory of FEM and CFD analyses are left out, and the machine modelling focuses only on lumped-parameter circuits. More information regarding FEM and CFD for thermal modelling can be found in [102].

The thermal lumped-parameter circuits are similar to their electrical counterparts, where temperatures replace voltages (or potentials), rate of heat transfers replace the currents, thermal resistances the electrical resistances, and the heat capacities of the different parts of the machine the electrical capacitors [103]. The analysed object is typically divided into several segments, where the nodes of the circuit represent the centres of each parts. Figure 4.1 shows an example of a simple thermal circuit design of an electrical machine stator in two dimensions.

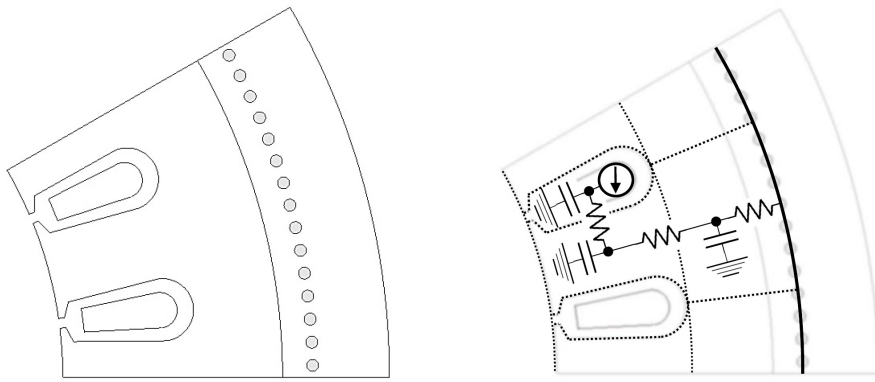

(a) Machine model without circuit. **(b)** Machine model with circuit.

Figure 4.1: Example of a lumped-parameter thermal circuit of a machine stator.

The stator is in this example divided up in three main parts: The slot, the stator teeth, and the stator yoke together with the lower part of the machine housing. The cooling channels (the small circles in Figure 4.1) act as a boundary condition in the circuit. Since the machine is symmetrical, the model in Figure 4.1b yields a representation of the whole machine in two dimensions. The following sections present a short introduction to the components of a lumped-parameter thermal circuit.

[2]Many of the available softwares provide solution for combining electromagnetic and thermal finite element simulations in an easy manner [102]. Furthermore, computational fluid dynamics (CFD) is used to simulate the heat transfer characteristics between the machine and different fluids (typically coolants).

Thermal resistances

Thermal resistances describe the steady-state relationship between the temperature and the rate of heat transfer. Three different phenomena control this relationship: thermal conduction, convection and radiation [104]. Radiation is often neglected in modelling electrical machines, and this section therefore focuses on conduction and convection. The conduction type of thermal resistance is based on Fourier's law of heat conduction that relates the temperature gradient to the rate of heat transfer in a medium where no bulk movements are involved. Mathematically the relationship can be formulated as

$$\dot{Q}_{\text{cond}} = -\lambda A \frac{d\zeta}{dx} \tag{4.1}$$

where $\dot{Q}_{\text{cond}}$ is the rate of heat transfer, $\frac{d\zeta}{dx}$ is the temperature gradient, A is the area and λ is the thermal conductivity of the conductive path. If the rate of heat transfer is constant over a certain distance x in the conductive path, (4.1) can be rewritten to

$$\dot{Q}_{\text{cond}} = \lambda A \frac{\zeta_1 - \zeta_2}{x} \tag{4.2}$$

Since the rate of heat transfer and the temperature represent the current and the voltage in the electrical counterpart, it makes sense to rewrite (4.2) to

$$\dot{Q}_{\text{cond}} = \frac{\zeta_1 - \zeta_2}{\mathcal{R}_{\text{cond}}} \tag{4.3}$$

where

$$\mathcal{R}_{\text{cond}} = \frac{x}{A \cdot \lambda} \tag{4.4}$$

In the circuit in Figure 4.1 A is the mean area, x is the distance, and λ is the average conductivity of the materials between the nodes. There are some parts of the machine where the equivalent resistances are difficult to estimate: Especially the conductivites of the radial parts of the winding, the interface between the slot and the stator teeth, and the crossing between the stator yoke and the housing are challenging due their arbitrary nature [105,106]. As a consequence, the literature presents many empirical studies on the conductivities of these parts. The equivalent thermal resistance between the winding and the tooth depends on various parameters such as the fill factor of the winding and the goodness factor of the insulation, and therefore varies from machine to machine – this is especially true for pulled

windings that have a stochastic conductor distribution in the slots [107, 108]. Therefore, experimental tests for calibration of the estimated equivalent thermal resistance between the winding and the teeth are next to mandatory for good thermal models. In addition, the interface between the laminates of the stator and the machine housing tends to be uneven, and the equivalent thermal resistance is therefore difficult to estimate [105, 109].

Equivalent thermal resistances of the convection type describes the relationship between the rate of heat transfer and the temperature difference between a solid surface and a fluid in motion. In most cases the term convection heat transfer coefficient, defined as "the rate of heat transfer between a solid surface and a fluid per unit surface area per unit temperature difference" [110], is used to described this relationship. Mathematically it is formulated as

$$h = \frac{\dot{Q}_{\text{conv}}}{A(\zeta_1 - \zeta_2)} \tag{4.5}$$

Since the relationship between the rate of heat transfer and the temperature difference does not (explicitly) depend on a distance x, it cannot be related to a equivalent electrical resistance in a physical sense. However, the heat transfer coefficient can easily be rewritten to relate the rate of heat transfer and temperature as a resistance

$$\mathcal{R}_{\text{conv}} = \frac{1}{hA} \tag{4.6}$$

Convection phenomena can be separated into two basic types: the forced convection and the natural convection. As the names imply, forced convection arises when a fluid is forced upon a solid surface, and natural convection when the fluid motion occurs due to natural means. Both types are used to cool machines; however, electrical machines for traction, which have a significant need for efficient cooling at high currents and speeds, are usually cooled with forced convection that yields a much higher heat transfer coefficient compared to natural convection. When forced convection cools the machine through e.g. water, oil or air cooling, the natural convection generally has a small impact on the overall cooling performance of the machine.

To express the characteristics of the relationship between the rate of heat transfer and the temperature during forced convection, a dimensionless heat transfer coefficient, also called the Nusselt number, is often used [104, 110]. The Nusselt number is a function of the Reynolds and Prandtl numbers, which in turn are functions of the velocity of the flow, the kinematic velocity, specific heat, and thermal diffusivity of the fluid. If there is an estimation of the Nusselt number (Nu) available, the heat transfer coefficient between the fluid and the wall can be calculated as

$$h = Nu \cdot \frac{\lambda}{L} \tag{4.7}$$

where λ is the thermal conductivity of the fluid and L is the characteristic length, which varies with the geometry of the cooling channel. For a laminar flow the Nusselt number can be found for common geometries, but when the flow turns turbulent it is almost impossible to obtain the heat transfer coefficient without experiments or detailed 3D CFD simulations.

Thermal capacitances

The capacitances of the thermal circuit describe the heat mass of the segments and are derived by

$$C = \rho V C_p \tag{4.8}$$

where ρ is the average density of the body, V is the body's volume and C_p is the average specific heat capacity. The thermal resistance together with the thermal capacitance yield the thermal time constant of the body and consequently describe the transient behaviour of the body's temperature. Most thermal capacitances of a machine are quite straight forward to derive if the geometry and materials are known. However, the thermal capacitances of the windings are challenging since they depend on properties that are difficult to predict in the practical realisation and production (e.g. insulation goodness factor). Furthermore, the distribution of conductors between the end-winding and the active winding is quite random and difficult to estimate in a pulled-winding machine. As a consequence, experimental tests are often performed to derive the specific heat capacity of winding segments [107, 108].

Heat sources

The heat sources in thermal lumped-parameter circuits represent heat dissipated from power losses in the machine. The models of the power loss generation in IPMSMs are described in chapter 3.

4.2.1 System modelling; the grey-box approach

The term "grey-box modelling" is used later in this chapter when the procedure of deriving the parameters of the lumped-parameter model is discussed, and a brief introduction to system modelling in general, and grey-box modelling in particular, is therefore in place. In

the litterature, models of physical systems are generally divided into three categories: the black-box model, the white-box model and the grey-box model [111].

- **The black-box** model does not take any physical aspects of the system into account and is purely based on the input and the output measurements. Consequently, it is an arbitrary transfer function that gives similar outputs as the modelled system for a given input. The black-box model can simulate an arbitrary system well, but it does not give any information regarding its actual physical properties, and can therefore not give information that can be reused in a redesign of the system (in this case an electrical machine). Furthermore, since the model does not relate to physics, a detailed validation becomes very important due to the risk that the model only performs sufficiently for the identification data.

- **The white-box** approach models a system purely based on physical models. White-box models are typically used when predicting the temperature in the design phase of a machine; both FEM models and lumped-parameter models can be considered to be white-box models. Since the white-box models do not use any experimental data (at least not in a strict sense [111]), parameters that are difficult to predict can distort the outcoming results of the models significantly. As discussed in the previous section, the thermal resistance between the winding and the stator core, and the contact resistances between the winding and the stator teeth and the stator yoke and the housing are especially challenging to determine. Furthermore, if the machine is cooled actively, the prediction of the heat transfer at the interface between the machine and the coolant demands sophisticated fluid dynamic simulations for good estimations.

- **The grey-box** models are based on both experimental measurements and physical models, and considering electrical machines they can be divided up into two categories. The first type, which can be considered a light grey-box or a white-box model with experimental feedback, bases some or all of its parameters on individual measurements. The different parameters, e.g. the equivalent thermal resistance and capacitance of the winding and the airgap, are derived individually, and the model is then put together as a pure white-box model. The second type identifies the model parameters globally through an optimisation algorithm; this is the approach that is proposed in this work. The model parameters are usually initially guesstimated by analytical calculations, whereupon they are refined to fit the available data. Therefore, the model does not necessarily correspond directly to physics, even though its foundation relates to a white-box model. Challenges lie in finding a model with enough parameters to represent the measurements well, but at the same time limit the number of parameters to avoid falling into local minima or divergence in the optimisation process. Therefore, thermal lumped-parameter grey-box models of the

second kind generally contain significantly less nodes than the corresponding white-box models.

4.3 Thermal modelling of this thesis

As mentioned in the introduction, the models of this thesis aim to predict the temperatures in different parts of a machine when it operates at low speed or when it stands still. Two models are proposed:

1. The first model, which is called the full-order model, is derived from measurements from all available thermal sensors in the machine. These are positioned in the end-winding, in the active winding, at the outmost laminate of the stator teeth and yoke, on top of the housing of the machine, and in the inlet and the outlet of the coolant circuit. The model yields a good representation of the nature of the thermal behaviour of the machine and has potential to include speed-dependent losses (this is discussed more in the conclusion of this chapter). However, in a real application, it is more likely that the machine only feature a sensor where the hotspot likely occurs.
2. The second model, which is a reduced-order model, focuses on predicting the hotspot temperature of the machine. The reduced-order model assumes that a sensor in the end-winding, a sensor mounted on top of the housing, and two sensors in the oil coolant circuit are available.

4.3.1 Test object and coolant circuit

The first step of the thermal model design process analyses the physical design and the coolant characteristics of the machine. Here, **machine 1** from Appendix A acts as the modelling object. The machine is designed to operate over a wide speed and torque range, and sometimes with currents that cannot be sustained indefinitely without causing damage to the machine. Figure 4.2 shows a sketch of the machine and the cooling circuit. The circles with crosses in the figure represent the thermal sensors that are installed in/on the machine and in the coolant circuit. The housing of the machine features cooling channels for liquid oil. As mentioned above, PT100 sensors are mounted in the end-winding overhang (not included in Figure 4.2), in the active winding inside the slots (2 in Figure 4.2), at the outmost laminate of the stator teeth and yoke (3 and 4 in Figure 4.2), and on top of the housing of the machine (5 in Figure 4.2). Furthermore, a cooling circuit that circulates oil through the cooling channels of the machine's housing is included in the test setup. PT100 sensors are mounted on the inlet and outlet of the machine house (6 in Figure 4.2), and the temperature of the coolant can therefore be included in the thermal model. The oil circuit

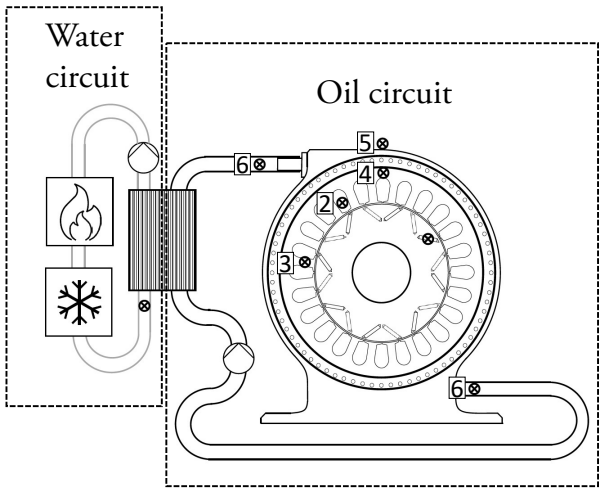

Figure 4.2: Sketch of the test object with the oil coolant circuit, heat exchanger and the water coolant circuit. The black circles with crosses represent the thermal sensors, where the numbers are different nodes in the equivalent circuit. The numbering starts at 2) since the end-winding sensor is excluded from the figure.

is thermally connected to a temperature controlled water circuit through a heat-exchanger. Therefore, it is possible to use the temperature of the water circuit as a boundary condition for the model. The sensors define the nodes in the model that the next coming section presents. Note that both the inlet and outlet sensors in the oil circuit have the number 6 in Figure 4.2. This is because the corresponding node temperature is the average of the measurements from the two.

Four basic assumptions that simplifies the model are considered based on the previously described system:

1. **All the heat is transferred through the active coolant in the housing.** This assumption holds sufficiently for the analysed machine since there is no end-winding cooling, since the thermal resistance between the rotor and the stator is so high that the thermal dynamics of the rotor affect the temperature in the stator marginally, and since the natural convection to the surrounding air is relatively small compared to the forced convection to the coolant. However, with an active cooling of the end-windings and/or the rotor the heat flow pattern becomes more complex, and tests must be performed to investigate if similar assumptions hold. Furthermore, the expectation that the natural convection is so small that it can be neglected cannot be taken for granted, and if the model does not suffice as a representation of the thermal

behaviour of the machine, this assumption should be revised. The model does however behave acceptable in this study, and the approximation is therefore considered sufficient.

2. **The thermal resistances and capacitances of the machine do not change with temperature.** This is not completely true since the thermal conductivity and the specific heat capacity of the materials change slightly with a varying temperature [112, 113]. However, the change is considered small enough to not have a significant impact on the temperature characteristics of the machine within the considered operating temperature range (the model is validated for temperatures from 60^{o}C to 150^{o}C). However, if the temperature range of the model is extended significantly, it can be necessary to include varying parameters in the model. Parameter varying systems are out the scope of this work, but [95] discuss how this can be implemented extensively for the interested reader.

3. **The losses in the windings are the only significant sources of rate of heat transfer**. Copper losses dominate the heat dissipation in the machine at standstill and low-speed operation, and the assumption is therefore sufficient in this context. It is difficult to specify at which speed the speed-dependent losses, which primarily arise in the electrical steel of the stator, start to affect the temperature of the machine significantly. Nevertheless, validation of the model of this work show that the assumption holds for a rotating speed of 500 rpm.

4. **The dynamics of the water circuit in the heat exchanger are so slow that the water temperature can be considered to be constant.** This assumption holds well and makes it possible to introduce the temperature of the water as a boundary condition in the model.

4.3.2 The full-order model design

As mentioned above, the full-order lumped-parameter circuit is built on all the PT100 sensors that are mounted in the windings, on the stator, on top of the housing of the machine and in the coolant circuit. The aforementioned assumptions yield a lumped-parameter circuit as depicted in Figure 4.3. The nodes represent the end-winding, the winding, the teeth, the yoke, the housing and the coolant. Furthermore, the temperature of the water in the heat-exchanger circuit acts as a boundary node of the model. The order of the model is determined by the number of nodes that contain dynamic elements (the thermal capacitances), and is consequently six. The rates of heat transfer into the winding and end-winding nodes of the circuit simulates the losses that arise when the windings are excited with a current.

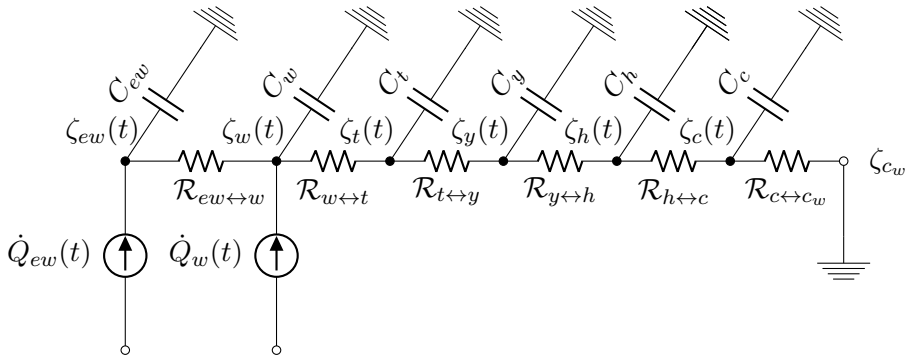

Figure 4.3: Lumped-parameter model of the test object.

State-space model for identification

The goal of the grey-box modelling is to find parameter values so that the equivalent circuit of Figure 4.3 emulates the thermal behaviour of the machine as accurately as possible. To achieve this, the first step is to represent the lumped-parameter circuit mathematically as a state-space model. The state-space model is structured as

$$\begin{aligned} \dot{\chi}(t) &= \mathbf{A}\chi(t) + \mathbf{B}u(t) \\ y(t) &= \mathbf{C}\chi(t) \end{aligned} \tag{4.9}$$

where $u(t)$ contains the inputs to the system, $\chi(t)$ the state variables and $y(t)$ the outputs. The input vector consists of the electrical currents, the winding resistance and the temperatures of the winding and end-winding nodes in Figure 4.3 (this is discussed further down). The state variable vector consists of the node temperatures, and the output vector is the same as the state variable vector (i.e. $\mathbf{C}$ is the identity matrix). Mathematically, $u(t)$ and $\chi(t)$ are formulated as

$$u(t) = \begin{pmatrix} R_{\circ} i(t)^2 \\ (\zeta_{ew}(t) - \zeta_{c_w}) R_{\circ} i(t)^2 \\ (\zeta_w(t) - \zeta_{c_w}) R_{\circ} i(t)^2 \\ 0 \\ 0 \\ 0 \end{pmatrix}, \quad \chi(t) = \begin{pmatrix} \zeta_{ew}(t) \\ \zeta_w(t) \\ \zeta_t(t) \\ \zeta_y(t) \\ \zeta_h(t) \\ \zeta_c(t) \end{pmatrix} \tag{4.10}$$

where $R_{\circ}$ is the resistance of the winding when it has the same temperature as the water. The first element of the input vector consequently describes the rate of heat transfer when the

temperature of the winding is the same as the temperature of the water, while the second and the third elements take the temperature's impact on the heat dissipation due to the change of the resistivity of the windings into consideration. In a wye-connected three-phase machine, $i(t)$ is $\sqrt{i_d^2 + i_q^2}$ and R_{o} is the phase resistance R_s supposing a power-invariant dq transformation. However, the machine must rotate to have an evenly distributed heat generation when the machine is wye connected, and the thermal model can therefore not be derived with tests when the machine stands still. To overcome this, the three phases of the machine are connected in series, and the resulting electrical impedance is excited with a time varying DC current. With the new connection, the same current flows through all windings, and the heat generation is therefore evenly distributed in all the slots. The resistance of the new connection, i.e. R_{o} in (4.10), is equal to $3R_s$, and $i(t)$ in (4.10) becomes the time varying DC current. Section 4.4 explains the setup further.

As seen in (4.10), the input vector $u(t)$ contains the state variables ζ_{ew} and ζ_w. This is necessary due to the temperature dependence of the resistance of the windings, which affects the losses, and therefore the rate of heat transfer, significantly. The connection between the state variables and the input imposes a feedback on the system, which out of a simulation and control perspective is problematic. However, since this system is designed for identification purposes, and all the state variables are measured during the experiments, this does not cause a problem at this stage. The following section describes how the system can be redesigned for simulation purposes.

The Kirchoff's voltage equations of the equivalent circuit yield the matrix **A** as

$$\mathbf{A} = \begin{pmatrix} -\frac{1}{\tau_{ew}} & \frac{1}{\tau_{ew}} & 0 & 0 & 0 & 0 \\ \frac{1}{\tau_{w1}} & -\left(\frac{1}{\tau_{w2}} + \frac{1}{\tau_{w1}}\right) & \frac{1}{\tau_{w2}} & 0 & 0 & 0 \\ 0 & \frac{1}{\tau_{t1}} & -\left(\frac{1}{\tau_{t2}} + \frac{1}{\tau_{t1}}\right) & \frac{1}{\tau_{t2}} & 0 & 0 \\ 0 & 0 & \frac{1}{\tau_{y1}} & -\left(\frac{1}{\tau_{y2}} + \frac{1}{\tau_{y1}}\right) & \frac{1}{\tau_{y2}} & 0 \\ 0 & 0 & 0 & \frac{1}{\tau_{h1}} & -\left(\frac{1}{\tau_{h2}} + \frac{1}{\tau_{h1}}\right) & \frac{1}{\tau_{h2}} \\ 0 & 0 & 0 & 0 & \frac{1}{\tau_{c1}} & -\left(\frac{1}{\tau_{c2}} + \frac{1}{\tau_{c1}}\right) \end{pmatrix} \tag{4.11}$$

where τ are the thermal time constants of the system ($\tau_{w1} = C_w \mathcal{R}_{ew \leftrightarrow w}$ and $\tau_{w2} = C_w \mathcal{R}_{w \leftrightarrow t}$ and so forth). The matrix **B** dictates how the inputs affect the state variables and is formulated as

$$\mathbf{B} = \begin{pmatrix} q\frac{1}{C_{ew}} & q\frac{\alpha_{\mathrm{Cu}}}{C_{ew}} & 0 & 0 & 0 & 0 \\ (1-q)\frac{1}{C_w} & 0 & (1-q)\frac{\alpha_{\mathrm{Cu}}}{C_w} & 0 & 0 & 0 \\ 0 & 0 & 0 & 0 & 0 & 0 \\ 0 & 0 & 0 & 0 & 0 & 0 \\ 0 & 0 & 0 & 0 & 0 & 0 \\ 0 & 0 & 0 & 0 & 0 & 0 \end{pmatrix} \tag{4.12}$$

where q divides the total stator resistance R_{s} between the winding and end-winding, and α_{Cu} defines the temperature dependence of the electrical resistance in the model; this factor is generally called the temperature coefficient in the literature. Note that the values in the second and third column of $\mathbf{B}$ relate to the second and third value in $u(t)$. These inputs take the temperature dependence of the heat dissipation in the windings into account. To clarify, the resulting inputs to the end-winding and winding node can be expressed as

$$\dot{Q}_{ew} = \left(R_{\mathrm{s}} i(t)^2 \cdot q\frac{1}{C_{ew}}\right) + \left(R_{\mathrm{s}} i(t)^2 \cdot q\frac{\alpha_{\mathrm{Cu}}}{C_{ew}}\right)(\zeta_{ew}(t) - \zeta_{c_w})$$
$$\dot{Q}_{w} = \left(R_{\mathrm{s}} i(t)^2 \cdot (1-q)\frac{1}{C_{w}}\right) + \left(R_{\mathrm{s}} i(t)^2 \cdot (1-q)\frac{\alpha_{\mathrm{Cu}}}{C_{ew}}\right)(\zeta_{w}(t) - \zeta_{c_w})$$

State-space model for simulation

As mentioned above, the state-space model for identification has an intrinsic feedback since the rate of heat transfer due to the electrical current depends on the temperature of the winding. The feedback creates an algebraic loop if the model is simulated without a delay. Therefore, it makes sense to differentiate the system. Here, the forward euler method is used to approximate the system's dynamics

$$\frac{\chi(n+1) - \chi(n)}{\Delta t} = \mathbf{A}\chi(n) + \mathbf{B}v_1(n)\chi(n) + \mathbf{B}v_2(n) \tag{4.13}$$

where $v_1(n)$ and $v_2(n)$ are given by

$$v_1(n) = \begin{pmatrix} 0 & 0 & 0 & 0 & 0 & 0 \\ R_o i(n)^2 & 0 & 0 & 0 & 0 & 0 \\ 0 & R_o i(n)^2 & 0 & 0 & 0 & 0 \\ 0 & 0 & 0 & 0 & 0 & 0 \\ 0 & 0 & 0 & 0 & 0 & 0 \\ 0 & 0 & 0 & 0 & 0 & 0 \end{pmatrix}, \; v_2(n) = \begin{pmatrix} R_o i(n)^2 \\ -R_o i(n)^2 \zeta_{c_w} \\ -R_o i(n)^2 \zeta_{c_w} \\ 0 \\ 0 \\ 0 \end{pmatrix}$$

and where Δt is the sampling time. This approximation is only sufficient if the noise to signal ratio in the current sensor is low and the time steps are short compared to the system's dynamics; otherwise, the output signal becomes noisy and unstable. In this work, the data was collected with one hertz, which suffices since the temperature dynamics of the machine are relatively slow. Considering Δt =1 [s], (4.13) can be rewritten to

$$\chi(n+1) = (\mathbf{I} + \mathbf{A} + \mathbf{B}v_1(n))\chi(n) + \mathbf{B}v_2(n) \tag{4.14}$$

which is straight forward to implement in code. It should be mentioned that there are more refined ways of simulating state-space systems that derives the results in more accurately [114]. However, in this case (4.14) suffice well.

Analytical estimation of parameters

Even if the design of the grey-box model is based on physics, the optimisation process only minimises the differences between the measured and estimated temperatures without taking any physical aspects of the model into account. Therefore, it is important to have initial estimations of the model parameters that correspond to reality as much as possible (in this case, we suppose that a realistic thermal model predicts the temperatures better). In addition, the analytical estimations should be compared to the final grey-box model parameters to make sure that the results have a reasonable physical interpretation. Some of the parameters are difficult to estimate: The heat transfer coefficients of the interfaces between the cooling channels and the oil in the oil circuit (see Figure 4.2), and the oil and the water through the heat exchanger, involve forced convection and demand extensive CFD simulations or measurements for accurate estimations. Furthermore, the thermal capacitance of the coolant node (the node of the temperature $\zeta_c(t)$ in Figure 4.3) in the model is complicated to estimate if the volume of the coolant is not known. Therefore, these parameters are given arbitrary values, within reasonable limits, in the initiation of the optimisation. However, the rest of the parameters of the model can be estimated more straight forwardly if the design and materials of the machine are known.

Resistances. The thermal resistances $\mathcal{R}_{w\leftrightarrow t}$, $\mathcal{R}_{t\leftrightarrow y}$ and $\mathcal{R}_{y\leftrightarrow h}$ are derived as suggested by Figure 4.1, while the estimation of the resistance $\mathcal{R}_{ew\leftrightarrow w}$ requires information about the axial geometry of the machine. As mentioned in section 4.2, the thermal conductivities of the interfaces between the winding and the teeth, and the yoke and the house, vary from machine to machine and are complicated and difficult to determine. However, the literature presents reasonable values that suffice as first estimations (respective references are given for each parameter below). The following list describes the considered approaches to derive the four resistances

- $\boldsymbol{\mathcal{R}_{w\leftrightarrow t}}$. Various publications state that the heat transfer coefficient between the winding and the teeth depends largely on the conductivity of the epoxy and different fillers that are used during the manufacturing process. Furthermore, the fill factor of the slot and the material of the conductors naturally affect the equivalent thermal conductivity of the windings. Here, the fill factor of the slot is assumed to be 40 % (an arbitrary but common figure), and the conductors are made out of copper. According to the litterature, these preconditions yield an equivalent thermal conductivity between 1.5 and 3 W/(mK) for the winding and insulation in the radial direction [107, 115, 116]. For this work, an equivalent thermal conductivity of $\lambda_{w\leftrightarrow t}$ = 2 W/(m·K) is used, which suffice for the final results of the thermal model estimation. When the interface's equivalent thermal conductivity is known, the tangential length between the middle of a slot and the slot wall, and the total area of all the slot walls, yield the resistance according to (4.4). The numerical values of the aforesaid parameters become

$$\begin{aligned} \lambda_{w\leftrightarrow t} &= 2 && [\mathrm{W/(m \cdot K)}] \\ x_{w\leftrightarrow t} &= 0.0042 && [\mathrm{m}] \\ A_{\text{slot-walls}} &= 0.0460 && [\mathrm{m^2}] \\ \mathcal{R}_{w\leftrightarrow t} &= 0.0454 && [\mathrm{K/W}] \end{aligned}$$

  Note that the part of the core between the winding node and the teeth node is neglected since the thermal conductivity of electrical steel is significantly higher than the radial thermal conductivity of the slot ($\lambda_{\text{E-steel}} \approx 30$ [W/(m · K)]).

- $\boldsymbol{\mathcal{R}_{t\leftrightarrow y}}$. In deriving the resistance between the teeth and the yoke, the mean area (A in (4.4)) is calculated by first deriving the total cross-sectional stator area between the teeth and yoke node (excluding the slot), then dividing it by the distance between the radius of the nodes (x in (4.4)) and finally multiplying the results with the machine length. Mathematically, the calculation of A can be expressed as

$$A_{t\leftrightarrow y} = \frac{l_m}{r_y - r_t} \int_0^{2\pi} \int_{r_t}^{r_y} S(r,\theta) dr d\theta \tag{4.15}$$

where $S(r,\theta)$ is the supposed function for the 2D cross-sectional geometry of the of the stator in polar coordinates, l_m is the machine length, and r_t and r_y are the radiuses to the node in the teeth and the yoke, respectively. When $A_{t\leftrightarrow y}$ and $x_{t\leftrightarrow y}$ are known, the thermal resistance is calculated according to (4.4), where the thermal conductivity of electrical steel $\lambda_{\text{E-steel}}$ is found in [117]. The numerical values of the parameters of the considered machine become

$$\begin{aligned} \lambda_{\text{E-steel}} &= 30 && [\text{W/(m} \cdot \text{K)}] \\ x_{t\leftrightarrow y} &= 0.0259 && [\text{m}] \\ A_{t\leftrightarrow y} &= 0.0276 && [\text{m}^2] \\ \mathcal{R}_{t\leftrightarrow y} &= 0.0218 && [\text{K/W}] \end{aligned}$$

- $\boldsymbol{\mathcal{R}_{y\leftrightarrow h}}$. The resistance between the yoke and the housing is quite arbitrary in its nature since the interface between the laminations of the stator and the relatively even surface of the housing varies from one machine to another, even if the design is the same. However, for a rough estimation it is possible to model the interface as an equivalent small uniform airgap. Here, the calculations of the parameters assume an airgap of $\Delta l_{ag} = 0.07$ mm [105]. The thermal resistances due to the iron and the aluminium are neglected since the thermal conductivity of air is much lower than that of the two metals ($\frac{\lambda_{\text{E-steel}}}{\lambda_{\text{Air}}} \approx 1136$ and $\frac{\lambda_{\text{Al}}}{\lambda_{\text{Air}}} \approx 7765$ [112, 118]). It should be added that if the distances between the nodes and the equivalent air gap are multiple orders of magnitudes longer than Δl_{ag} they can have significance in the total thermal resistance between the nodes regardless of the big difference in thermal conductivity. Nevertheless, the approximation suffice in this context since the parameter estimations are optimised in the grey-box model estimation procedure after the analytical estimations. The numerical results for the parameters that derive the equivalent thermal resistance and its resulting value become

$$\begin{aligned} \lambda_{\text{Air}} &= 0.0264 && [\text{W/(m} \cdot \text{K)}] \\ x_{ag} &= 0.00007 && [\text{m}] \\ A_{ag} &= 0.0592 && [\text{m}^2] \\ \mathcal{R}_{ag} &= 0.045 && [\text{K/W}] \end{aligned}$$

- $\boldsymbol{\mathcal{R}_{ew\leftrightarrow w}}$. The estimation of the resistance between the end-winding and the active winding requires insight in the axial geometry of the machine. Due to the arbitrary

winding distribution of pulled windings, it is difficult to derive an accurate estimation of the actual length between the middle of the end-winding and the active winding. Furthermore, the exact placements of the sensors are not known in this case, which means it is uncertain whether they measure the intended temperatures. Despite the difficulties, one can derive an approximate value of the end-winding-to-winding resistance: A crude estimation considers the end-windings to be perfect half circles in between one slot to the next, and assumes that the end-winding and winding sensors are mounted in the middle of the half circle, and in the middle of the axial length of the machine, respectively. Figure 4.4 shows the diameter of the assumed half circle for the machine that is evaluated in this work.

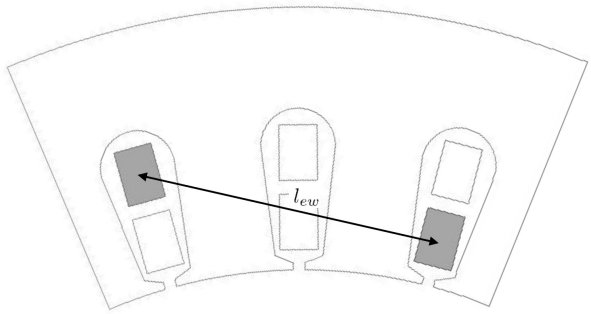

Figure 4.4: Length for end winding estimation.

The estimated length x in (4.4) between the nodes of the end-winding and active winding becomes

$$x_{ew\leftrightarrow w} = \frac{l_{ew}\pi}{4} + \frac{l_m}{2} \tag{4.16}$$

where l_m is the axial length of the machine. The areas of the active winding and the end-winding are considered to be the slot area. Furthermore, the thermal conductivity of the insulation is considered negligible compared to the copper. Therefore, the parameter $A_{ew\leftrightarrow w}$ in (4.4) is estimated by the slot area multiplied by the winding fill factor. The resistance is now derived with (4.4), where the thermal conductivity of copper λ_{Cu} is found in [112]. The numerical results for the parameters that derive the equivalent thermal resistance and its resulting value become

$$\begin{aligned} \lambda_{\text{Cu}} &= 400 && [\text{W}/(\text{m}\cdot\text{K})] \\ x_{ew\leftrightarrow w} &= 0.078 && [\text{m}] \\ A_{ew\leftrightarrow w} &= 0.0017 && [\text{m}^2] \\ \mathcal{R}_{ew\leftrightarrow w} &= 0.112 && [\text{K/W}] \end{aligned}$$

Thermal capacitances. Equation (4.8) gives the thermal capacitances of the equivalent circuit straight forwardly if the materials and geometries of the different parts of the machine are known. Unfortunately, no geometrical data of the housing is available, which means its equivalent thermal capacitance is estimated very roughly in the initialisation of the optimisation. Furthermore, the equivalent thermal capacitance of the node that represent the oil circuit in Figure 4.2 is, as mentioned in the beginning of this section, complicated to derive – especially when the volume of the coolant is not known. Nevertheless, the rest of the thermal capacitances of the equivalent circuit in Figure 4.3 can be derived with the available information:

- $\boldsymbol{C_{ew}}$. The estimation of the thermal capacitance of the end-windings assumes that one end-turn is a perfect halfcircle with the diameter l_{ew} (the same assumption as the estimation of $\mathcal{R}_{ew\leftrightarrow w}$ does, see Figure 4.4). Considering the area of the slot and the end-winding to be the same, the volume of the end-windings become

$$V_{ew} = \frac{l_{ew} A_{slot} \pi}{2} n_{\text{slots}} \tag{4.17}$$

  The windings consist both of copper and of insulation that have significantly different density and specific heat capacity. However, the literature presents typical figures that can be used for the calculations [107, 113]. Considering a fill-factor of 40 %, the density of the winding is approximated to

$$\rho_{wind} = 0.4\rho_{\text{Cu}} + 0.6\rho_{\text{Epoxy}}$$

  Here, an epoxy resin mass density of $\rho_{\text{Epoxy}} = 1200$ [kg/m^3] and a copper mass density of ρ_{Cu}=8890 [kg/m^3] are considered, and an approximate estimation of the equivalent specific heat capacity of the windings $C_{p,wind}$ is obtained from [107]. Considering (4.8), the parameter values of the equivalent thermal capacitance of the windings together with its value become

$$\begin{aligned} \rho_{wind} &= 4276 && [\text{kg/m}^3] \\ C_{p,wind} &= 700 && [\text{J/(kg}^o\text{K)}] \\ V_{ew} &= 2.97 \cdot 10^{-4} && [\text{m}^3] \\ C_{ew} &= 889 && [\text{J/}^o\text{K}] \end{aligned}$$

- $\boldsymbol{C_w}$. The thermal capacitance of the windings inside of the slots is calculated as C_{ew}, with the exception that the volume is the stack length times the slot area and the number of slots

$$V_w = l_m A_{slot} n_{\text{slots}} \tag{4.18}$$

The earlier presented equivalent mass density and specific heat of the windings together with the volume of the windings inside the slots give the equivalent thermal capacitance

$$\begin{aligned} V_w &= 3.84 \cdot 10^{-4} && [\text{m}^3] \\ C_w &= 1150 && [\text{J}/^o\text{K}] \end{aligned}$$

- $\boldsymbol{C_t}$. The volume of the teeth part of the stator can be described as

$$V_t = l_m \int_0^{2\pi} \int_{r_{ti}}^{r_{to}} S_t(r, \theta) dr d\theta \tag{4.19}$$

where r_{ti} and r_{to} are the radiuses of the inner and outer boundaries of the teeth segment, respectively. The density $\rho_{\text{E-steel}}$ and the specific heat capacity $C_{p,\text{E-steel}}$ of electrical steel are found in [117], and the parameters of the equivalent thermal capacitance becomes

$$\begin{aligned} \rho_{\text{E-steel}} &= 7650 && [\text{kg/m}^3] \\ C_{p,\text{E-steel}} &= 490 && [\text{J/(kg}^o\text{K)}] \\ V_t &= 6.37 \cdot 10^{-4} && [\text{m}^3] \\ C_t &= 2387 && [\text{J}/^o\text{K}] \end{aligned}$$

- $\boldsymbol{C_y}$. The calculation of the yoke thermal capacitance is very similar as for C_t, except that the boundaries of the radial integral in (4.19) change:

$$V_y = l_m \int_0^{2\pi} \int_{r_{to}}^{r_{so}} S_t(r, \theta) dr d\theta \tag{4.20}$$

where r_{so} is the outer diameter of the stator (the interface between the stator and the housing). The volume of the stator segment, together with the mass density and specific heat of the electrical steel, give the thermal capacitance according to (4.8)

$$\begin{aligned} V_y &= 7.86 \cdot 10^{-4} && [\text{m}^3] \\ C_y &= 2748 && [\text{J}/^o\text{K}] \end{aligned}$$

Comments

The procedures above describe simplified strategies to derive the passive elements in the equivalent circuit of the full-order model. A more thorough analyses can include e.g. the stacking factor of the stator, a deeper investigation of an appropriate division between capacitances in the machine, inclusion of the iron part in the winding-to-teeth and the yoke-to-house resistance, and calculations of the housing capacitance that is straight forward to achieve if the house geometry can be estimated. However, the analytically derived parameter values suffice in this context since they are later on optimised in the grey-box estimation procedure. All the analytically estimated parameters can be found together in table 4.1 that appears in section 4.4.1.

4.3.3 The reduced-order model

Figure 4.5 shows the reduced-order model, which builds upon the sensors in the end-winding, on the top of the housing, and in the coolant channels.

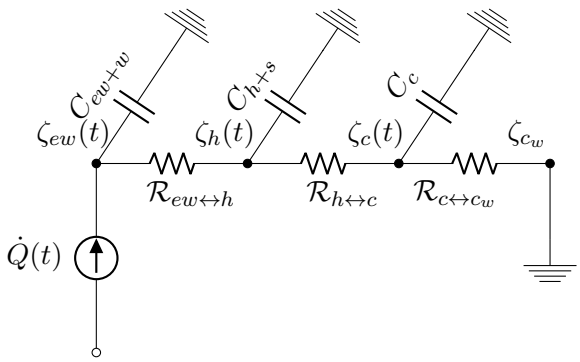

Figure 4.5: Reduced-order lumped-parameter model of the test object.

In this model, the heat dissipation is not divided between the end-winding and the active winding. Instead, all the losses are modelled to arise in the end-winding. The assumption moves the model away from a physical representation of the machine, which in other words makes the model a "darker" grey-box representation compared to the full-order model. The equivalent thermal capacitance of the end-winding node in Figure 4.5 is estimated as the sum of the end-winding capacitance and the winding capacitance from the full-order model, while the node that represents the house temperature has an equivalent thermal capacitance equal to the sum the teeth, the yoke and the housing thermal capacitance. The values of the new thermal capacitances are found in table 4.1 that appears in section 4.4.1. Kirchoff's voltage law yields the state-space matrices of the reduced-order model

$$\mathbf{A} = \begin{pmatrix} -\frac{1}{\tau_{ew}} & \frac{1}{\tau_{ew}} & 0 \\ \frac{1}{\tau_{h1}} & -\left(\frac{1}{\tau_{h2}} + \frac{1}{\tau_{h1}}\right) & \frac{1}{\tau_{h2}} \\ 0 & \frac{1}{\tau_{c1}} & -\left(\frac{1}{\tau_{c2}} + \frac{1}{\tau_{c1}}\right) \end{pmatrix} \tag{4.21}$$

$$\mathbf{B} = \begin{pmatrix} \frac{1}{C_{ew}} & \frac{\alpha}{C_{ew}} & 0 \\ 0 & 0 & 0 \\ 0 & 0 & 0 \end{pmatrix} \tag{4.22}$$

The input vector and state vector become

$$u(t) = \begin{pmatrix} R_o i(t)^2 \\ (\zeta_{ew}(t) - \zeta_{c_w}) R_o i(t)^2 \\ 0 \end{pmatrix}, \; \chi(t) = \begin{pmatrix} \zeta_{ew}(t) \\ \zeta_h(t) \\ \zeta_c(t) \end{pmatrix} \tag{4.23}$$

The state-space model for simulation is formulated in the same way as for the full-order model (section 3.2).

4.3.4 Optimisation procedure

This work does not focus on the mathematical algorithm that optimises the model parameters, but rather on the step-by-step modelling procedure in a broader perspective (the main focus is described further in the introduction and conclusion of this chapter). Therefore, the System Identification Tool-box in Matlab, which features a predefined work package for grey-box model identification, is used [119]. However, a brief introduction to the mathematical concept of the optimisation algorithm is important to understand how the parameter values are derived. Furthermore, there are some practical aspects, such as initialisation of the optimisation, that should be discussed.

Initialisation of optimisation

Before the actual identification procedure starts, it is important to provide the optimisation algorithm with good first estimations of the parameters. The analytical estimations of the parameters that the preceding section presents give a first base for the initial values for the optimisation. However, there are two additional measures that can be considered to get better initial parameter values:

1. A straight forward approach to obtain good estimates of all thermal resistances of the model, except the one between the end-winding and the active winding, is to let the system approach a quasi-steady-state temperature distribution in the end of the identification test sequence. Since all the losses arise in the active winding and end-winding, the rate of heat transfer from the winding node out to the coolant is known. The rate of heat transfer together with the temperature drops between the nodes of the circuit then yield the resistances according to

$$\mathcal{R} = \frac{\zeta_1 - \zeta_2}{\dot{Q}} \tag{4.24}$$

2. Since (4.13) gives a straight forward solution to simulate the model, one can get an understanding of how different parameters affect the temperature distribution by manually changing them slightly and comparing the simulation output results with the measurements. This procedure helps with obtaining suitable initial parameter values for the optimisation algorithm, and it also indicates how the different parameters of the model affect its dynamics.

It should be emphasised that none of these measures require additional tests, but can be performed with the same data that is used for identification supposing that the test sequence ends in a quasi-steady-state temperature distribution.

In addition to good initial parameter values, it may be favourable to reduce the order of freedom of the model by locking parameters that are well known, supposing they are relatively temperature independent[3]. In this case, the temperature coefficient of copper α_{Cu} is locked throughout the optimisation procedure since it has a well-defined value that remains fairly constant in the relevant temperature range [75]. Furthermore, the end-winding node temperature in the full-order model is affected by the end-winding capacitance, the end-winding-to-winding resistance, and the q factor that divides the stator resistance into an end-winding and a winding part. Since an infinite combination of these parameters give the same results (supposing that the winding capacitance can change as well), the optimisation procedure has a high risk of deriving unrealistic parameter values, which can be problematic in e.g. an extension of the model. However, by locking the end-winding-to-winding resistance, the optimisation algorithm is able to derive realistic parameter values that give accurate simulation results.

Concept of optimisation algorithm

Matlab's toolbox for system identification provides a number of different optimisation algorithms that can be used to derive the optimal parameters of the grey-box model. The

[3]Here, "locked parameter" means parameters which values do not change in the optimisation procedure.

algorithms minimise the square of the errors between the measured values and the system outputs by changing the system parameters. The sum of the squares of the errors can be described with the cost function

$$f(\mathbf{x}) = \sum_{i=1}^{m} r_i(\mathbf{x})^{\mathrm{T}} r_i(\mathbf{x}) \tag{4.25}$$

where $\mathbf{x}$ contains the parameters of the system, $r(\mathbf{x})$ the residuals (the difference between the measurements and the model outputs) and m is the number of observations. Ideally, $f(\mathbf{x})$ becomes as close to zero as possible after the optimisation procedure. Most optimisation algorithms that are available in the grey-box work package are based on the Gauss-Newton algorithm, which is a simplification of the Newton's method for optimisation; a variant of this algorithm is also used in this work. These methods try to find parameter values that yield a zero derivative of the cost function without letting its value increase during the search process. Naturally, this function finds the closest local minimum considering the starting values of the parameters, and it is therefore important to choose parameters that finds an as global optimum as possible. The Newton's method with one identifiable variable is formulated as

$$x(k+1) = x(k) - \frac{f'(x,k)}{f''(x,k)} \tag{4.26}$$

where k is the iteration index of the optimisation procedure. Considering $f(x,k)$ to be equal to the cost function (4.25), (4.26) becomes

$$x(k+1) = x(k) - \frac{\sum_{i=1}^{m} r_i \frac{dr_i}{dx(k)}}{\sum_{i=1}^{m} \frac{d^2 r_i}{dx(k)^2}} \tag{4.27}$$

With multiple identifiable variables, the derivative of the cost function with regards to the identifiable parameters is represented by the gradient vector, and the second derivative by the Hessian matrix

$$\mathbf{x}(k+1) = \mathbf{x}(k) - \mathbf{H}^{-1}\mathbf{g} \tag{4.28}$$

where $\mathbf{H}$ is the Hessian matrix and $\mathbf{g}$ is the gradient vector. The gradient vector is a column vector with the same number of elements as number of identifiable parameters in the system. Considering the cost function (4.25), one element of the gradient vector for one specific k is derived as

$$g_j = 2\sum_{i=1}^{m} r_i \frac{\partial r_i}{\partial x_j} \tag{4.29}$$

The complete gradient vector is formulated as

$$\mathbf{g} = 2\mathbf{J}^T\mathbf{r} \tag{4.30}$$

where $\mathbf{J}$ is the Jacobian matrix and $\mathbf{r}$ is a column vector containing the residuals. The Hessian matrix is the derivative of the gradient in regard to the identifiable parameters, and is consequently a square matrix with the same number of rows and columns as the number of identifiable parameters in the system. One element in the Hessian matrix is given by

$$H_{jl} = 2\sum_{i=1}^{m}\left(\frac{\partial r_i}{\partial x_j}\frac{\partial r_i}{\partial x_l} + r_i\frac{\partial^2 r_i}{\partial x_j \partial x_l}\right) \tag{4.31}$$

As seen in (4.31), the Hessian contains both first- and second-order derivatives of the residuals with regards to all parameters. However, the second-order derivatives can be computationally demanding to calculate, and if the system is fairly linear and the residuals are small around the minimum, the second-order derivatives can be approximated to zero; this simplification yields the Gauss-Newton algorithm. Considering the second-order derivatives in the Hessian to be zero, (4.28) can be rewritten to

$$\mathbf{x}(k+1) = \mathbf{x}(k) - (\mathbf{J}^T\mathbf{J})^{-1}\mathbf{J}^T\mathbf{r}(\mathbf{x}(k)) \tag{4.32}$$

which, together with a set criteria when to stop (e.g. maximum iterations reached) yield parameters that minimises the cost function as much as possible. The methods that are available in Matlab's tool-box manipulate the Jacobian and/or the Hessian and set up additional restrictions and rules for the optimisation process to perform more efficient estimations. Furthermore, the algorithms work with subspaces to make the optimisation process more efficient (this is the automatically choosen algorithm in the grey-box identification package, and was used for the optimisation in this work). In addition, other methods, such as the gradient-decent method, which only follows the negative gradient minimise the cost function, and the Levenberg-Marquardt algorithm, which combines Gauss-Newton's with the gradient-decent method, are also available. More information regarding relevant optimisation algorithms can be found in [120].

Comments

In addition to the underlying optimisation algorithm, it is also possible to include an overlaying algorithm that automates the process to find the good initial parameters. One such example is the particle swarm algorithm where different parameter values is located randomly in a search space (within reasonable limits of course), and each of the initial parameter combinations are evaluated to find the best case [121]. In the next iteration the particles move according to certain conditions, and a new optimisation with the underlying algorithm is performed. This approach may help a lot, especially if the numbers of parameters is substantial and there are many parameters that are difficult to estimate analytically.

There are also additional measures one can take to further control the optimisation. The parameters can be limited by bounds so they do not obtain values that deviates from physics (e.g. negative impedances). Furthermore, weights can be put on different outputs if some temperatures are more important than others. In some instances, it can be more important to model the winding temperature accurately compared to the stator yoke temperature. In such cases, higher weights can be put on the residuals from the more important temperatures, which make the optimisation algorithm find parameter values that make the models reflect these temperatures better.

4.4 Experimental procedure, setup and results

One of the main goals of the proposed test method is to avoid conventional converters and a dynamo; the tests should be performed at standstill and at the same time capture as much of the thermal dynamic behaviour of the machine as possible. It is therefore preferable to include the thermal dynamics that arise when the current is significantly higher than what the machine can sustain in a steady-state situation. Furthermore, the current should contain as little harmonics as possible to make sure that the absolute majority of the losses are dissipated in the windings. Considering these aspects, the test setup is assembled as described in the following list

- Both the physical inputs and the outputs of the windings are available in the test object of this work, and they can therefore be connected in series to create one circuit that includes all the conductors of the machine.
- The end points of the circuit are connected to a supply voltage that excites the machine with current. The supply voltage is in this case a three-phase rectifier bridge connected to a transformer rated for high current, which in turn is connected to a variable transformer that can provide voltages between 0 and 230 Volts. Furthermore,

a electrical capacitor is mounted on the output of the bridge to cancel out harmonics. Consequently, an adjustable DC current with small harmonics is created and used as excitation during the experiments.

- To obtain the input power, which is approximately the heat dissipated in the windings, the voltage over the input terminals of the machine is measured directly with two cables that are connected to a differential input in the data acquisition (DAQ) system. The current is obtained by measuring the voltage over a shunt resistor.

Figure 4.6 shows the circuit layout of the test setup.

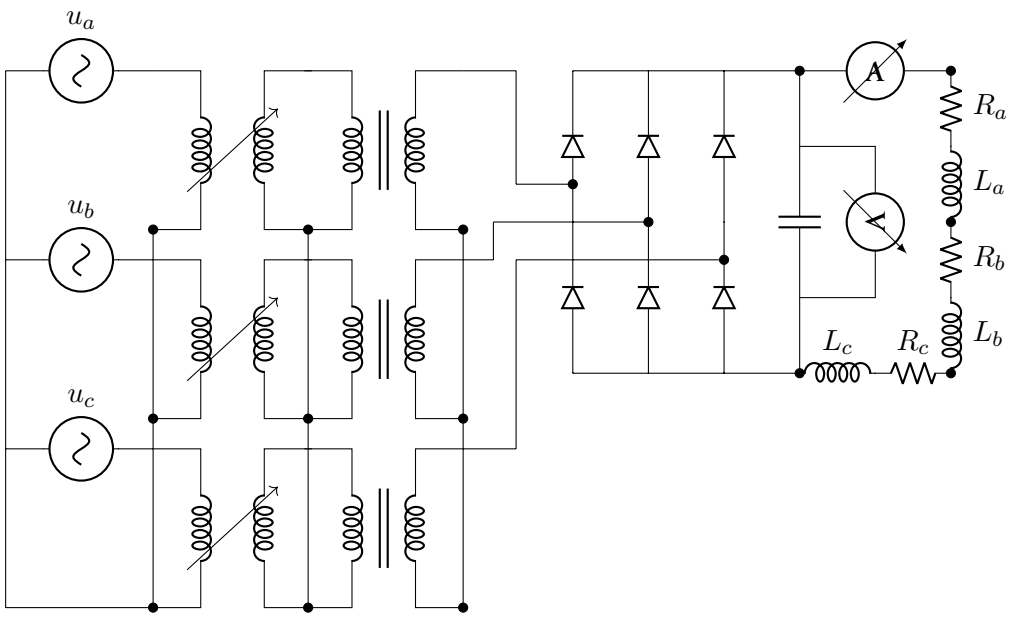

Figure 4.6: Setup configuration for the experimental tests.

The resistance R_0 in the state-space models (the state-space model is presented in section 4.3.2) is equal to the sum of the phase resistances in Figure 4.6, i.e. $R_0 = R_a + R_b + R_c$ at the same temperature as the water coolant (60^o in the following experimental results).

Control of the excitation current

The input current of the experiments should result in a thermal dynamic behaviour of the machine that simulates realistic thermal transients in the designated application. Since the torque varies from zero to values that almost cause overheating in the stator windings

in automotive applications, the current sequence includes both relatively high and low currents. In the setup, the current is controlled manually by adjusting the voltage from the variable transformer, and it can therefore not provide constant power pulses (the stator resistance increases when the temperature increases and the current therefore decreases, even though the voltage remains). However, this does not have a negative impact on the quality of the results as long as the current is measured accurately, and a wide range of current values are included throughout the test.

Another important aspect of the control of the input current is to not let the temperatures in the machine reach levels where they can cause damage. Especially the winding temperatures must be supervised since their insulation starts to degrade above the rated limits. Furthermore, the temperature sensor is never in the actual hot-spot of the winding, and there should therefore be a margin between the thermal limits and the maximum temperature of the experiments; the litterature suggests a limit of 10 ^{o}C below the rated maximum temperature of the windings [101].

Control of the water coolant temperature

The identification procedure and the thermal model of the machine suppose that the temperature of the water circuit (see Figure 4.2) of the cooling/heating setup remains constant throughout the tests. This is achieved by controlling the fan of a radiator that is included in the water circuit. The water temperature is measured at the inlet of the heat exchanger that is connected to the oil circuit, and a PI controller increases the speed of the fan if the temperature is too high, and vice versa if the temperature is too low. The heater makes it possible to keep the water temperature higher than room temperature until the test object reaches a quasi-steady-state temperature distribution, and the starting temperature of the experiments can therefore be chosen freely (within the thermal limits of the system).

4.4.1 Identification results

Figure 4.7a shows the input current of the system identification input sequence for the grey-box estimation. Since the voltage remains constant in the different operating points, the input current drops when the winding resistance increase due to the increasing temperature. The input voltage is changed six times to different values to provoke enough thermal dynamics so the system can be identified from the measured data. The sequence is approximately 50 minutes and includes currents that ranges from approximately 10 Amperes to 50 Amperes. It is difficult to draw a definitive conclusion regarding how long the sequence must be, and how many times and how much the current needs to change throughout the sequence to obtain enough information about the thermal transient behaviour of the machine for a satisfying system identification. However, the currents should result in the

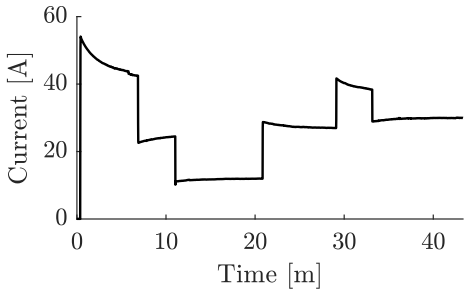

(a) Input current for identification dataset.

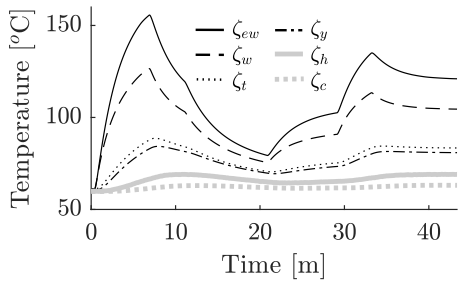

(b) Resulting node temperatures during excitation.

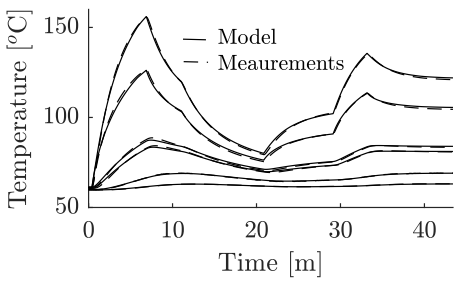

(c) Measurements together with the identified full-order grey-box model simulation results.

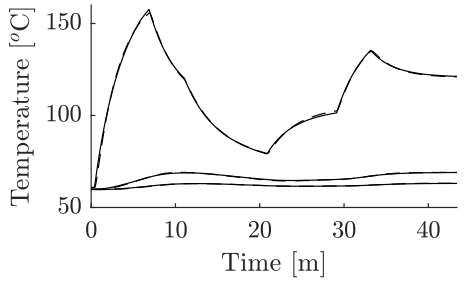

(d) Measurements together with the identified reduced-order grey-box model simulation results.

Figure 4.7: Identification input current and resulting temperature measurements and model simulations.

maximum temperature dynamics that can be expected during operation, and they should make the temperatures increase to almost the maximum allowed temperature in the machine.

The resulting measured node temperatures from the identification sequence experiment are shown in Figure 4.7b. The temperatures behave as expected: the hottest temperature arises in the end-winding, and the lowest in the oil coolant, which remains similar to the water temperature (60^oC) throughout the sequence. Figure 4.7c and 4.7d show the measurements together with the resulting full- and reduced-order model simulation results after the identification, respectively. Both model results fit the measurements very well, which is expected since the models are optimised based on the measurements.

Parameter values

Table 4.1 shows the resulting numerical parameter values of the analytical estimations, and of the initial and the resulting grey-box model estimations of the two models. The ca-

Table 4.1: Model parameters.

$\mathcal{R}_{ew\leftrightarrow w}$	0.116	C_{ew}	889
$\mathcal{R}_{w\leftrightarrow t}$	0.045	C_w	1150
$\mathcal{R}_{t\leftrightarrow y}$	0.022	C_t	2387
$\mathcal{R}_{y\leftrightarrow h}$	0.0407	C_y	2748
$\mathcal{R}_{h\leftrightarrow c}$	x	C_h	12000
$\mathcal{R}_{c\leftrightarrow c_w}$	x	C_c	x
q	0.36	α	0.004

(a) Analytically calculated model parameters.

$\mathcal{R}_{ew\leftrightarrow w}$	0.116	C_{ew}	889
$\mathcal{R}_{w\leftrightarrow t}$	0.0533	C_w	1150
$\mathcal{R}_{t\leftrightarrow y}$	0.0060	C_t	1200
$\mathcal{R}_{y\leftrightarrow h}$	0.0332	C_y	1200
$\mathcal{R}_{h\leftrightarrow c}$	0.017	C_h	12000
$\mathcal{R}_{c\leftrightarrow c_w}$	0.01	C_c	15000
q	0.36	α	0.004
$\mathcal{R}_{ew\leftrightarrow h}$	0.153	C_{ew+w}	2039
		C_{h+y+t}	17135

(b) Initial grey-box model parameters.

$\mathcal{R}_{ew\leftrightarrow w}$	0.116	C_{ew}	741
$\mathcal{R}_{w\leftrightarrow t}$	0.054	C_w	1383
$\mathcal{R}_{t\leftrightarrow y}$	0.0056	C_t	1728
$\mathcal{R}_{y\leftrightarrow h}$	0.028	C_y	1744
$\mathcal{R}_{h\leftrightarrow c}$	0.015	C_h	11207
$\mathcal{R}_{c\leftrightarrow c_w}$	0.009	C_c	15643
q	0.347	α	0.004

(c) Grey-box estimated model parameters for the full-order system.

$\mathcal{R}_{ew\leftrightarrow h}$	0.120	C_{ew+w}	1943
$\mathcal{R}_{h\leftrightarrow c}$	0.015	C_{h+s}	22541
$\mathcal{R}_{c\leftrightarrow c_w}$	0.008	C_c	9581
		α	0.004

(d) Grey-box estimated model parameters for the reduced-order system.

pacitance values of the analytical estimations (Table 4.1a) are used as initial parameters in the grey-box identification of the full-order system (Table 4.1b), except for the teeth and yoke, which are changed manually after a few test runs (see section 4.3.4 for an explanation to this). The initial capacitance values for the reduced-order model are derived from the analytically calculated values, where C_{ew+w} is the sum of the analytically derived winding and end-winding capacitances, and C_{h+s} is the sum of the analytically derived teeth, yoke and housing capacitances. The resistances of the initial grey-box identification parameters for both models are derived from the quasi-steady-state situation in the end of the identification sequence, and therefore differs from the analytically derived parameters.

Comparing the analytically calculated and the initial parameters, the biggest relative difference is found between the teeth and yoke results. A plausible explanation for this is that these parameters are very dependent on the placement of the sensors: The thermal resistance changes approximately linearly with the change of distance since the thermal resistivity between the sensors does not change significantly. Furthermore, the sensors are mounted on the outermost laminate of the machine, where the temperature gradient might not be as significant as in the middle of the machine. This would result in a smaller estimated thermal teeth-to-yoke resistance from the measurements compared to the calculated result. In addition, it is complicated to obtain information about how quick the temperature of the outmost laminate changes compared to the rest of the teeth and the yoke, and equivalent teeth and yoke thermal capacitance values are therefore complex to estimate. In either case, the resulting changes in the resistance and capacitance values between the analytically derived and the initial grey-box parameters are considered small enough to be realistic.

All the final grey-box parameter values of the full-order model are close to the initial values, except for the estimated teeth and yoke capacitances which lie in between the initial and the analytically estimated parameters, and the end-winding capacitance, which increase substantially, but not unrealistically much (Table 4.1c). The results point towards a model that relates closely to physics, which makes it likely to be valid for any arbitrary winding current. The reduced-order model identification yields a winding to house resistance that is lower than the initial, but still within reasonable limits (Table 4.1d). The estimated capacitances are also relatively close to the initial guesses. The identification results show that a representation of the machine as a third-order system yields a model that is surprisingly close to the physical expectations. However, it should be emphasised that this assumes that the sensors represent the actual temperatures of the machine, which is especially uncertain for the end-winding node. The conclusion of this chapter discusses this more.

4.4.2 Validation tests

After the identification procedure is finished, it is important to validate the resulting models to make sure they work well with arbitrary input data. Two validation procedures are considered.

1. In the first validation procedure, the setup remains the same as for the identification tests, but the input current sequence changes. A comparison between the temperature measurements when the new input current excites the machine and the simulation of the temperatures with the estimated models from the identification data, but with the new current input, gives information regarding the validity of the models.

2. In the second validation procedure, the phases of the test object is connected in a wye configuration, and a three-phase h-bridge converter acts as the power source during the experiment. A conventional PI current controller, which is used in e.g. back-to-back tests, controls the machine throughout the test. The new configuration makes it possible to validate the models when the machine rotates with a low speed. To make sure that the speed of the test object remains constant even though the controller demands a certain current that gives rise to a certain torque (rather than a constant speed), an additional load machine is connected to the shaft of the test object. It should be emphasised that the whole test procedure – and a good validation – can be performed with the initial test setup, which does not include an additional machine and drive. However, in this context it is good to reinforce the validation of the model to make sure that it performs well. The current of the test object is controlled with an MTPA algorithm (see chapter 2, section 2.2 for an explanation of the MTPA concept) to mimic a real operation situation as much as possible. With the new setup, the term $R_0 i(n)^2$ in the **B** matrix of the state-space models is exchanged for $\frac{R_0}{3}(i_d(n)^2 + i_d(n)^2)$, which yields the DC resistance power losses in the windings (AC losses are neglected). An alternative to this would be to keep the speed constant by changing the angle of the dq-axes current vector when the magnitude of it increases; such a strategy makes the extra machine redundant since the torque can be held constant even though the current changes. However, due to the limited time this was not studied in this project.

Validation Results from the standstill identification test setup

Figure 4.8 shows the input current and the resulting measured and simulated temperatures of the validation test sequence from the standstill identification test setup.

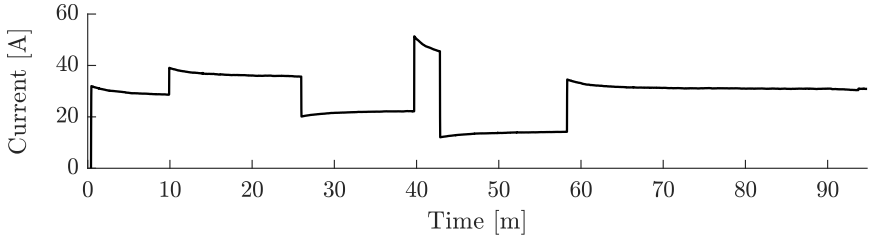

(a) Input validation current.

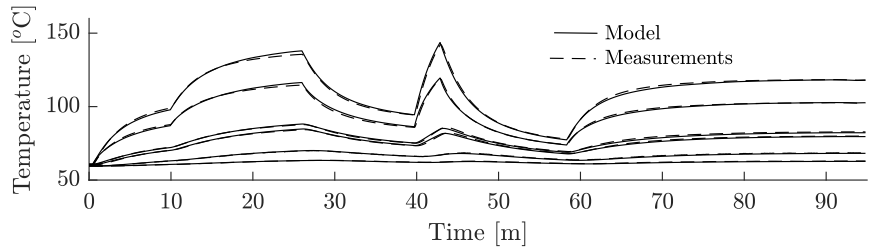

(b) Simulated and measured temperatures from the full-order model.

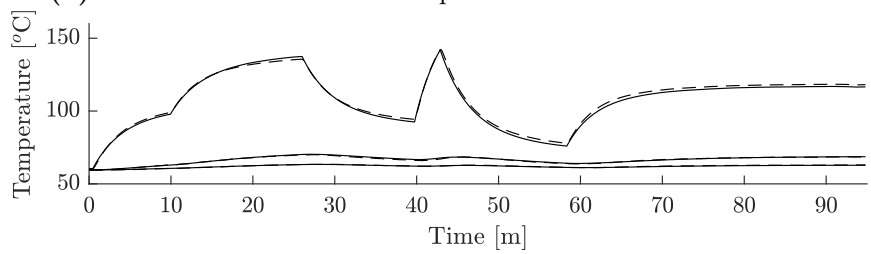

(c) Simulated and measured temperatures from the reduced-order model.

Figure 4.8: Validation from the standstill identification test setup with a new input current sequence and a new temperature profile.

The fits between both the full-order model and the reduced-order model simulation results and the measurements are good considering the arbitrary nature of the input current. Figure 4.9 shows the absolute and relative differences between the simulation results and the measurements.

The differences look almost discontinuous when the input current changes a lot in a short time. This may be due to that a heat source, one or two thermal resistances and a capacitance may be a too simple model to simulate the detailed transient behaviour of the windings. In either way, the discontinuous jumps do not matter much when judging the models' overall ability to predict the temperatures of the machine.

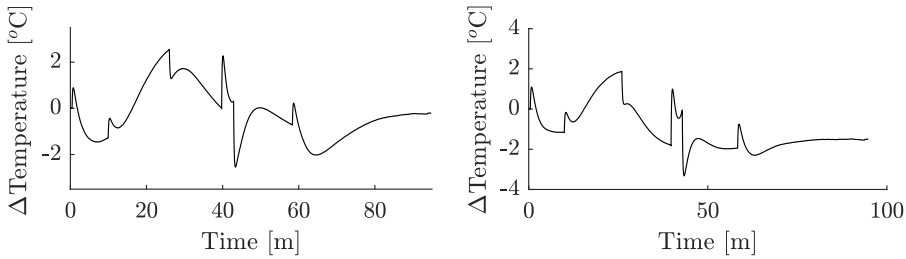

(a) Absolute difference between the measured and simulated temperatures for the full-order model.

(b) Absolute difference between the measured and simulated temperatures for the reduced-order model.

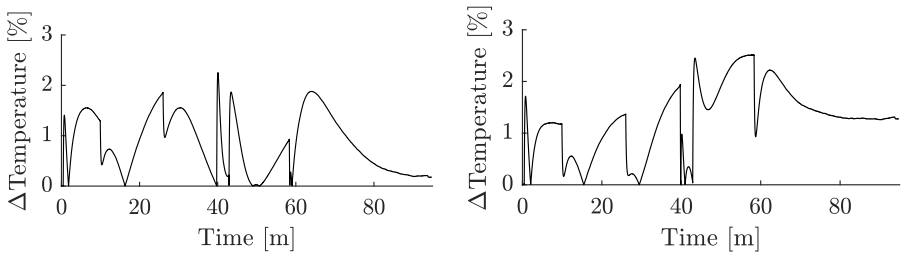

(c) Percental difference between the measured and simulated temperatures for the full-order model.

(d) Percental difference between the measured and simulated temperatures for the reduced-order model.

Figure 4.9: Difference between simulated and measured temperatures for the standstill identification test setup.

To analyse the results deeper, Table 4.2a shows the most significant absolute and the percental differences between the simulated and the measured temperatures.

Table 4.2: Deviation between measurements and simulations

	Full-order	Reduces-order
$\Delta\zeta_{max}$	2.56 ^{o}C	3.32 ^{o}C
$\Delta\zeta_{avr}$	0.91 ^{o}C	1.35 ^{o}C
$\Delta\zeta^p_{max}$	2.25 %	2.51 %
$\Delta\zeta^p_{avr}$	0.84 %	1.28 %

(a) Standstill test setup.

	Full-order	Reduced-order
$\Delta\zeta_{max}$	1.99^{o}C	2.72 ^{o}C
$\Delta\zeta_{avr}$	0.79 ^{o}C	1.30 ^{o}C
$\Delta\zeta^p_{max}$	2.53 %	3.31 %
$\Delta\zeta^p_{avr}$	0.95 %	1.52 %

(b) Rotating test setup.

The full-order model performs slightly better than the reduced-order model both in absolute and percental terms. The highest deviation in total of all temperatures is 3.32 ^{o}C, and the average absolute difference for the temperature that differs the most, which is the end-winding temperature, is 1.35 ^{o}C. Furthermore, the percental differences stay below 2.51 %.

Validation Results of constant speed tests

Figure 4.10 shows the results from the rotating test setup.

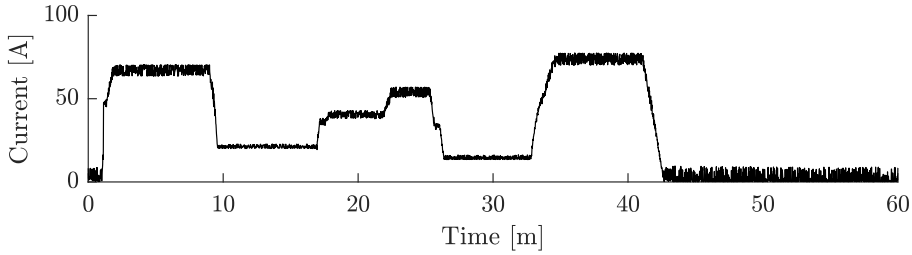

(a) Input current for identification data-set.

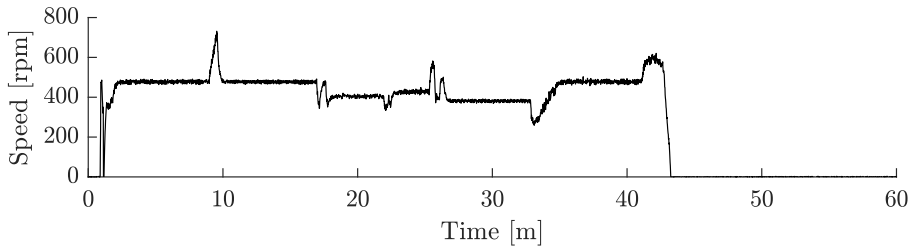

(b) Input speed for identification data-set.

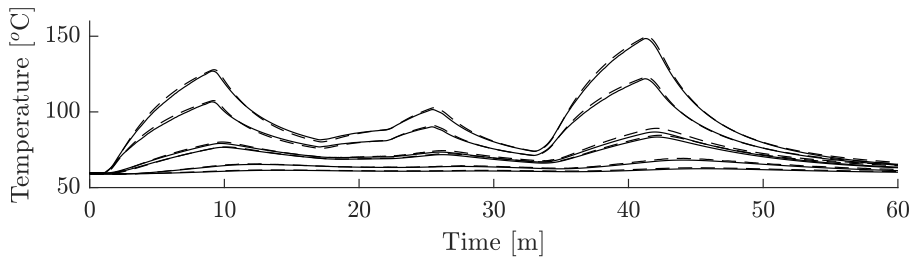

(c) Validation data-set measurements and simulated model results.

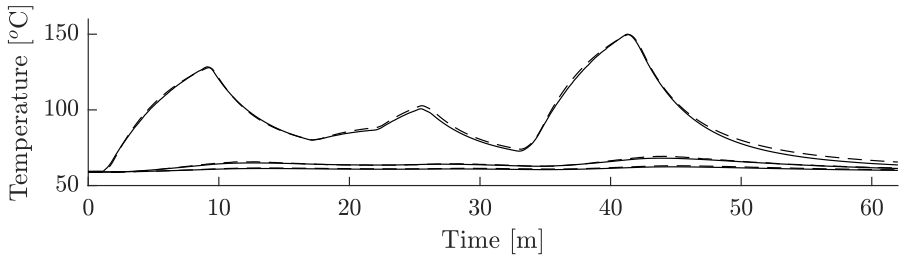

(d) Validation data-set measurements and simulated model results.

Figure 4.10: Identification data-set and resulting model simulations from the constant speed setup.

The rotating speed is kept around 500 rpm throughout the test. Considering the estimations of the previous chapter, the speed-dependent losses at 500 rpm are around 10 W. This is sufficiently low considering the relatively high stator resistance of the machine (see Figure 3.11 and Appendix A). To evaluate the results in more detail, Figure 4.11 shows the differences between the measurements and the simulations.

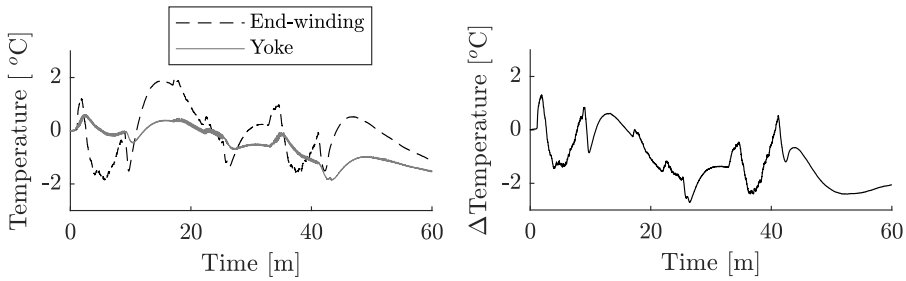

(a) Absolute difference between the measured and simulated temperatures for the full-order model.

(b) Absolute difference between the measured and simulated temperatures for the reduced-order model.

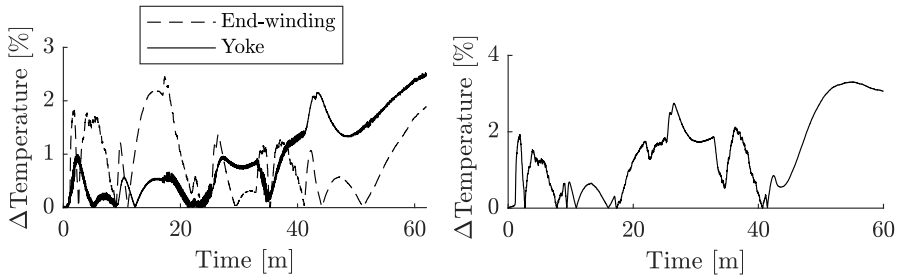

(c) Percental difference between the measured and simulated temperatures for the full-order model.

(d) Percental difference between the measured and simulated temperatures for the reduced-order model.

Figure 4.11: Difference between simulated and measured temperatures for the rotating test setup.

The measurements and the model results fit well considering the difference in the winding excitation and the rotation in the validation experiments compared to the identification test. As for the results from validation test with the initial setup, the end-winding temperature shows the greatest absolute difference between the measurements and the results from the full- and the reduced-order models. However, contrary to the first test, a comparison between the yoke temperature measurements and the simulations yields a similar difference, and the yoke temperature shows the biggest percental difference between the simulations and the measurements. The bigger difference between the yoke temperature measurements and the simulation is not surprising since the rotation leads to losses in the

core of the machine, and the model is therefore prone to underestimate the temperatures.

Table 4.2b shows the maximum and mean absolute and percental differences between the measurements and the model results. The percental difference between the end-winding temperature and the low-order model results is the biggest with 3.31 %. This difference occurs in the end of the sequence when the excitation is turned of and the machine temperature approaches the coolant temperature. Regardless, the measurements and model results shows good agreements considering the difference in excitation compared to the identification test setup.

4.5 Summary

This chapter describes a modelling and test procedure that derives experimentally based thermal models of IPMSMs when they stand still or operate at low speeds. The procedure includes a wide range of data in the identification procedure, and the models can therefore be used to simulate peak current capability of a machine. No sophisticated measurement equipment is necessary, and the procedure demands only one test sequence for the parameter identification. Therefore, the tests can be performed with relatively small means within a reasonable time scale. The chapter proposes two models: The first includes the temperatures of the end-winding, the winding, the stator, the housing and the coolant, while the second includes only the temperatures of the end-winding, the housing and the coolant. Below follows suggestions to possible applications and expansions of the models, and a discussion regarding an alternative test setup approach. Furthermore, since the sensors are a fundamental part of the modelling process, implications of sensor placements and inaccurate measurements are discussed.

The full-order model

The full-order model demands many sensors in the machine. These sensors are generally not included in serial production. However, prototypes are much more likely to include similar sensors for an extensive evaluation of a design. Therefore, the full-order model is primarily designed to get information about how the heat transfers, and how the thermal resistances in different parts of the machine behave. Theoretically, it is also straight forward to introduce speed-dependent losses in the model, considering that the majority of these losses are dissipated in the stator core. The identification and validation of such models require tests with both variable currents and frequencies, which in turn demands an additional machine to control the speed of the test object. However, a similar method as presented in the foregoing chapter, where the machine works constantly under mechanically transient conditions, could also work as input data, supposing the mechanical transient

are not too high. Furthermore, the loss models from the preceding chapter can be included in the model as a first estimation of the heat dissipation due to the speed-dependent losses. The model would lack an estimation of the permanent magnet (pm) temperatures since no rotor node is included[4]. However, it is quite straight forward (at least out of a theoretical point of view) to approximate the PM temperatures by estimating the linked magnetic flux online. Look-up tables that relate the linked magnetic flux to the temperature and currents, as presented in chapter 2, section 2.2.2, could be used for this purpose. In addition, it is possible to include an additional node in the rotor if it is needed. To conclude, the full-order model yields a good overview of how the temperature distributes over the machine, but leaves a lot of room for development and future work.

The reduced-order model

The reduced-order model only needs sensors in the end-winding (which is the hotspot in the considered machine), in the housing and in the coolant channels. However, the sensor of the housing is mounted on top of the machine, and as a consequence, the modelling procedure only demands that one sensor is integrated in the actual manufacturing process. As serial produced machines often feature a thermal sensor in the supposed hotspot, it is not unrealistic to assume that the reduced-order model can be derived for not only the prototype, but for all produced units. This makes it ideal for e.g. end-of-line testing, which can give an individual thermal model for each produced unit, and which can detect if something is wrong with the cooling system of the machine. However, the design of the model should still be done on a prototype, whereupon the model would be calibrated for each unit. An interesting continuation of the evaluation of the reduced-order model would be to see how well it predicts high thermal transients in the windings due to high currents when the rotational speed of the machine is high. If it is possible for the model to achieve this, it would add high value to predict e.g. thermal rise in the windings due to high regenerative braking [122]. Such predictions would be valuable for the development of current control algorithms. Unfortunately, this type of investigations were not feasible to perform within the time limit of the project.

Alternative identification test setup

Since the test methods of the former chapters use the same mechanical and electrical setup, an interesting continuation of this work would be to find a procedure to derive the thermal

[4]There is a sensor installed in the vicinity of the permanent magnets in the machine (this sensor is used in the experimental procedure of chapter 2 so it would be straight-forward to include such a node in the model. However, the node would give little useful information since 1) the thermal resistance between the stator and the rotor is significantly affected by the rotational speed, and 2) there are no losses in the rotor with DC currents in the windings.

identification data without changing these connections. One possible approach to achieve this could be to control the d-axis current with a current controller and the q-axis current with a speed controller. This would give the possibility to rotate the machine with a high enough speed to distribute the winding copper losses approximately equal over the slots, but a low enough speed to not induce significant speed-dependent losses. In addition, the magnitude of the losses could be controlled by adjusting the d-axis current. In this case, R_{o} in (4.10) would be equal to the stator resistance R_s, and $i(t)$ would be equal to $\sqrt{i_d^{s2} + i_q^{s2}}$. Of course, loss phenomena due to the switching converter would make it hard to estimate the power losses (the heat sources in (4.3)) very accurately. On the other hand, in many cases these losses are low enough to neglect.

Dependence on sensors

Since the identification of the proposed models builds upon temperature measurements from each respective node, the thermal sensors of the machine dictate the model designs. It is of course possible to add nodes that do not represent the experimentally obtained temperatures. However, the risk of divergence and bad optimisation results increase significantly if the order of the model increases without including more information about the dynamic temperature characteristics of the machine in the additional model nodes. This is prone to move the model towards a darker grey model, which in turn can result in problems with repeatability and validation if there is not a very substantial amount of identification data available.

The modelling procedure always assumes that the sensors measure the temperatures in the designated spatial positions in the machine. However, the sensor placement in the windings is difficult to control, and the model can therefore be optimised for unexpected spatial positions. This is especially important to emphasise when a node is put in the supposed hotspot of the machine (in this case the end-winding nodes of the models), since the measured temperature can be significantly lower than the actual. In addition, the uncertainty of the temperature measurements can be high, which also should be taken into account when deciding how reliable the model is.

Conclusions

The main purpose of this chapter is to present a procedure to derive a thermal model of a machine that operates under highly dynamical conditions. The proposed models are only valid for the considered or similar machine designs, and it is important to evaluate each design for itself, and to chose an equivalent circuit that represents the thermal behaviour of the machine in a sufficient way. This might also be an iterative process since the first choice

of an equivalent circuit might not yield sufficient results. Nevertheless, the results of this chapter show that the presented modelling approach can give good models with relatively small means.

Chapter 5

Applications, continuation and conclusion

This work presents methods that derive the electromagnetic properties, the loss profile, and information about the thermal behaviour of IPMSMs. The three aforementioned categories are divided into three different chapters that propose methods to find the characteristics of their respective part. Each chapter summarises the outcome of their presented methods respectively, and this final one therefore primarily aims to tie all the results together to find a general conclusion of the work. Below follow some alternative applications where the methods can be used together, suggestions on continuation of the work, and a final conclusion of the thesis.

Applications

The individual chapters propose applications for their respective methods. However, one application that has not yet been discussed in full is testing in the end of a production line. End-of-line testing can benefit from all the presented methods, and the methods can also be combined for a better result. The electromagnetic characterisation evaluates the magnetic model fast and gives individual data for each machine that can be used for optimal current controller design. Furthermore, if the shaft dimension of the test object is known, the moment of inertia on the rotating axis can be increased by introducing a flywheel that assures sufficiently low magnitudes of acceleration. In addition, the number of evaluated data points can be chosen so that 1) they give enough information to yield a sufficient magnetic model and 2) the test time stays within the given time requirements. A whole loss profile analysis, which demands a low magnitude of acceleration and consequently a high moment of inertia of the rotating axis, is unrealistic to perform on each manufactured machine in

the end-of-line context due to time requirements[1]. However, the low torque operational points of the magnetic model estimation dynamic test sequence still yield possibilities to control if the losses of the machine behave as expected, and consequently give insight into the health of the machine. Furthermore, a standstill thermal test as presented in chapter 4, but with a shorter excitation sequence, reveals if the thermal impedances deviate from the expected. All steps assume that a prototype has been evaluated in before hand so the results can be compared to the "correct" properties.

Another suitable application for the test methods of this work is in-situ testing of machines already installed in vehicles. This application requires that the shaft of the test object can be decoupled from the wheels with a clutch. If the disconnection is possible, all of the methods can be used to obtain a complete characterisation of the machine without needing to remove it from the vehicle. However, the test to obtain the data for the thermal model identification would have to be modified to excite the machine while it rotates slowly. Nevertheless, as described in section 4.5, this could be achieved with a controller strategy that controls the d-axis current with a current controller and the q-axis current with a speed controller. An evaluation of in-situ tests would be an interesting step for further research of the methods.

In addition to the end-of-line testing and vehicle in-situ testing, the methods can be used to give a coherent picture of a prototype machine to evaluate if it performs sufficiently for the intended application. Furthermore, the results from these tests can be used as a reference for the end-of-line evaluations. However, as mentioned numerous times in this thesis, the methods are not intended for machine benchmark testing that can be used as selling points, since these generally require detailed uncertainty analyses. Nevertheless, even though the uncertainty of the dynamic test results cannot be obtained in a straight forward manner, it does not mean that the results are bad, only that the possible statistical deviation from the results cannot be estimated numerically in an easy manner.

Continuation

Most of the continuation suggestions for the different parts of this thesis are discussed in each respective chapter. However, the work can also be put in a broader context that does not only focus on the specific methods but on machine and system identification in general. A first step in this line would be to include the power converter in the character-

[1]The results in chapter 3 show that an acceleration of around 180 rad/s^2 is on the limit to produce good results. With this acceleration the speed reaches 5000 rpm in around 3 seconds. Considering the design of the test sequence (see section 2.3.1), a test of this loading point would take around 12 seconds. Furthermore, in high field-weakening operation, the torque would be significantly lower, and the top speed significantly higher. Consequently, the testing time would be considerably longer, and the duration of a complete mapping of the machine could add up to half an hour or more. This is most likely not acceptable if machines are produced at a high rate.

isation process. If the converter properties are included in the results, the outcome yields a performance model of the whole electrical machine drive system in a vehicle. The most intuitive approach to achieve this is to measure the voltage and the current on the DC side of the converter (the side which is connected to a battery in an electrical vehicle). A comparison between the DC link power and the mechanical power on the shaft of the machine gives the complete losses of the whole system. Information about these losses would give possibilities to design control algorithms that minimise the losses of the whole machine drive system during operation.

Conclusion

As mentioned above, this thesis presents methods to derive the most important characteristics of an IPMSM: the electromagnetic properties, the loss profile, and thermal behaviour. The dynamic test approach that is presented proves to be an efficient procedure to obtain the electromagnetic characteristics of a machine quickly and accurately. To estimate the power losses with measurements from dynamic measurements is challenging, but the presented method proves to be a good tool to obtain detailed information of the losses of a test object, which can lay as a foundation for modelling. Finally, the presented thermal model estimation approach still has a lot of room for expansion, but gives a straight forward alternative to estimate the thermal characteristics of a machine at standstill and low-speed operation. Together, these methods present solutions to obtain information about the most relevant properties of an IPMSM. The introduction defines the aim of this thesis as "to obtain the most important characteristics of an IPMSM with 1) as little and cheap equipment as possible and 2) as fast testing procedures as possible". Considering the outcome of the thesis, the author believes the objectives of the research are met.

Appendix A

Testing equipment

Test objects

The specifications of the two machines that were used as test objects throughout this work are found in table A.1. The first test object, which we call **machine 1**, is designed by PhD Francisco J. Marquez-Fernandez for an Electric rear-wheel-drive unit. More information regarding specifications and the electromagnetic design process is found in [123], and a presentation and evaluation of the thermal properties of the machine is found in [124]. Figure A.1 shows a photo of machine 1.

Figure A.1: machine 1

The second test object, which we call **machine 2**, is designed by PhD Rasmus Andersson for heavy hybrid vehicles. A detailed presentation of the design and characteristics of the machine is found in [125]. Figure A.2 shows a photo of machine 2 with the flywheel that was used during the loss measurement experiments.

Table A.1: Characteristics of the test objects.

	machine 1	**machine 2**
Nbr of poles	8	6
Nbr of slots	24	36
Nbr of turns	8	4
Winding type	Double-layer distributed	Single-layer distributed
DC-link voltage	≈ 300 [V]	≈ 600 [V]
Base speed	≈3000 [rpm]	≈6000 [rpm]
Top speed	≈15000 [rpm]	≈15000 [rpm]
Rated torque	≈60 [Nm]	≈125 [Nm]
Peak torque	>100 [Nm]	≈250 [Nm]
Winding resistance	≈0.101 Ω	≈0.021 Ω

Appendix B presents finite element models of both test objects.

Power converter

The power converter that acted as power source throughout the experiments consists of six SKIIP 513 GD172-3DUL V3 modules which are rated for 1200 V DC-link voltage and 400 A rms current.

Control and data acquisition system

The compactRIO system from National Instruments acted as both control and data acquisition system during all of the experiments. The compactRIO is a modular system that allows a quick and flexible configuration of various input and output signals. Furthermore, the system features a field-programmable gate array (FPGA) that makes the synchronisation between the control loop, the demodulation of the resolver rotor position signals, the synchronisation of phase voltage measurements, and the saving of data relatively easy to perform.

Sensors

The list below presents the sensors that were used to perform the measurements throughout the work

- The hall effect current transducer LA 205-S was used to measure the phase currents.
- The hall effect transducer LEM LV25-p measured the DC voltage.

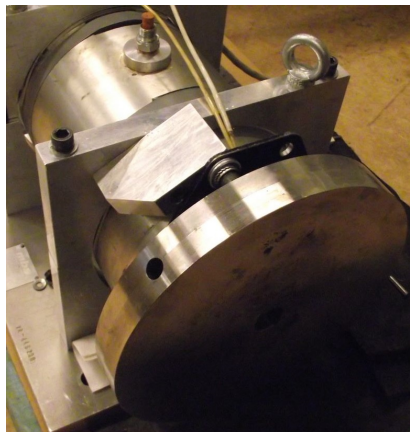

Figure A.2: machine 2

- The Tektronix P5200 high voltage differential probes were used to measure the switching instances of the power converter.
- A variable reluctance Singlsyn resolver by Tamagawa measured the rotor position of machine 1 and machine 2.
- pt100 thermal resistance thermometer sensors measured the temperature in the machines.

Appendix B

Finite element models

The finite element models of the machines that act as test objects in this thesis are shown in Figure B.1.

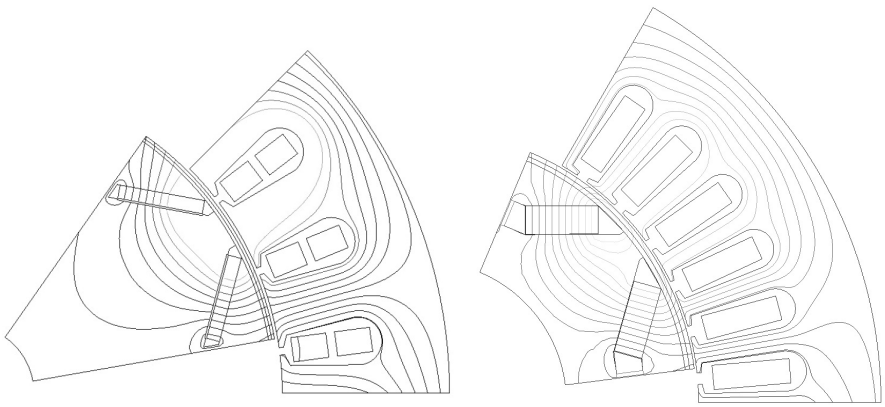

(a) Machine 1 **(b) Machine 2**

Figure B.1: FEM models of evaluated machines.

Due to deviation between the simulation results and the estimates based on experimental data, considerable effort has been put into analyses of the models. Downwards follow the most important conclusions drawn from the analyses.

Thermal aspects

The magnetic permeability of the components of the machine changes little with the temperature, and it is therefore neglected in the simulation model [126][1]. However, the permanent magnet BH characteristics change significantly and cannot be neglected. Figure B.2 shows an approximation of how the load line of the permanent magnets of the machine (N35SH neodynium magnets) change with temperature [23].

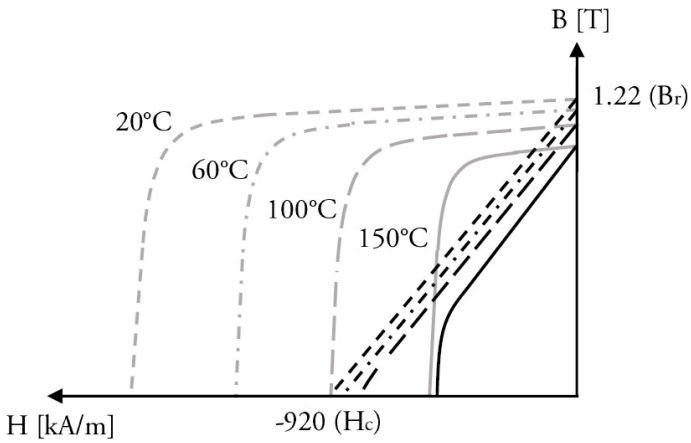

Figure B.2: Approximate temperature characteristics of N35SH.

The effect of the temperature on the permanent magnets is reversible up to a certain point where the remanence flux density is lowered permanently. In the ansys Maxwell software, which was used as the main simulation tool throughout this thesis, the permanent magnet BH characteristics are defined by the magnetic coeversity (H_c). However, the data sheet gives the temperature coefficient for the remanence flux (B_r). Since the remanence flux and the magnetic coevercity are approximately linearly dependent at relatively low temperatures the temperature coefficient holds for the remancence flux also, and the coevercity as a function of temperature can be calculated as

$$H_c(T) = H_c(20^o)\,(1 + \beta(T - 20^o)) \tag{B.1}$$

Where β is the temperature of coefficient for the remanence flux of the magnets, which in the case of N35SH neodynium magnets is -0.0011 [23]. When the temperature increases,

[1]The permeability of iron changes around 0.1%/°C, which can cause a noticable change for big temperature differences. However, since the permeability of the electric steel is so high compared to the one of the airgap and the permanent magnets, a substantial percental change of the reluctance due to the electric steel yields a much lower percental impact on the total reluctance of the magnetic circuits of the machines.

the relationship between H_c and B_r is no longer linear. As a consequence, the magnetic coevercity cannot be calculated with the temperature coefficient of the remanence flux which makes it hard to foresee the temperature's effect on H_c. In the simulations in this study the the coeversity was estimated with (B.1) throughout the whole temperature range. As the results in chapter 2 shows, this approximation holds fairly well within the tested temperature range.

Sensitivity of magnetic model simulation

The following list presents some important aspects of the magnetic model derivation of permanent magnet machines through FEM simulations that was found during the simulation process.

- The meshing next to the airgap is very important. The linked magnetic flux from the permanent magnets decreases when the mesh gets finer. A too coarse mesh consequently leads to an overestimation of the linked magnetic flux, which also earlier publications from the author have struggled with.
- The saturation characteristics of the core material affects the results significantly. The datasheet for the evaluated machines' electrical steel only gives the saturation curve up to 1.7 tesla. However, the saturation characteristics over 1.7 tesla have a significant impact on the results since the flux barriers in the rotor depend on saturation to prevent flux leakage. Furthermore, the overloading characteristics when the q-axis current is very high also change when the saturation data is erroneous. If the saturation is underestimated at high flux densities, the model underestimates the flux from the permanent magnets due to leakage, and overestimates the q-axis linked magnetic flux for high q-axis currents due to a too high iron permeability.
- The manufacturing process of the machine affect the flux and loss characteristics of the machine [11, 12]. If the simulation model has a narrow air gap between the rotor and stator small tolerance errors influence the inductance of the machine significantly. Furthermore, the effect depends on the manufacturing techniques, and each particular machine has individual characteristics that are very hard to include in the model. Therefore, it is next to impossible to achieve a perfect match between simulations and measurements.

In addition to the aspects above, all simulation results in this work comes from 2D models. Therefore, the models exclude effects from flux fringing and end-winding inductance. These phenomena can however be compensated for by analytical expressions. Hendershot and Miller give an approximate formula that assumes the end-windings to be formed as

circles with air in the middle to derive the inductance for a set geometry [127]. Figure B.3 illustrates such a model of the windings.

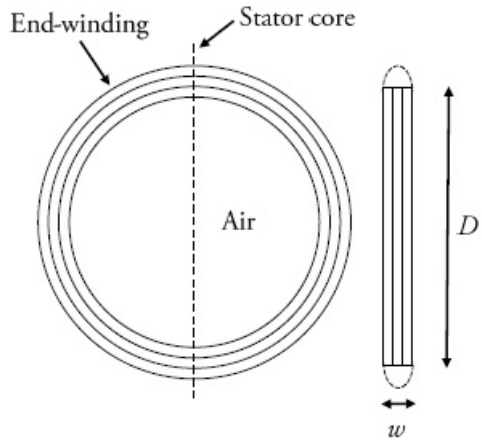

Figure B.3: end-winding model for inductance calculations.

Given the this simplification, the inductance is given by

$$L_{\text{circ}} = \frac{\mu_0 N_c^2 D}{2} \ln\left(\frac{4D}{0.447\sqrt{D \cdot w}} - 2\right) \tag{B.2}$$

where μ_0 is the magnetic permeability of free space, N_c is the number of turns in the windings, and D and w are the diameter and the width of the end-winding model, respectively (Figure B.3). There exists numerous other analytical equations to approximate the 3D effects, but for an accurate estimation 3D fem models is generally used [128,129]. 3D fem simulations are however time consuming both in terms of modelling and simulation time, and in most cases – at least for machines where the diameter of the machine is not significantly longer than the length – 2D simulations are sufficient.

It should be mentioned that since the machines that this thesis evaluates are relatively long compared to their diameter, the effect of the 3D phenomena are relative small. For example, (B.2) gives an end-winding inductance of approximately 1% of the active inductance in **machine 1**. This difference is so small that the aforementioned error sources clearly dominate in the inductance estimation.

Sensitivity of AC losses

The simulations greatly underestimate the AC losses in the machine. One of the most probable reason for the difference is the extra losses that the manufacturing of the machines gives rise to. Both the radial and the axial losses in the core increase significantly due to cutting of the laminates – this is especially true when laser cutting and welding are used in the manufacturing [92].

Appendix C

Current control and software implementation

The cRIO system from national instruments was the central control and data acquisition unit for the experiments in this work. The field programmable gate array (FPGA) that the system includes features accurate timing and true parallelism, which facilitates the implementation of a synchronised and well-performing current controller. The software is designed to synchronise the control and data acquisition as much as possible to avoid drifting and timing errors. This appendix explains the most important parts of the algorithms and how they are implemented

C.1 Main control loop

Figure C.1 shows a flowchart of the main control loop that was used throughout this project. The loop is synchronised with the inverter switching frequency, and the controller consequently gives a new voltage reference value every switching period. In the first step of the loop, Analog to digital converters sample measurements from the current sensors, the resolver signals and the DC link voltage into the system. Secondly, an algorithm demodulates the resolver signals to obtain the frequency and the rotor position of the test object. Thirdly, the measured voltages, currents and the position are stored in a FIFO to be sent to the host computer. Fourthly, the currents are transformed to dq-axes currents and are fed into the current controller (explained below). The dq-axes voltage references that the current controller produces are transformed to abc coordinates, whereupon converter non-linearities are compensated for in the reference voltages. The final reference voltages are sent to a fast loop that derives the gate signals for the IGBTs, and the loop restarts.

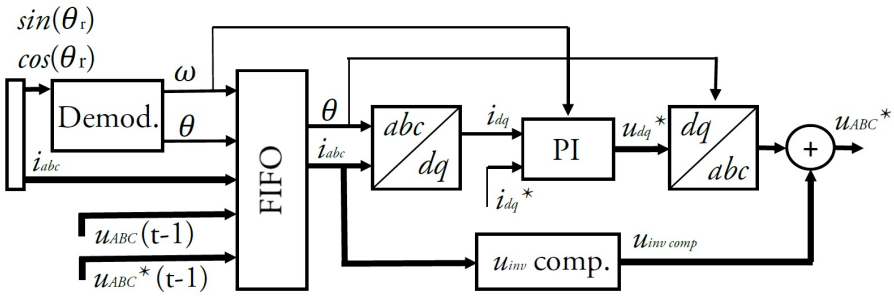

Figure C.1: Flowchart of the main control loop.

Resolver demodulation

The two machines that are tested in this work have resolvers as position sensors. The resolvers need to be excited with a high frequency signal – typically between 5 and 10 kHz – whereupon two signals in quadrature return to the control system for demodulation. In this work the cRIO generates a excitation signal of 10 kHz. Since the D/A converters of the system work with 100 kHz, the system can only generate 10 samples per excitation signal period. However, in the presented implementation a solution where only eight discrete values generates the excitation is chosen. This makes it possible to generate a symmetric excitation signal that is relatively easy to demodulate.

When the modulated signals return from the resolver the peak values are read into the system through fringe detection, and the trigonometric method yield the rotor angle [37]. The trigonometric method simply calculates the arctangent value of the peaks of the returning resolver signals as

$$\hat{\theta_r} = atan\left(\frac{\hat{u}\sin\theta}{\hat{u}\cos\theta}\right) \tag{C.1}$$

where zero division is avoided using the CORDIC algorithm [38]. Since the main control loop is synchronised with the excitation signal generation, the modulation can be done directly in the main loop with the sampled resolver signals.

Current controller

The design of the current controller is a standard proportional intergrator (PI) controller suggested by many publications. The PI gains are derived by the internal model design approach presented in [130]. The induced voltages in both d and q are feed forwarded for a better load disturbance rejection. In addition, compensations of inverter non-linearities

such as dead-times, rise and fall times and voltage drops of the semi-conductor components are feed forwarded.

Induced voltage feed forward

The most common PMSM PI control strategy feed forwards the emf (induced voltage due to the permanent magnet flux) and neglects the induced voltage due to the stator currents. A more refined model considers the induced voltages as functions of constant d and q inductance values and the rotational frequency together with the currents. However, if detailed flux characteristics as functions of the currents are available, look-up tables can be used to feed forward accurate estimations of the induced voltages. This further enhances the load disturbance rejection capabilities of the controller. In this work, the induced voltage is calculated with the current reference values for a more stable controller.

Inverter non-linearities feed forward

To further enhance the controller performance and to make the reference values from the controller as similar as possible to the actual inverter voltages, the algorithm feed forwards estimations of the non-linearities of the converter to the reference signals. This work finds the proper feed forward values with look-up tables as function of the phase currents. The look-up tables are derived by the by the following procedure

1. Measure the resistance of the phase windings of the machine;
2. Apply a d-axis current to align the flux from the permanent magnets with phase A;
3. Switch from current control to voltage control and apply a specific d-axis voltage. Note the resulting voltage phase references and measure the phase currents (the current should flow through two of the windings and not create a torque) and measure the resulting current in the stator windings. Calculate the voltage drop over the phases by multiplying the current with the resistance to find the actual phase voltages. The differences between the references and the voltages give the non-linearities for the specific phase currents. Do this for as many voltages/currents as necessary for the testing range.
4. Structure the results in look-up tables as functions of the phase currents.

The look-up tables are integrated in the controller algorithm as shown in Figure C.1. The non-linearities change when the DC-link voltage changes, and it is therefore necessary to have look-up tables for all the DC-voltages that are used.

Gate signal generation

The gate signals are generated according to the symmetrical suboscillation method. Firstly, the reference values from the current controller (u^*_{abc} in Figure C.1) are normalised by dividing them with $\frac{U_{DC}}{2}$

$$s_{abc} = u^*_{abc}\frac{2}{U_{dc}} \tag{C.2}$$

These signals are references for the suboscillation method and allows a maximum voltage of $\frac{U_{dc}}{2}$. To extend the accessible voltage it is possible to add zero sequence harmonics to the reference signals. The maximum possible voltage extension without over modulation is achieved by adding harmonics so that

$$\max(s'_{abc}) = -\min(s'_{abc}) \tag{C.3}$$

where s'_{abc} are the reference signals after the zero sequence component has been added. The condition is reached by

$$s'_{abc} = s_{abc} - \frac{\max(s'_{abc}) + \max(s'_{abc})}{2} \tag{C.4}$$

which becomes the final signals to be compared to the carrier wave to decide the duty-cycles for the converter legs.

Bibliography

[1] A. M. El-Refaie and T. M. Jahns. Comparison of synchronous PM machine types for wide constant-power speed range operation. In *Fourtieth IAS Annual Meeting. Conference Record of the 2005 Industry Applications Conference, 2005.*, volume 2, pages 1015–1022 Vol. 2, Oct 2005.

[2] Z. Yang, F. Shang, I. P. Brown, and M. Krishnamurthy. Comparative Study of Interior Permanent Magnet, Induction, and Switched Reluctance Motor Drives for EV and HEV Applications. *IEEE Transactions on Transportation Electrification*, 1(3):245–254, Oct 2015.

[3] T. Finken, M. Felden, and K. Hameyer. Comparison and design of different electrical machine types regarding their applicability in hybrid electrical vehicles. In *2008 18th International Conference on Electrical Machines*, pages 1–5, Sept 2008.

[4] A. Vagati, G. Pellegrino, and P. Guglielmi. Comparison between SPM and IPM motor drives for EV application. In *The XIX International Conference on Electrical Machines - ICEM 2010*, pages 1–6, Sept 2010.

[5] X. Liu, H. Chen, J. Zhao, and A. Belahcen. Research on the Performances and Parameters of Interior PMSM Used for Electric Vehicles. *IEEE Transactions on Industrial Electronics*, 63(6):3533–3545, June 2016.

[6] Joint Committee Guides Metrology. *Evaluation of measurement data – Guide to the Expression of Uncertainty in Measurement (GUM 2008)*, volume 100. 01 2008.

[7] L. Aarniovuori, J. Kolehmainen, A. Kosonen, M. Niemelä, H. Chen, W. Cao, and J. Pyrhönen. Application of Calorimetric Method for Loss Measurement of a SynRM Drive System. *IEEE Transactions on Industrial Electronics*, 63(4):2005–2015, April 2016.

[8] S. A. Odhano, R. Bojoi, M. Popescu, and A. Tenconi. Parameter identification and self-commissioning of AC permanent magnet machines - A review. In *2015 IEEE*

Workshop on Electrical Machines Design, Control and Diagnosis (WEMDCD), pages 195–203, March 2015.

[9] G. Domingues-Olavarria, F. J. Marquez-Fernandez, P. Fyhr, A. Reinap, M. Andersson, and M. Alakula. Optimization of Electric Powertrains Based on Scalable Cost and Performance Models. *IEEE Transactions on Industry Applications*, pages 1–1, 2018.

[10] G. Bramerdorfer, J. A. Tapia, J. J. Pyrhönen, and A. Cavagnino. Modern Electrical Machine Design Optimization: Techniques, Trends, and Best Practices. *IEEE Transactions on Industrial Electronics*, 65(10):7672–7684, Oct 2018.

[11] W. M. Arshad, T. Ryckebush, F. Magnussen, H. Lendenmann, J. Soulard, B. Eriksson, and B. Malmros. Incorporating Lamination Processing and Component Manufacturing in Electrical Machine Design Tools. In *2007 IEEE Industry Applications Annual Meeting*, pages 94–102, Sept 2007.

[12] A Belhadj, P Baudouin, F Breaban, A Deffontaine, M Dewulf, and Y Houbaert. Effect of laser cutting on microstructure and on magnetic properties of grain non-oriented electrical steels. *Journal of Magnetism and Magnetic Materials*, 256(1–3):20 – 31, 2003.

[13] V. B. Honsinger. Performance of Polyphase Permanent Magnet Machines. *IEEE Transactions on Power Apparatus and Systems*, PAS-99(4):1510–1518, July 1980.

[14] T. Sebastian, G. Slemon, and M. Rahman. Modelling of permanent magnet synchronous motors. *IEEE Transactions on Magnetics*, 22(5):1069–1071, Sep 1986.

[15] A. Gebregergis, M. H. Chowdhury, M. S. Islam, and T. Sebastian. Modeling of Permanent-Magnet Synchronous Machine Including Torque Ripple Effects. *IEEE Transactions on Industry Applications*, 51(1):232–239, Jan 2015.

[16] T. Herold, D. Franck, E. Lange, and K. Hameyer. Extension of a d-q model of a permanent magnet excited synchronous machine by including saturation, cross-coupling and slotting effects. In *2011 IEEE International Electric Machines Drives Conference (IEMDC)*, pages 1363–1367, May 2011.

[17] T. M. Jahns, G. B. Kliman, and T. W. Neumann. Interior Permanent-Magnet Synchronous Motors for Adjustable-Speed Drives. *IEEE Transactions on Industry Applications*, IA-22(4):738–747, July 1986.

[18] Y. A. . I. Mohamed and T. K. Lee. Adaptive self-tuning MTPA vector controller for IPMSM drive system. *IEEE Transactions on Energy Conversion*, 21(3):636–644, Sept 2006.

[19] P. Niazi, H. A. Toliyat, and A. Goodarzi. Robust Maximum Torque per Ampere (MTPA) Control of PM-Assisted SynRM for Traction Applications. *IEEE Transactions on Vehicular Technology*, 56(4):1538–1545, July 2007.

[20] S. Bolognani, R. Petrella, A. Prearo, and L. Sgarbossa. Automatic Tracking of MTPA Trajectory in IPM Motor Drives Based on AC Current Injection. *IEEE Transactions on Industry Applications*, 47(1):105–114, Jan 2011.

[21] J. Ottosson and M. Alakula. A compact field weakening controller implementation. In *International Symposium on Power Electronics, Electrical Drives, Automation and Motion, 2006. SPEEDAM 2006.*, pages 696–700, May 2006.

[22] A. Rabiei, T. Thiringer, and J. Lindberg. Maximizing the energy efficiency of a PMSM for vehicular applications using an iron loss accounting optimization based on nonlinear programming. In *2012 XXth International Conference on Electrical Machines*, pages 1001–1007, Sep. 2012.

[23] ECLIPSE magnetics. Sintered Neodymium Iron Boron (NdFeB) Magnets.

[24] T. Boileau, N. Leboeuf, B. Nahid-Mobarakeh, and F. Meibody-Tabar. Online Identification of PMSM Parameters: Parameter Identifiability and Estimator Comparative Study. *IEEE Transactions on Industry Applications*, 47(4):1944–1957, July 2011.

[25] K. Liu, Z. Q. Zhu, and D. A. Stone. Parameter Estimation for Condition Monitoring of PMSM Stator Winding and Rotor Permanent Magnets. *IEEE Transactions on Industrial Electronics*, 60(12):5902–5913, Dec 2013.

[26] S. Ichikawa, M. Tomita, S. Doki, and S. Okuma. Sensorless control of permanent-magnet synchronous motors using online parameter identification based on system identification theory. *IEEE Transactions on Industrial Electronics*, 53(2):363–372, April 2006.

[27] K. M. Rahman and S. Hiti. Identification of machine parameters of a synchronous motor. *IEEE Transactions on Industry Applications*, 41(2):557–565, March 2005.

[28] R. Dutta and M. F. Rahman. A Comparative Analysis of Two Test Methods of Measuring d - and q -Axes Inductances of Interior Permanent-Magnet Machine. *IEEE Transactions on Magnetics*, 42(11):3712–3718, Nov 2006.

[29] A. S. Babel, J. G. Cintron-Rivera, S. N. Foster, and E. G. Strangas. Evaluation of a Parameter Identification Method for Permanent Magnet AC Machines Through Parametric Sensitivity Analysis. *IEEE Transactions on Energy Conversion*, 29(1):240–249, March 2014.

[30] C. Choi, W. Lee, S. O. Kwon, and J. P. Hong. Experimental Estimation of Inductance for Interior Permanent Magnet Synchronous Machine Considering Temperature Distribution. *IEEE Transactions on Magnetics*, 49(6):2990–2996, June 2013.

[31] E. Armando, R. I. Bojoi, P. Guglielmi, G. Pellegrino, and M. Pastorelli. Experimental Identification of the Magnetic Model of Synchronous Machines. *IEEE Transactions on Industry Applications*, 49(5):2116–2125, Sept 2013.

[32] S. A. Odhano, R. Bojoi, Ş. G. Roşu, and A. Tenconi. Identification of the Magnetic Model of Permanent-Magnet Synchronous Machines Using DC-Biased Low-Frequency AC Signal Injection. *IEEE Transactions on Industry Applications*, 51(4):3208–3215, July 2015.

[33] G. Wang, L. Qu, H. Zhan, J. Xu, L. Ding, G. Zhang, and D. Xu. Self-Commissioning of Permanent Magnet Synchronous Machine Drives at Standstill Considering Inverter Nonlinearities. *IEEE Transactions on Power Electronics*, 29(12):6615–6627, Dec 2014.

[34] N. Bedetti, S. Calligaro, and R. Petrella. Stand-Still Self-Identification of Flux Characteristics for Synchronous Reluctance Machines Using Novel Saturation Approximating Function and Multiple Linear Regression. *IEEE Transactions on Industry Applications*, 52(4):3083–3092, July 2016.

[35] S. Wiedemann and R. M. Kennel. Encoderless self-commissioning and identification of synchronous reluctance machines at standstill. In *2017 IEEE 26th International Symposium on Industrial Electronics (ISIE)*, pages 296–302, June 2017.

[36] G. Pellegrino, B. Boazzo, and T. M. Jahns. Magnetic Model Self-Identification for PM Synchronous Machine Drives. *IEEE Transactions on Industry Applications*, 51(3):2246–2254, May 2015.

[37] K. Bouallaga, L. Idkhajine, A. Prata, and E. Monmasson. Demodulation methods on fully FPGA-based system for resolver signals treatment. In *2007 European Conference on Power Electronics and Applications*, pages 1–6, Sept 2007.

[38] J. E. Volder. The CORDIC Trigonometric Computing Technique. *IRE Transactions on Electronic Computers*, EC-8(3):330–334, Sept 1959.

[39] L. Idkhajine, E. Monmasson, M. W. Naouar, A. Prata, and K. Bouallaga. Fully Integrated FPGA-Based Controller for Synchronous Motor Drive. *IEEE Transactions on Industrial Electronics*, 56(10):4006–4017, Oct 2009.

[40] Y. Wang, Z. Zhu, and Z. Zuo. A Novel Design Method for Resolver-to-Digital Conversion. *IEEE Transactions on Industrial Electronics*, 62(6):3724–3731, June 2015.

[41] Tung-Hai Chin, M. Nakano, and T. Hirayama. Accurate measurement of instantaneous values of voltage, current and power for power electronics circuits. In *PESC 98 Record. 29th Annual IEEE Power Electronics Specialists Conference (Cat. No.98CH36196)*, volume 1, pages 302–307 vol.1, May 1998.

[42] T. D. Batzel and M. Comanescu. Instantaneous voltage measurement in PWM voltage source inverters. In *2007 International Aegean Conference on Electrical Machines and Power Electronics*, pages 168–173, Sept 2007.

[43] T. Qiu, X. Wen, and F. Zhao. Adaptive-Linear-Neuron-Based Dead-Time Effects Compensation Scheme for PMSM Drives. *IEEE Transactions on Power Electronics*, 31(3):2530–2538, March 2016.

[44] U. Abronzini, C. Attaianese, M. D'Arpino, M. Di Monaco, and G. Tomasso. Steady-State Dead-Time Compensation in VSI. *IEEE Transactions on Industrial Electronics*, 63(9):5858–5866, Sept 2016.

[45] K. Liu, Z. Q. Zhu, Q. Zhang, and J. Zhang. Influence of Nonideal Voltage Measurement on Parameter Estimation in Permanent-Magnet Synchronous Machines. *IEEE Transactions on Industrial Electronics*, 59(6):2438–2447, June 2012.

[46] I. R. Bojoi, E. Armando, G. Pellegrino, and S. G. Rosu. Self-commissioning of inverter nonlinear effects in ac drives. In *2012 IEEE International Energy Conference and Exhibition (ENERGYCON)*, pages 213–218, Sept 2012.

[47] Jonas Lundgren. splinefit. https://se.mathworks.com/matlabcentral/fileexchange/13812-splinefit.

[48] IEEE Guide for Test Procedures for Synchronous Machines Part IAcceptance and Performance Testing Part IITest Procedures and Parameter Determination for Dynamic Analysis. *IEEE Std 115-2009 (Revision of IEEE Std 115-1995)*, pages 1–219, May 2010.

[49] IEEE Trial-Use Guide for Testing Permanent Magnet Machines. *IEEE Std 1812-2014*, pages 1–56, Feb 2015.

[50] B. Deusinger, M. Lehr, and A. Binder. Determination of efficiency of permanent magnet synchronous machines from summation of losses. In *2014 International Symposium on Power Electronics, Electrical Drives, Automation and Motion*, pages 619–624, June 2014.

[51] D. Zeng, J. Zou, and Y. Xu. Analysis and Discussion of the Indirect Testing Method for the Losses of Permanent Magnet Synchronous Machines. *IEEE Transactions on Magnetics*, 54(11):1–5, Nov 2018.

[52] N. Yogal, C. Lehrmann, and M. Henke. Determination of the Measurement Uncertainty of Direct and Indirect Efficiency Measurement Methods in Permanent Magnet Synchronous Machines. In *2018 XIII International Conference on Electrical Machines (ICEM)*, pages 1149–1156, Sep. 2018.

[53] R. Wrobel, P. H. Mellor, M. Popescu, and D. A. Staton. Power Loss Analysis in Thermal Design of Permanent-Magnet Machines x2014;A Review. *IEEE Transactions on Industry Applications*, 52(2):1359–1368, March 2016.

[54] W. Cao, G. M. Asher, X. Huang, H. Zhang, I. French, J. Zhang, and M. Short. Calorimeters and Techniques Used for Power Loss Measurements in Electrical Machines. *IEEE Instrumentation Measurement Magazine*, 13(6):26–33, December 2010.

[55] B. Baholo, P.H. Mellor, D. Howe, and T.S. Birch. An automated calorimetric method of loss measurement in electrical machines. *Journal of Magnetism and Magnetic Materials*, 133(1):433 – 436, 1994.

[56] C. D. Graham Jr. Physical origin of losses in conducting ferromagnetic materials (invited). *Journal of Applied Physics*, 53(11):8276–8280, 1982.

[57] Andreas Krings and Juliette Soulard. Overview and Comparison of Iron Loss Models for Electrical Machines. 10:162–169, 05 2010.

[58] J. Reinert, A. Brockmeyer, and R. W. A. A. De Doncker. Calculation of losses in ferro- and ferrimagnetic materials based on the modified Steinmetz equation. *IEEE Transactions on Industry Applications*, 37(4):1055–1061, Jul 2001.

[59] C. P. Steinmetz. On the Law of Hysteresis. *Transactions of the American Institute of Electrical Engineers*, IX(1):1–64, Jan 1892.

[60] R H. Pry and C P. Bean. Calculation of the Energy Loss in Magnetic Sheet Materials Using a Domain Model. 29:532–533, 03 1958.

[61] G. Bertotti. Physical interpretation of eddy current losses in ferromagnetic materials. I. Theoretical considerations. *Journal of Applied Physics*, 57(6):2110–2117, 1985.

[62] K. Foster. Temperature dependence of loss separation measurements for oriented silicon steels. *IEEE Transactions on Magnetics*, 22(1):49–53, Jan 1986.

[63] A. Mouillet, J. L. Ille, M. Akroune, and M. A. Dami. Magnetic and loss characteristics of nonoriented silicon-iron under unconventional conditions. *IEE Proceedings - Science, Measurement and Technology*, 141(1):75–78, Jan 1994.

[64] N. Takahashi, M. Morishita, D. Miyagi, and M. Nakano. Comparison of Magnetic Properties of Magnetic Materials at High Temperature. *IEEE Transactions on Magnetics*, 47(10):4352–4355, Oct 2011.

[65] A. Krings, S. A. Mousavi, O. Wallmark, and J. Soulard. Temperature Influence of NiFe Steel Laminations on the Characteristics of Small Slotless Permanent Magnet Machines. *IEEE Transactions on Magnetics*, 49(7):4064–4067, July 2013.

[66] Ned Mohan, Tore Marvin Undeland, and William P. Robbins. *Power electronics : converters, applications and design.* New York : Wiley, cop. 1995, 1995.

[67] A. M. Urling, V. A. Niemela, G. R. Skutt, and T. G. Wilson. Characterizing high-frequency effects in transformer windings-a guide to several significant articles. In *Proceedings, Fourth Annual IEEE Applied Power Electronics Conference and Exposition*, pages 373–385, Mar 1989.

[68] J. A. Ferreira. AAnalytical computation of AC resistance of round and rectangular litz wire windings. *IEE Proceedings B - Electric Power Applications*, 139(1):21–25, Jan 1992.

[69] J. Mühlethaler, J. W. Kolar, and A. Ecklebe. Loss modeling of inductive components employed in power electronic systems. In *8th International Conference on Power Electronics - ECCE Asia*, pages 945–952, May 2011.

[70] Glenn S. Smith. A simple derivation for the skin effect in a round wire. 35, 03 2014.

[71] C. R. Sullivan. Computationally efficient winding loss calculation with multiple windings, arbitrary waveforms, and two-dimensional or three-dimensional field geometry. *IEEE Transactions on Power Electronics*, 16(1):142–150, Jan 2001.

[72] A. S. Thomas, Z. Q. Zhu, and G. W. Jewell. Proximity Loss Study In High Speed Flux-Switching Permanent Magnet Machine. *IEEE Transactions on Magnetics*, 45(10):4748–4751, Oct 2009.

[73] M. van der Geest, H. Polinder, J. A. Ferreira, and D. Zeilstra. Current Sharing Analysis of Parallel Strands in Low-Voltage High-Speed Machines. *IEEE Transactions on Industrial Electronics*, 61(6):3064–3070, June 2014.

[74] Pontus Fyhr. *Electromobility (Materials and Manufacturiing Economics)*. PhD thesis, Lund University, 2018.

[75] RA Matula. Electrical resistivity of copper, gold, palladium, and silver. 8, 10 1979.

[76] R. Wrobel, D. E. Salt, A. Griffo, N. Simpson, and P. H. Mellor. Derivation and Scaling of AC Copper Loss in Thermal Modeling of Electrical Machines. *IEEE Transactions on Industrial Electronics*, 61(8):4412–4420, Aug 2014.

[77] SKF. *Rolling bearings*. SKF group, 2016.

[78] SKF. SKF Bearing Calculator. `skf.com/bearingcalculator`, 2018. [Online; accessed 06-June-2018].

[79] Rasmus Andersson. *On the Design of Electric Traction Machines*. PhD thesis, Division of Industrial Electrical Engineering and Automation, Faculty of Engineering, Lund University, 2019.

[80] Peter R.N. Childs. Chapter 4 - introduction to rotating disc systems. In Peter R.N. Childs, editor, *Rotating Flow*, pages 81 – 126. Butterworth-Heinemann, Oxford, 2011.

[81] P. D. Pfister and Y. Perriard. Very-High-Speed Slotless Permanent-Magnet Motors: Analytical Modeling, Optimization, Design, and Torque Measurement Methods. *IEEE Transactions on Industrial Electronics*, 57(1):296–303, Jan 2010.

[82] K. Kiyota, T. Kakishima, and A. Chiba. Estimation and comparison of the windage loss of a 60 kW Switched Reluctance Motor for hybrid electric vehicles. In *2014 International Power Electronics Conference (IPEC-Hiroshima 2014 - ECCE ASIA)*, pages 3513–3518, May 2014.

[83] Kevin R. Anderson, Jun Lin, and Alexander Wong. Experimental and Numerical Study of Windage Losses in the Narrow Gap Region of a High-Speed Electric Motor. *Fluids*, 3(1), 2018.

[84] J. E. Vrancik. *Prediction of windage power loss in alternators*. NASA, United States, 1971.

[85] S. H. Han, T. M. Jahns, and Z. Q. Zhu. Analysis of Rotor Core Eddy-Current Losses in Interior Permanent-Magnet Synchronous Machines. *IEEE Transactions on Industry Applications*, 46(1):196–205, Jan 2010.

[86] Hui Zhang and Oskar Wallmark. Limitations and Constraints of Eddy-Current Loss Models for Interior Permanent-Magnet Motors with Fractional-Slot Concentrated Windings. *Energies*, 10(3), 2017.

[87] M. Krakowski. Eddy-current losses in thin circular and rectangular plates. *Archiv für Elektrotechnik*, 64(6):307–311, Nov 1982.

[88] M. Paradkar and J. Böcker. 3D analytical model for estimation of eddy currentlosses in the magnets of IPM machine considering the reaction field of the induced eddy currents. In *2015 IEEE Energy Conversion Congress and Exposition (ECCE)*, pages 2862–2869, Sept 2015.

[89] M. Cheng and S. Zhu. Calculation of PM Eddy Current Loss in IPM Machine Under PWM VSI Supply With Combined 2-D FE and Analytical Method. *IEEE Transactions on Magnetics*, 53(1):1–12, Jan 2017.

[90] K. Yamazaki and A. Abe. Loss Investigation of Interior Permanent-Magnet Motors Considering Carrier Harmonics and Magnet Eddy Currents. *IEEE Transactions on Industry Applications*, 45(2):659–665, March 2009.

[91] Rolf Johansson. *System modeling and identification*. Prentice Hall, 1993.

[92] M. Veigel, A. Krämer, G. Lanza, and M. Doppelbauer. Investigation of the impact of production processes on iron losses of laminated stator cores for electric machines. In *2016 IEEE Energy Conversion Congress and Exposition (ECCE)*, pages 1–5, Sept 2016.

[93] F. Boseniuk and B. Ponick. Parameterization of transient thermal models for permanent magnet synchronous machines exclusively based on measurements. In *2014 International Symposium on Power Electronics, Electrical Drives, Automation and Motion*, pages 295–301, June 2014.

[94] O. Wallscheid and J. Böcker. Global Identification of a Low-Order Lumped-Parameter Thermal Network for Permanent Magnet Synchronous Motors. *IEEE Transactions on Energy Conversion*, 31(1):354–365, March 2016.

[95] D. Gaona, O. Wallscheid, and J. Böcker. Glocal identification methods for low-order lumped parameter thermal networks used in permanent magnet synchronous motors. In *2017 IEEE 12th International Conference on Power Electronics and Drive Systems (PEDS)*, pages 1,126–1,134, Dec 2017.

[96] T. Huber, W. Peters, and J. Böcker. Monitoring critical temperatures in permanent magnet synchronous motors using low-order thermal models. In *2014 International Power Electronics Conference (IPEC-Hiroshima 2014 - ECCE ASIA)*, pages 1508–1515, May 2014.

[97] A. Boglietti, E. Carpaneto, M. Cossale, A. Lucco Borlera, D. Staton, and M. Popescu. Electrical machine first order short-time thermal transients model: Measurements and parameters evaluation. In *IECON 2014 - 40th Annual Conference of the IEEE Industrial Electronics Society*, pages 555–561, Oct 2014.

[98] J. Godbehere, R. Wrobel, D. Drury, and P. H. Mellor. Experimentally Calibrated Thermal Stator Modeling of AC Machines for Short-Duty Transient Operation. *IEEE Transactions on Industry Applications*, 53(4):3457–3466, July 2017.

[99] V. T. Buyukdegirmenci and P. T. Krein. Induction Machine Characterization for Short-Term or Momentary Stall Torque. *IEEE Transactions on Industry Applications*, 51(3):2237–2245, May 2015.

[100] A. Boglietti, E. Carpaneto, M. Cossale, and S. Vaschetto. Stator-Winding Thermal Models for Short-Time Thermal Transients: Definition and Validation. *IEEE Transactions on Industrial Electronics*, 63(5):2713–2721, May 2016.

[101] A. Boglietti, M. Cossale, S. Vaschetto, and T. Dutra. Winding Thermal Model for Short-Time Transient: Experimental Validation in Operative Conditions. *IEEE Transactions on Industry Applications*, 54(2):1312–1319, March 2018.

[102] A. Boglietti, A. Cavagnino, D. Staton, M. Shanel, M. Mueller, and C. Mejuto. Evolution and Modern Approaches for Thermal Analysis of Electrical Machines. *IEEE Transactions on Industrial Electronics*, 56(3):871–882, March 2009.

[103] Developers of Thermal Analysis Kit (Tak) KK Associates. *Thermal network modelling handbock*. 1999-2000. https://www.tak2000.com.

[104] Yunus A. Cengel and Afshin J. Ghajar. *Heat and Mass Transfer: Fundamentals and Applications*. McGraw-Hill Education., 2015.

[105] A. Boglietti, A. Cavagnino, and D. Staton. Determination of Critical Parameters in Electrical Machine Thermal Models. *IEEE Transactions on Industry Applications*, 44(4):1150–1159, July 2008.

[106] D. Staton, A. Boglietti, and A. Cavagnino. Solving the More Difficult Aspects of Electric Motor Thermal Analysis in Small and Medium Size Industrial Induction Motors. *IEEE Transactions on Energy Conversion*, 20(3):620–628, Sept 2005.

[107] N. Simpson, R. Wrobel, and P. H. Mellor. Estimation of Equivalent Thermal Parameters of Impregnated Electrical Windings. *IEEE Transactions on Industry Applications*, 49(6):2505–2515, Nov 2013.

[108] A. Boglietti, E. Carpaneto, M. Cossale, S. Vaschetto, M. Popescu, and D. A. Staton. Stator Winding Thermal Conductivity Evaluation: An Industrial Production Assessment. *IEEE Transactions on Industry Applications*, 52(5):3893–3900, Sept 2016.

[109] N. Simpson, T. Duggan, P. H. Mellor, and J. D. Booker. Measurement of the thermal characteristics of a stator-housing interface. In *2017 IEEE 11th International Symposium on Diagnostics for Electrical Machines, Power Electronics and Drives (SDEMPED)*, pages 557–564, Aug 2017.

[110] Peter Böckh and Thomas Wetzel. *Heat Transfer. [Elektronisk resurs] : Basics and Practice.* Berlin, Heidelberg : Springer Berlin Heidelberg, 2012., 2012.

[111] Karel J. Keesman. *System Identification*. Springer, London, 2011.

[112] C. Y. Ho R. W. Powell and P. E. Liley. *Thermal Conductivity of Selected Materials*. UNITED STATES DEPARTMENT OF COMMERCE, 1966.

[113] W. G. Saba G. T. Furukawa and M. L. Reilly. *Critical Analysis of the Heat-Capacity Data of the Literature and Evaluation of Thermodynamic Properties of Copper, Silver,*

and Gold from 0 to 300 °K. UNITED STATES DEPARTMENT OF COMMERCE, 1968.

[114] Lennart Ljung Torkel Glad. *Reglerteknik*. Studentlitteratur, 2008.

[115] F. J. Márquez-Fernández, J. H. J. Potgieter, A. G. Fraser, and M. D. McCulloch. Experimental validation of a thermal model for high speed switched reluctance machines for traction applications. In *2016 XXII International Conference on Electrical Machines (ICEM)*, pages 2711–2717, Sept 2016.

[116] Gunnar Kylander. *Thermal modelling of small cage induction motors*. PhD thesis, Chalmers University of Technology, 2 1995.

[117] D. Kowal, P. Sergeant, L. Dupré, and L. Vandenbossche. The Effect of the Electrical Steel Properties on the Temperature Distribution in Direct-Drive PM Synchronous Generators for 5 MW Wind Turbines. *IEEE Transactions on Magnetics*, 49(10):5371–5377, Oct 2013.

[118] Eric W. Lemmon. *CRC handbook of chemistry and physics*. CRC Press, 2018.

[119] Matlab's *Grey-Box Model Estimation* package description. `https://se.mathworks.com/help/ident/grey-box-model-estimation.html`.

[120] A. Wills and B. Ninness. On Gradient-Based Search for Multivariable System Estimates. *IEEE Transactions on Automatic Control*, 53(1):298–306, Feb 2008.

[121] J. Kennedy and R. Eberhart. Particle swarm optimization. In *Neural Networks, 1995. Proceedings., IEEE International Conference on*, volume 4, pages 1942–1948 vol.4, Nov 1995.

[122] G. Domingues. *Wisdom of Gabo D*. 2018.

[123] Francisco J. Marquez-Fernandez. *Electric Traction Machine Design for an E-RWD Unit*. PhD thesis, Division of Industrial Electrical Engineering and Automation, Faculty of Engineering, Lund University, 2014.

[124] Zhe Huang. Thermal design of Electrical Machines - Investigation and Evaluation of Cooling Performances, 2014.

[125] Rasmus Andersson. Electric Traction Machine Design for Heavy Hybrid Vehicles, 2014.

[126] R. L. Sanford. *Temperature Coefficient of Permeability within the Working Range*. Bulletin of the Bureau of Standards vol. 12, 1914.

[127] TJE Miller J. R. Hendershot. *Design on brushless permanent-magnet motors*. Magna psysics publishing, 1994.

[128] J. H. J. Potgieter and M. J. Kamper. Calculation Methods and Effects of End-Winding Inductance and Permanent-Magnet End Flux on Performance Prediction of Nonoverlap Winding Permanent-Magnet Machines. *IEEE Transactions on Industry Applications*, 50(4):2458–2466, July 2014.

[129] M. Bortolozzi, A. Tessarolo, and C. Bruzzese. Analytical Computation of End-Coil Leakage Inductance of Round-Rotor Synchronous Machines Field Winding. *IEEE Transactions on Magnetics*, 52(2):1–10, Feb 2016.

[130] L. Harnefors and H. P. Nee. Model-based current control of AC machines using the internal model control method. *IEEE Transactions on Industry Applications*, 34(1):133–141, Jan 1998.

I decided to become the PMSM king
and if I die fighting, then that's that

Printed by Media-Tryck, Lund 2019 NORDIC SWAN ECOLABEL 3041 0903

Lund University
Faculty of Engineering
Department of Biomedical Engineering
Division of Industrial Electrical Engineering
and Automation
ISBN 978-91-88934-98-7
ISSN LUTEDX/(TEIE-1092)/1-199/(2019)